Space Charge Behavior and Partial Discharge Mechanism in SF_6 Gas

Toshihiro Takahashi

Space Charge Behavior and Partial Discharge Mechanism in SF_6 Gas

Toshihiro Takahashi

Table of Contents

Chapter 1 Introduction

1.1 Role of Electric Power in Human Life

In human life, electric power has become the most essential energy source in residential, commercial and industrial fields. This is due to plenty of advantages of electric power, e.g., cleanliness, high safety, easy transmission and high efficiency in conversion into heat, light, etc. Thus, the availability of electric power has been expanding extensively. Electric power consumption in the world has increased from $10{,}524\times10^9$ kWh in 1990 to $12{,}260\times10^9$ kWh in 1997, whose 59.4% was consumed in industrialized countries such as United States and Japan[1]. In 2020, it is expected to rise up to $21{,}574\times10^9$ kWh, due to not only the rapid industrialization of developing countries such as China, India and South Korea, but also more widespread applications of electrical and electronic devices in the industrialized countries[1].

Moreover, the information technologies represented by the Internet and computers with high performance have been rapidly developing and widely spreading into all over the world, especially in the industrialized countries. In the near future, the Internet will be one of the most important social infrastructures, whose operation is supported by the electricity.

Therefore, the role of electric power will continue to be raised up, and its stable and quality supply is strongly needed.

1.2 Electric Power Apparatus and SF6 Gas

In order to transmit electric power with the least loss and the highest reliability for a long distance from electric power plants remote from cities, the voltage level of transmission lines should be raised. The highest rated voltage level is nowadays 500 kV in Japan, 765 kV in North America and 420 kV in Europe. In Japan, raising the rated voltage up to 1000 kV (UHV: Ultra High Voltage) has been planned and electric power apparatus for UHV transmission have been developed[2, 3]. On the contrary, the electric power apparatus and substations should be as compact as possible in order to reduce the cost of construction, the influence on the surroundings, etc. Then, the higher the rated voltage of electric power apparatus is, the higher the electric field strength is pursued inside the apparatus.

SF6 gas has a large electronegativity, which leads to high electrical insulation property[4, 5]. Figure 1.1 shows the electric field dependence of effective ionization coefficient of SF6 gas and air[6]. In Fig. 1.1, the critical electric field strength for SF6 gas, where the effective ionization coefficient becomes 0, is about 3 times higher than that for air. This means that the insulation strength under homogeneous electric field for SF6 gas is 3 times higher than that for air. This merit has been brought about by large collision and attachment cross sections of SF6 gas, as shown in Fig. 1.2[4]. Besides the electrical insulation property, SF6 gas has the following industrial features;

(1) Non-toxicity; SF6 gas itself is categorized as only asphyxiant gas and is reported that a human could survive comfortably and indefinitely in a mixture of 20% O2 and 80% SF6[7].

(2) Non-flammability and chemical inertness; They are attributed to the tight bonding between fluorines and sulphur[8, 9]. These features bring about 3200-year lifetime in atmosphere[10] .

(3) Arc quenching ability; Insulation property of SF6 gas rapidly recovers in the case of electrical breakdown, which brings about superior arc-quenching ability[11, 12].

Other physical and chemical properties of SF6 gas are shown in Table 1.1. As shown in Table 1.1, since the sublimation point is reasonably low, -63.8°C, SF6 gas can be used at the high

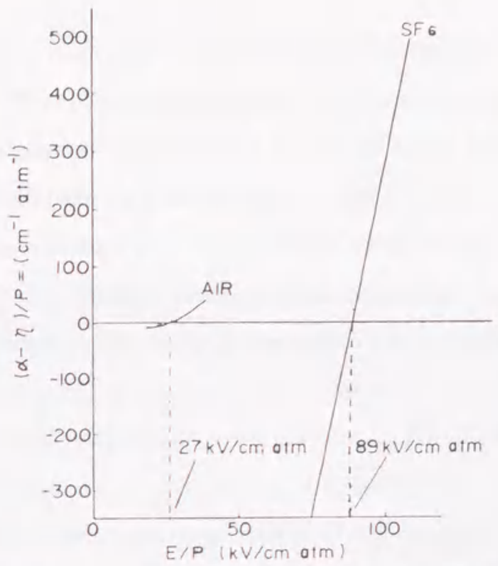

Fig. 1.1 Electric field dependence of effective ionization coefficient (α−η)/P of SF6 gas and air[6].

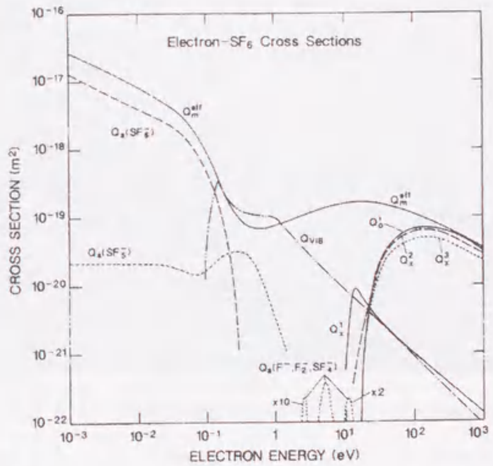

Fig. 1.2 Collision and attachment cross sections of SF6 gas[4].

Q_m^{eff}: effective momentum transfer
$Q_a(SF_6^-)$, $Q_a(SF_5^-)$, and $Q_a(F^-, F_2^-, SF_4^-)$: electron attachment
Q_{VIB}: vibrational excitation
Q_o^i: total ionization
Q_x^j(j = 1, 2, 3): electronic excitation

pressures of 0.4 MPa to 0.6 MPa. Then, SF_6 gas has been widely used for the electrical insulation of electric power apparatus such as Gas Insulated Switchgears (GIS)[2, 13 - 16], Cubicle-type GIS (C-GIS)[17], Gas Insulated Transmission Lines (GIL)[18, 19] and Gas Insulated Transformers[20, 21]. A typical 500 kV GIS is shown in Fig. 1.3. Such apparatus are filled with pressurized SF_6 gas inside the grounded metallic enclosure, which keeps the charged section unreachable and prevents from outside disturbance such as snow, ice, sandblast and humidity. Thus, the application of SF_6 gas insulated power apparatus into electric power transmission and distribution systems has been increasing rapidly and contributing to the electric power supply with high stability and quality. Especially in Japan, SF_6 gas insulated power apparatus have been introduced in almost all substations, which enables substations to be made much more compact into 5 to 10% in area and 2 to 3% in volume compared with those using air-insulated electric power apparatus[16].

Table 1.1 Physical and chemical properties of SF_6 gas.

Molecular weight	g/mol	146.06
Density (0.1013MPa, 25°C)	g/cm^3	6.089×10^{-3}
Sublimation point	°C	-63.8
Melting point	°C	-50.8
Critical temperature	°C	45.55
Critical pressure	MPa	3.759
Critical density	g/cm^3	0.737

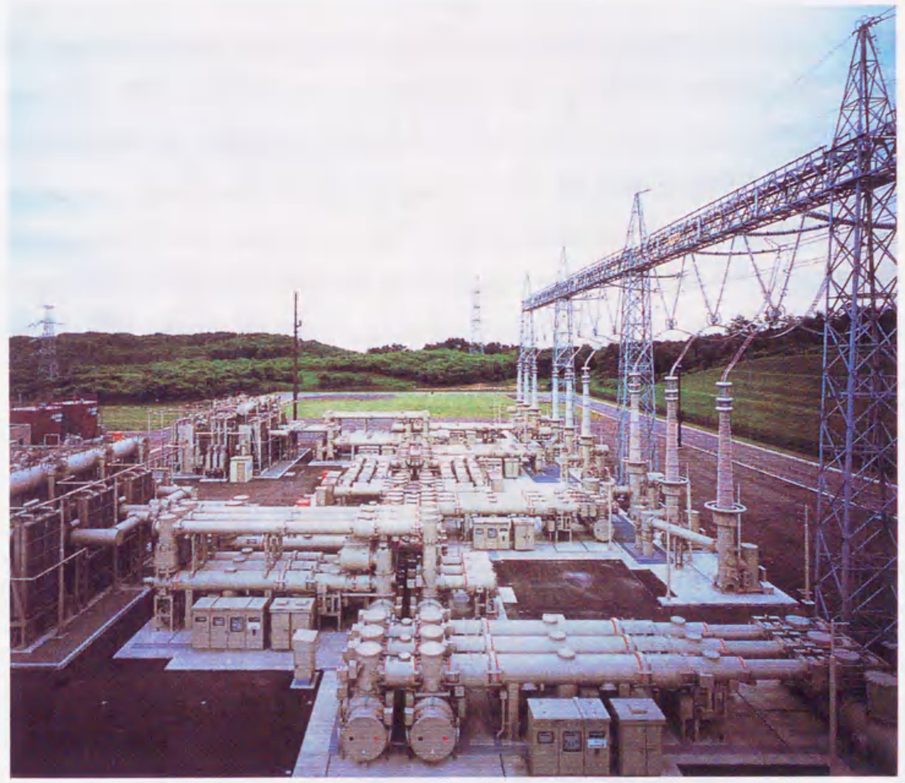

Fig. 1.3 A typical 500 kV SF_6 gas insulated switchgear.

1.3 Partial Discharge in Electric Power Apparatus

There is a possibility that conducting particles such as chip or dust of metallic materials may contaminate gas insulated electric power apparatus during their manufacturing and assembling processes. Such contaminants can stand up and lift off by the internal electric field in the testing or operation of the apparatus. They can move in the gap space of SF_6 gas and sometimes touch or be fixed on the high voltage conductor and on the solid insulators which support the high voltage conductors. Moreover, a void in the solid insulators and the surface roughness on the high voltage conductor could be arisen during their production process. The classification of defects in GIS is summarized in Fig. 1.4[22, 23].

Such defects produce a local enhancement of the electric field, which may cause a partial discharge (PD). This is because SF_6 gas has the effective ionization coefficient depending strongly on the electric field, as was previously shown in Fig. 1.1. PD could finally lead to the electrical

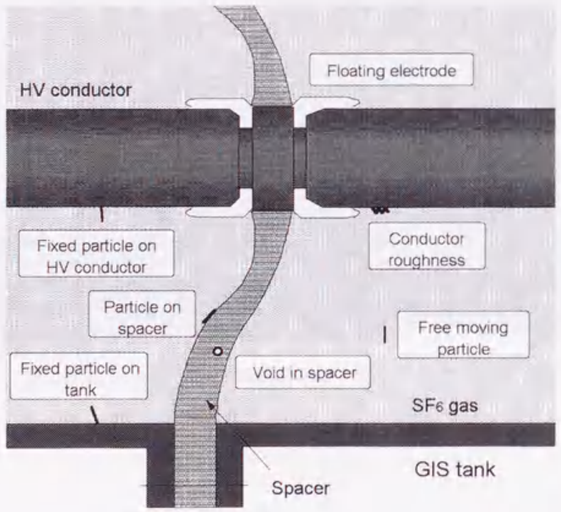

Fig. 1.4 Possible defects in GIS[22, 23].

breakdown in the apparatus[24], which is one of the major causes for the failure of the apparatus[25] and the obstruction of the electric power supply. The fixed particles on the solid dielectric surface and on the high voltage conductor and the free moving particles in the gap space are considered as the most dangerous conditions. This is because the electric field strength at the tip of the particles could easily become strong enough to generate PD in SF_6 gas and induce the breakdown, especially under the lightning and switching impulse voltage applications[22, 26]. This means that the electrical insulation property of SF_6 gas decreases sharply under inhomogeneous electric field distribution, although it is quite strong under homogeneous and quasi-homogeneous electric field distribution, as mentioned in the previous section. Figure 1.5 shows the gas pressure dependence of breakdown voltage in SF_6 gas under inhomogeneous electric field such as needle-plane electrode[27]. As can be seen in Fig. 1.5, breakdown voltage had non-linear relationship to the gas pressure. This is attributed to the PD-induced space charges, leading to the electric field relaxation around the needle tip, which is called "corona stabilization effect."

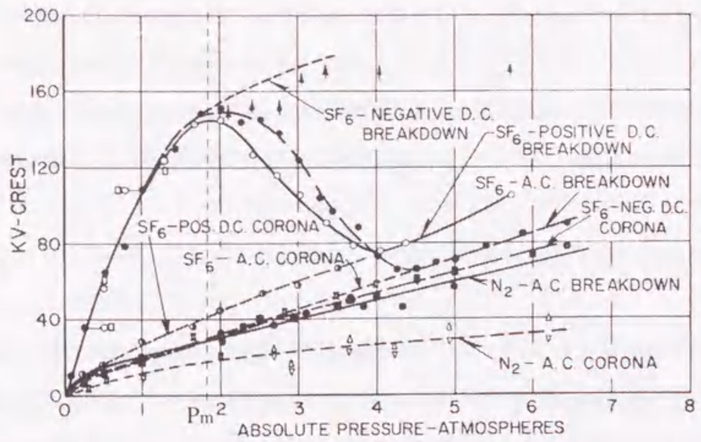

Fig. 1.5 Gas pressure dependence of breakdown and PD inception voltages for different kinds of applied voltage in SF_6 and N_2 gases[27].

Therefore, the detection techniques of PD in SF_6 gas with high sensitivity and accuracy are quite important for the stable operation of SF_6 gas insulated power apparatus. Moreover, they are expected to be developed into the insulation diagnosis, the breakdown and the lifetime prediction, and the preventive maintenance. The investigation of the PD detection techniques in the gas insulated power apparatus and PD phenomena in SF_6 gas have been intensively carried out in the last 40 years. In the following sections, the recent activities to investigate the PD detection techniques and PD phenomena will be introduced.

1.4 Partial Discharge Detection and Its Application to Electrical Insulation Diagnosis

PD is associated with a number of characteristic signals such as electromagnetic wave and light emission. Different kinds of techniques to detect such characteristic PD signals have been developed so far, which can be categorized by the object of detection as followings; electromagnetic wave, current pulse signal, acoustic emission signal, light emission intensity and image, and chemical decomposition. In this section, developed and developing PD detection techniques which are popular in the actual GIS are summarized together with signal processing and analyzing techniques in order to increase the accuracy and sensitivity of PD detection.

1.4.1 Electromagnetic Wave

PD in SF_6 gas is well known to be accompanied by a sharp current pulse with a rise time of less than 1 ns, which generates electromagnetic waves up to VHF and UHF bands[28]. The electromagnetic wave propagates in GIS with very low attenuation and is emitted from the aperture of GIS such as spacers and bushings[29]. In order to detect such electromagnetic wave signal with high sensitivity and low signal-to-noise ratio, many kinds of sensors inside and outside GIS have

been developed[29 - 36]. Recently, VHF and UHF sensors inside GIS are getting popular.

Figure 1.6 shows a typical disk-type UHF sensor[30]. The output signal was a voltage induced on the sensor by the electromagnetic wave and / or high frequency components of the transient signal propagating on the high voltage conductor. Such a sensor is occasionally called as a "coupler." Figure 1.7 shows a typical method to mount the UHF coupler in GIS[31]. It had a feature to allow no disturbance on the internal electric field, which is one of the most important properties for the sensor inside GIS. Goto *et al.* developed the spacer-embedded type PD sensor for detecting VHF signal (60 - 70 MHz), as shown in Fig. 1.8[32]. This sensor brought about no disturbance on the internal electric field as well as the electric field relaxation at the triple-junction. The minimum sensitivity of PD charge was reported to be several 10 pC. Judd *et al.* developed a spiral antenna of a self-complementary and log-periodic structure with the wide-band frequency response, combined with a wide-band coaxial balun to match the impedance between the spiral antenna and cable, as shown in Fig. 1.9[33]. They also constructed a coupler calibration system using GHz TEM (GTEM) cell, as shown in Fig. 1.10[37], which contributed to compare the PD detection sensitivity of different internal UHF sensors.

These internal sensors are sensitive and noiseproof, because the intrusion of external noise into GIS is quite small. However, internal sensors can be applied only to the new apparatus, hardly to the existing apparatus. Thus, several kinds of external sensors using UHF techniques have been developed for the existing apparatus. Maekawa *et al.* developed the external type PD sensor, as shown in Fig. 1.11[38]. This type of external PD sensor picked up the leakage electromagnetic wave out of the spacer, which had the same level of PD detection sensitivity as that of internal PD sensor such as the disk-type UHF sensor.

The electromagnetic wave signal propagates in GIS with not only TEM mode but also different modes such as TE_{11} and TM_{11}. Thus, there are many investigations for the propagation characteristics of the electromagnetic wave inside GIS including mode analyses[39 - 43]. Sakakibara *et al.* investigated the attenuation rate for the GIS components such as L-shaped bus, straight bus with insulating spacers, T-branch bus and open disconnectors[39]. As a result, they revealed the

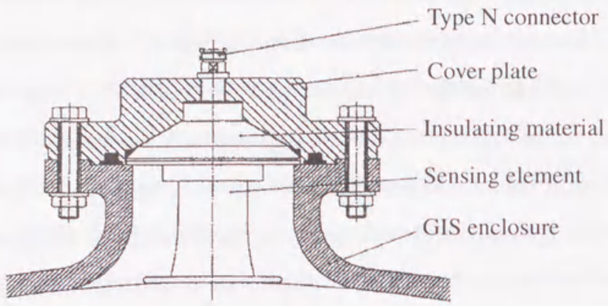

Fig. 1.6 UHF sensor[30].

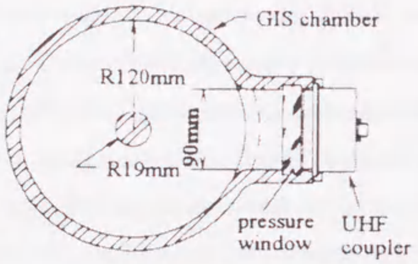

Fig. 1.7 UHF coupler mounted on observation window[31].

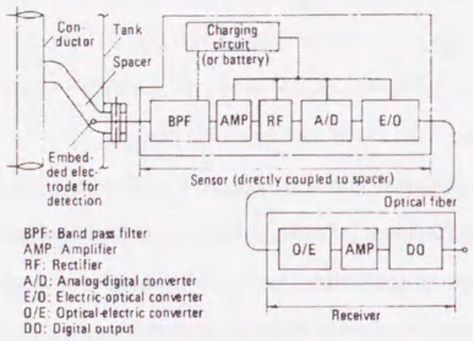

Fig. 1.8 Spacer-embedded type PD sensor and analysis system[32].

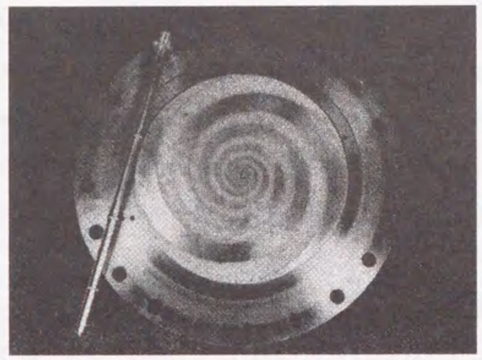

Fig. 1.9 Spiral antenna and wide-band coaxial balun[33].

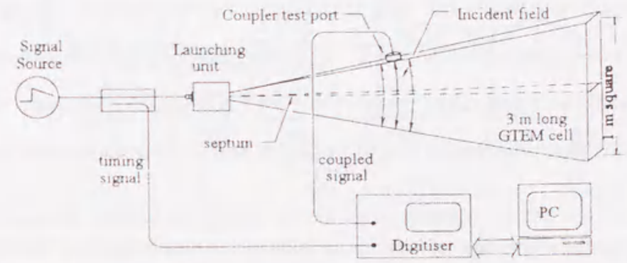

Fig. 1.10 GHz TEM (GTEM) cell and experimental setup for sensor calibration[37].

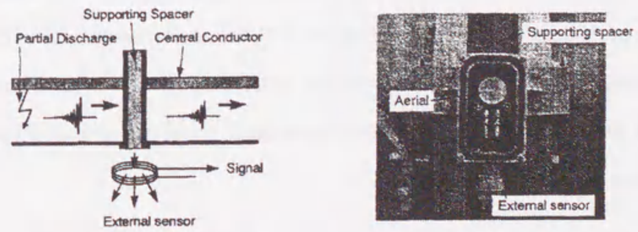

(a) Detection principle. (b) Mounting on GIS spacer.

Fig. 1.11 External type PD sensor[38].

existence of different attenuation characteristics; for example, in the case of L-shaped bus, electromagnetic wave signal attenuated at the frequency of around 400 MHz, while in the case of a straight bus provided with insulating spacers, attenuated at the frequency of around 100 MHz. Muto *et al.* investigated the dependence of frequency spectrum of measured electromagnetic wave signals on the angle between PD source and sensor, using the mode analysis[40]. They pointed out that the PD detection sensitivity could depend on the radial position of the sensor.

1.4.2 Current Pulse Signal

PD in SF_6 gas generates a current pulse with steep rise time, which flows on the grounded metal enclosure of GIS and finally flows out of the grounding line[44, 45]. The conventional PD detection method, regulated by IEC 270, is categorized in this method. The IEC 270 method detects the PD current pulse signal through C - R parallel circuit connected between GIS enclosure and the grounding line. Kurrer *et al.* reported that the PD detection sensitivity, which could be determined by the environmental noise, was equal to that of UHF method in a small GIS test setup[44].

PD current pulse signal has been measured mainly in the investigation of the PD phenomena, because PD current signal directly reflects the PD phenomena such as ionization and electron avaranche. Thus, it is significant for evaluating PD phenomena to measure PD current pulse waveform with high fidelity. Judd *et al.* measured free particle-induced PD current pulse waveforms in SF_6 gas at the pressure of 0.48 MPa by a digitizer with the analog bandwidth of 5 GHz and the sampling rate of about 100 GS/s[46]. Compensating with the transfer function of measuring cable and equipment, they revealed that PD current pulse had a steep rise time of 50 ps and a pulse width of 70 ps, as shown in Fig. 1.12.

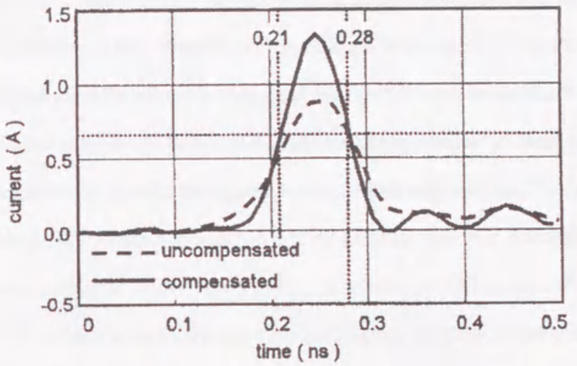

Fig. 1.12 Free particle-induced PD current pulse waveform measured by a high-speed digitizer[46].

1.4.3 Noise Reduction and Signal Processing

Since PD signal detected by different sensors mentioned above can be distorted by external noises, the noises should be reduced in order to keep high sensitivity and reliability of the PD detection. Moreover, the detected PD signal should be analyzed to identify and locate the PD source and to diagnose the insulation condition. Thus, many techniques for the noise reduction and signal processing have been developed.

As for the noise reduction techniques, selection of measuring frequency region[47, 48] and time domain region[47, 49], filtering using wavelet analysis[50] and adaptive filter[51, 52], etc. have been developed. Hikita *et al.* investigated the frequency components of PD in air and SF_6 gas[47]. They pointed out that the selective PD measurement with the higher frequency components could discriminate PD in SF_6 gas under noisy condition. Li *et al.* developed noise extraction algorithm using discrete wavelet analysis for the noise reduction of PD signal measured by the UHF technique[50].

As for the signal processing techniques, characterization of measured PD data by Phase Resolved PD (PRPD) pattern[48, 53 - 55], and the extraction of the featuring characteristics using the Neural Networks (NN)[56, 57], etc. have been developed. Tsurimoto *et al.* succeeded to identify PD sources on the basis of frequency dependence of PD signal and PRPD pattern[48]. Lapp *et al.* classified the PD sources by the relationship between the differences in voltage and phase for two consecutive PD pulses[54]. Oki *et al.* applied NN to the location of PD source using the spacer-embedded type electromagnetic sensors and simulated pulse injection method[56].

1.5 Investigations of Partial Discharge Mechanisms in SF_6 Gas

1.5.1 Breakdown Prediction Technique Based on Partial Discharge Measurement

PD can induce the electrical breakdown, as mentioned in Section 1.3. A few investigations have been carried out for the breakdown prediction by means of the PD measurement.

Okubo *et al.* reported the temporal transition of PD characteristics for a long term until breakdown, as shown in Fig. 1.13[24]. In Fig. 1.13, the charge magnitude of PD increased with time under the constant voltage application. Especially, at the stage just before the breakdown in Fig. 1.13 (f), a PD pulse with relatively large magnitude of charge was generated at the phase region of positive applied voltage peak. This was due to the temporal change of the needle tip shape, which increased the generation probability of the leader-type PD and decreased the breakdown voltage.

In order to recognize the leader-type PD from a number of PD pulses, Okubo *et al.* carried out the simultaneous measurement of a current pulse waveform and corresponding light emission image for a single PD in SF_6 gas under ac voltage application, as shown in Fig. 1.14[58]. They classified PD into two categories; a streamer-type PD with single-peak current pulse observed mainly at lower gas pressure region $P \leq P_m$ where the breakdown voltage took its maximum value as shown in Fig. 1.5, and a leader-type PD with multiple-peak current pulse leading to the breakdown observed mainly at $P \geq P_m$. They also simultaneously measured the light intensity waveforms for different wavelength components and current pulse waveform for single PD with multi peaks, as shown in Fig. 1.15[59]. They revealed that the ratio of the red light component to the blue one for the second peak was larger than that for the first one, which was the evidence of the leader-type PD.

The transition mechanism from the streamer-type PD to the leader-type PD has been also investigated, especially under the steep-front pulse voltage application. Gallimberti *et al.* simultaneously measured the current pulse waveform, the streak image and the Schlieren pictures

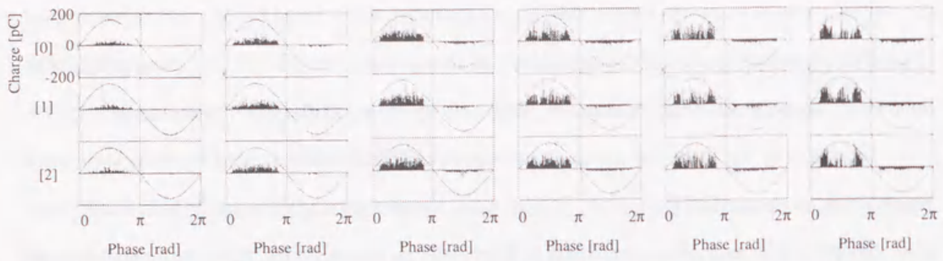

(a) 1 min. (b) 10 min. (c) 30 min. (d) 60 min. (e) 100 min. (f) 149 min.

Fig. 1.13 PD phase characteristics from PD inception to breakdown for a long time ac voltage application[24].

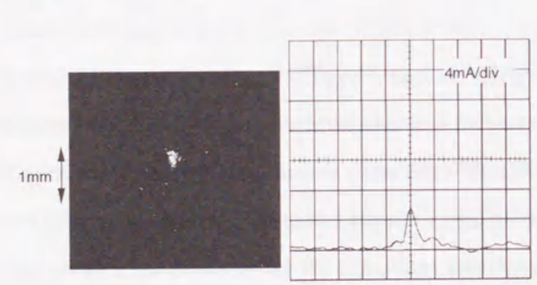

(a) Streamer-type PD.

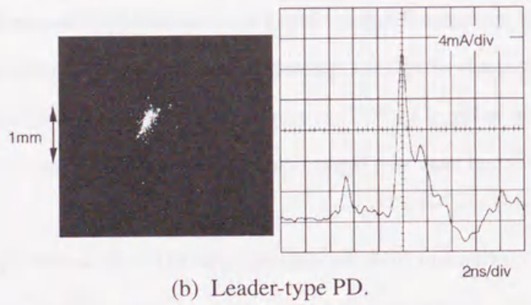

(b) Leader-type PD.

Fig. 1.14 Light emission image and current pulse waveform for a single PD in SF_6 gas under ac voltage application[58].

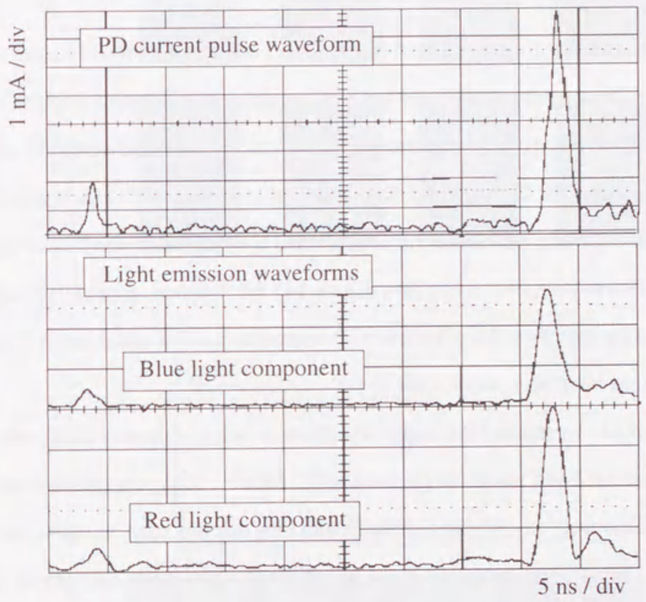

Fig. 1.15 PD current pulse waveform with multi peaks and corresponding light emission waveforms for different wavelength components[59].

for a single PD in SF_6 gas under positive impulse voltage application, as shown in Fig. 1.16[60]. They observed the double-peak PD current pulse and leader channel in the Schlieren and the streak records.

1.5.2 Sequential Partial Discharge Characteristics and Space Charge Behavior

Some investigations for the leader-type PD have been carried out so far, however, most of them were under the steep-front pulse voltage application such as lightning impulse voltage[60 - 62], which was due to the space charge free environment. Space charges generated by the preceding PD pulse would distort the electric field distribution at around the PD source and fluctuate the generation probability of the initial electron. Therefore, it is important for the breakdown prediction in the actual GIS under operation to investigate PD mechanism, especially sequential PD characteristics taking the space charge behavior into account, under ac and dc conditions. However, a few investigations have been carried out so far.

Fréchette *et al.* investigated the sequential characteristics of negative PD under dc voltage condition in pressurized SF_6 gas at the pressure of 0.5 MPa[63]. They reported that the magnitude of PD current pulse waveform correlated strongly with time that preceded, as shown in Fig. 1.17.

As for the space charge behavior, some investigations have been carried out. Van Brunt *et al.* calculated the limiting values of ion mobility k_ℓ for two ion trajectories under ac condition, in order to verify the influence of negative ions in the negative ac half cycle on the positive PD inception in the subsequent positive ac half cycle, as shown in Fig. 1.18[64]. The negative ions would be accumulated in the gap space when the mobility of the ion was smaller than the solid line of corresponding ion trajectory, while they would reach the opposite plane electrode when the ion mobility was larger than the solid line. They confirmed that at higher gas pressure region, the calculation result corresponded to the reduction of positive PD inception voltage, because a greater amount of negative ions generated by negative PD could remain in the gap space just before the polarity reversal. Pfeiffer *et al.* introduced a simplified extension model for a streamer-

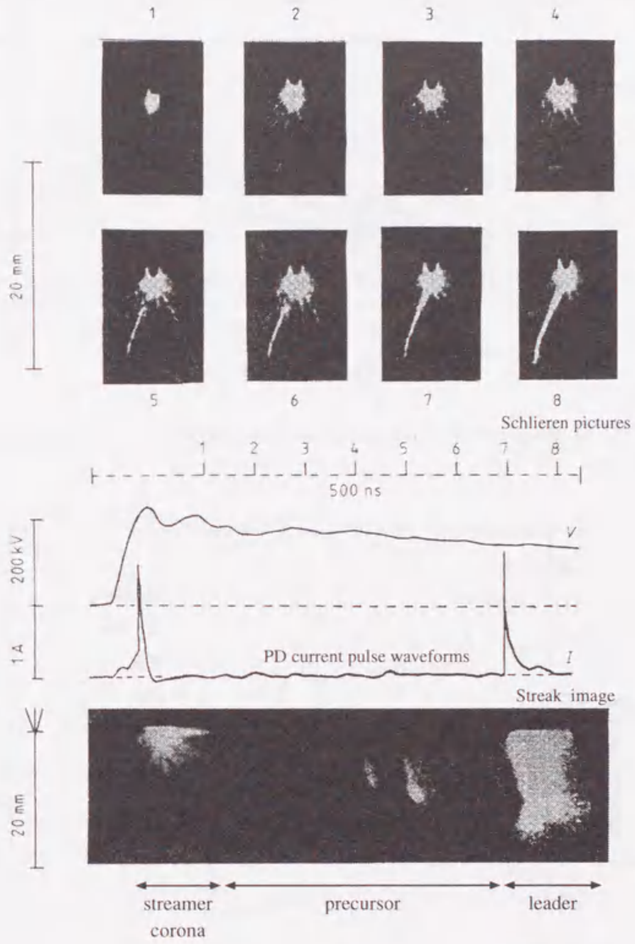

Fig. 1.16 Schlieren pictures, current pulse waveform and streak image for a single PD in SF_6 gas under positive impulse voltage application[60].

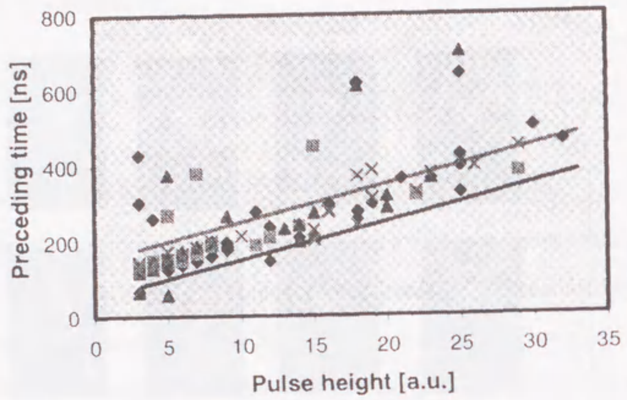

Fig. 1.17 Relationship between preceding time and negative PD current pulse height[63].

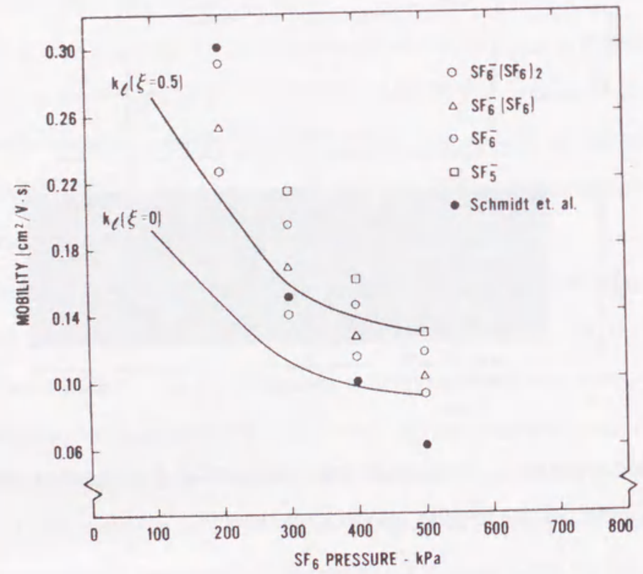

Fig. 1.18 Limiting value of ion mobility for different two ion trajectories[64].

type and a leader-type PD, as shown in Fig. 1.19[65]. They determined the streamer radius r_c as the distance from leader tip to the point where the electric field strength was equal to the critical electric field of the gas medium, and revealed that r_c corresponded to the observed ionization volume with PD light emission, as shown in Fig. 1.20.

A few numerical simulations for the sequential PD characteristics have been carried out. Okabe *et al.* calculated the sequential positive PD current pulses for the steep-rise dc voltage condition by a multichannel model, which had coaxial multi channels outside a single PD channel[66]. They achieved the successive PD current pulses, as shown in Fig. 1.21, with consideration of bidirectional drift and diffusion of ions.

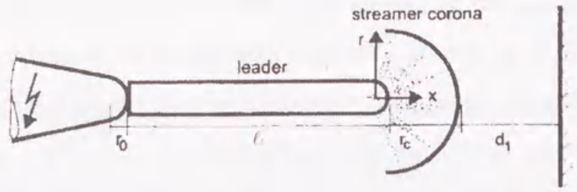

Fig. 1.19 Simplified extension model for streamer-type PD and leader-type PD[65].

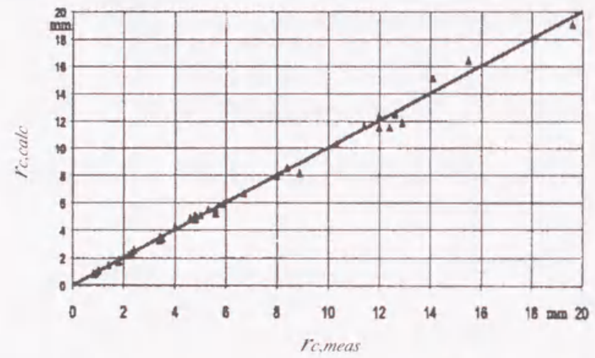

Fig. 1.20 Comparison of measured corona radii $r_{c,meas}$ and the calculated corona radii, $r_{c,calc}$[65].

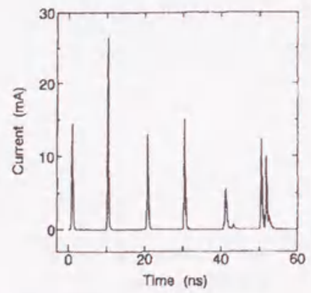

Fig. 1.21 Sequential PD current pulses simulated with multichannel model with consideration of bidirectional drift and diffusion of ions[66].

1.6 Purpose and Composition of the Dissertation

As mentioned in the previous sections, PD measurement techniques in SF_6 gas insulated electric power apparatus have been developed for their reliable insulation diagnosis. However, the present PD measurement focuses mainly on the magnitude and the voltage phase information of PD signals within the limit of the detection sensitivity. The pattern matching of PD characteristics is also based on the empirical data obtained by the laboratory experiments for different kinds of defects. In other words, they are hardly based on the physical phenomena of PD in SF_6 gas. Thus, in order to establish reliable and efficient insulation diagnosis for SF_6 gas insulated power apparatus, PD phenomena and their mechanisms should be elucidated through the precise PD measurement techniques. Especially, space charge behavior may play an important role for PD inception, extension and breakdown, so that PD mechanism should be investigated with consideration of space charge behavior.

From these viewpoints, this dissertation focuses on the relationship between space charge behavior and PD mechanism in SF_6 gas under ac voltage condition. Through the selective PD measurement using high sensitive and time-resolved techniques, statistical and sequential PD characteristics are investigated for different experimental conditions. Moreover, the propagation characteristics of PD-induced electromagnetic wave in long-distance GIL model are discussed.

The composition of this dissertation is as follows;

Chapter 2 Partial Discharge Mechanism in SF_6 Gas with Consideration of Space Charge Behavior

In Chapter 2, PD characteristics under ac voltage condition are described. Firstly, measuring systems for PD current pulse waveform and for light emission of PD are established with high frequency techniques. Then, PD characteristics are investigated with different power frequencies and electrode configurations, and discussed taking account of the space charge behavior. Finally, a model of the space charge behavior and PD generation mechanism is proposed.

Chapter 3 Sequential Generation Characteristics of Partial Discharges in SF_6 Gas with Consideration of Space Charge Behavior and Corona Stabilization

In Chapter 3, a measuring system for sequential PD generation characteristics with high time-resolution is firstly constructed. Then, the sequential PD generation characteristics are measured for ac and positive dc voltage conditions and are discussed on the relationship between PD charge and preceding time from viewpoint of the space charge behavior and corona stabilization effect. Finally, a model for the space charge behavior between sequential two PD pulses is suggested.

Chapter 4 Long-term Sequential Characteristics of Negative Partial Discharge in Pressurized SF_6 Gas

In Chapter 4, negative PD characteristics under higher gas pressure condition are observed with long-term, high time-resolution PD measuring system. Moreover, temporal transition of the negative PD characteristics is measured for 6 hours. Experimental results are discussed with consideration of space charge behavior and generation mechanism of the initial electron attributed to the temporal change of the electrode surface condition.

Chapter 5 Propagation Characteristics of Electromagnetic Wave Caused by Partial Discharge in Long-distance Gas Insulated Transmission Line

In Chapter 5, simultaneous measurement of PD current pulse waveforms and corresponding electromagnetic waveforms in a full-scale 275 kV class GIL model are described. Propagation and attenuation characteristics of the electromagnetic wave in GIL are discussed from viewpoint of the amplitude of waveforms and each frequency component achieved by the wavelet analysis.

Chapter 6 Summary

In Chapter 6, the composition of this dissertation is summarized and the scope for the future research is also given.

References

[1] Energy Information Administration: "International Energy Outlook 2000", Office of Integrated Analysis and Forecasting, U.S. Department of Energy, Washington, D.C., pp. 113-131, March, 2000.

[2] Y.Yamagata, N.Shimoda, M.Ohno, M.Kobayashi, Y.Shimizu and K.Sasamori: "Field Tests on Current Carrying Performances of 1000 kV GIS", *1999 IEEE Transmission and Distribution Conference*, Vol. 2, pp. 495-500, 1999.

[3] E.Harada, H.Nogiwa, S.Maruyama, K.Ogata, H.Yamada and K.Ogawa: "Application of Electronic Secondary Technologies to 1000 kV Gas-insulated Switchgear and Transformers", *1999 IEEE Transmission and Distribution Conference*, Vol. 2, pp. 509-516, 1999.

[4] A.V.Phelps and R.J.Van Brunt: "Electron-transport, Ionization, Attachment, and Dissociation Coefficients in SF_6 and Its Mixtures", *Journal of Applied Physics*, Vol. 64, No. 9, pp. 4269-4277, 1988.

[5] L.G.Christophorou and R.J.Van Brunt: "SF_6/N_2 Mixtures - Basic and HV Insulation Properties", *IEEE Transactions on Dielectrics and Electrical Insulation*, Vol. 2, No. 5, pp. 952-1003, 1995.

[6] T.Nitta and Y.Shibuya: "Electrical Breakdown of Long Gaps in Sulfur Hexafluoride", *IEEE Transactions on Power Apparatus and Systems*, Vol. 90, No. 3, pp. 1065-1071, 1971.

[7] S.A.Boggs: "Sulphur Hexafluoride: Introduction to the Material and Dielectric", *IEEE Electrical Insulation Magazine*, Vol. 5, No. 5, pp. 18-21, 1989.

[8] R.G.A.R.Maclagan: "Symmetry, Ionic Structures and *d* Orbitals in SF_6", *Journal of Chemical Education*, Vol. 57, No. 6, pp. 428-429, 1980.

[9] A.E.Reed and F.Weinhold: "On the Role of *d* Orbitals in SF_6", *Journal of American Chemical Society*, Vol. 108, No. 13, pp. 3586-3593, 1986.

[10] A.R.Ravishankara, S.Solomon, A.A.Turnipseed and R.F.Warren: "Atmospheric Lifetimes of Long-lived Halogenated Species", *Science*, Vol. 259, pp. 194-199, 1993.

[11] G.Cliteur, K.Suzuki, H.Ikeda and S.Yanabu: "A Collisional-radiative SF_6 Arc Plasma Model Using Boltzmann Analysis", *IEEE Transactions on Plasma Science*, Vol. 25, No. 5, pp. 996-1000, 1997.

[12] A.Gleizes, B.Rahmani, J.J.Gonzalez and B.Liani: "Calculation of Net Emission Coefficient in N_2, SF_6 and SF_6-N_2 Arc Plasmas", *Journal of Physics D: Applied Physics*, Vol. 24, pp. 1300-1309, 1991.

[13] H.Toda, Y.Ozaki, I.Miwa, S.Nishiwaki, Y.Murayama and S.Yanabu: "Development of 800 kV Gas-insulated Switchgear", *IEEE Transactions on Power Delivery*, Vol. 7, No. 1, pp. 316-323, 1992.

[14] T.Hasegawa, K.Yamaji, M.Hatano, F.Endo, T.Rokunohe and T.Yamagiwa: "Development of Insulation Structure and Enhancement of Insulation Reliability of 500 kV dc GIS", *IEEE Transactions on Power Delivery*, Vol. 12, No. 1, pp. 194-202, 1997.

[15] S.M.Ghufran Ali and W.D.Goodwin: "The Design and Testing of Gas-insulated Metalclad Switchgear and Its Application to EHV Substations", *Power Engineering Journal*, Vol. 2, No. 1, pp. 17-25, 1988.

[16] S.Yanabu, Y.Murayama and S.Matsumoto: "SF_6 Insulation and Its Application to HV Equipment", *IEEE Transactions on Electrical Insulation*, Vol. 26, No. 3, pp. 358-366, 1991.

[17] J.Sato, T.Shioiri, M.Miyagawa, T.Yoshida and K.Yokokura: "Composite Insulation Technology for New Compact 72/84 kV C-GIS", *1999 IEEE Transmission and Distribution Conference*, Vol. 2, pp. 489-494, 1999.

[18] A.Sabot: "Insulation Co-ordination Procedure for 420 kV Gas Insulated Lines (GIL)", *11th International Symposium on High Voltage Engineering*, Vol. 3, pp. 1-10, 1999.

[19] T.Nojima, M.Shimizu, A.Miyazaki, T.Araki, H.Nishima, H.Hata, H.Yamaguchi, T.Yamauchi and M.Miyashita: "Study on an After-laying Test for a Long-distance GIL", *IEEE Transactions on Power Delivery*, Vol. 13, No. 3, pp. 718-727, 1998.

[20] E.Takahashi, K.Tanaka, K.Toda, M.Ikeda, T.Teranishi, M.Inaba and T.Yanari: "Development of Large-capacity Gas-insulated Transformer", *IEEE Transactions on Power Delivery*, Vol. 11, No. 2, pp. 895-902, 1996.

[21] K.Hiraishi, Y.Uwano, K.Shirakura, Y.Gotanda, K.Endoo, M.Higaki, M.Horikoshi, K.Mizuno and H.Hora: "Development and Practical Operation of Perfluorocarbon Immersed 275 kV Transformers with Compressed SF_6 Gas Insulation", *IEEE Transactions on Power Delivery*, Vol. 10, No. 2, pp. 880-888, 1995.

[22] R.Haller, W.Hauschild and W.Mosch: "High-voltage Field Testing of GIS from a Physical View-point", *2nd International Conference on Properties and Applications of Dielectric Materials*, Vol. 2, pp. 746-749, 1988.

[23] R.Baumgartner, B.Fruth, W.Lanz and K.Pettersson: "Partial Discharge - Part IX: PD in Gas-insulated Substations - Fundamental Considerations", *IEEE Electrical Insulation Magazine*, Vol. 7, No. 6, pp. 5-13, 1992.

[24] H.Okubo, T.Kato, N.Hayakawa and M.Hikita: "Temporal Development of Partial Discharge and Its Application to Breakdown Prediction in SF_6 Gas", *IEEE Transactions on Power Delivery*, Vol. 13, No. 2, pp. 440-445, 1998.

[25] A.Sabot, A.Petit and J.P.Taillebois: "GIS Insulation Co-ordination: On-site Tests and Dielectric Diagnostic Techniques, a Utility Point of View", *IEEE Transactions on Power Delivery*, Vol. 11, No. 3, pp. 1309-1316, 1996.

[26] T.Hasegawa, K.Yamaji, M.Hatano, H.Aoyagi, Y.Taniguchi and A.Kobayashi: "dc Dielectric Characteristics and Conception of Insulation Design for dc GIS", *IEEE Transactions on Power Delivery*, Vol 11, No. 4, pp. 1776-1782, 1996.

[27] C.N.Works and T.W.Dakin: "Dielectric Breakdown of Sulfur Hexafluoride in Nonuniform Fields", *Transactions on American Institute of Electrical Engineers*, Vol. 72, pp. 682-689, 1953.

[28] S.M.Neuhold, M.L.Schmatz, M.Hässig, M.M.Spühler and G.Strof: "Combined Broad and Narrow Band Multichannel PD Measurement System with High Sensitivity for GIS", *11th International Symposium on High Voltage Engineering*, Vol. 5, pp. 152-155, 1999.

[29] M.Kozako, Z.H.Tian, N.Shibata and M.Hikita: "Reduction of Continuous and Pulse-shape Noise by Digital Signal Processing for Reliable PD Detection in HV Substations", *11th International Symposium on High Voltage Engineering*, Vol. 5, pp. 168-171, 1999.

[30] N.de Kock, B.Coric and R.Oietsch: "UHF PD Detection in Gas-insulated Switchgear - Suitability and Sensitivity of the UHF Method in Comparison with the IEC 270 Method", *IEEE Electrical Insulation Magazine*, Vol. 12, No. 6, pp. 20-26, 1996.

[31] M.D.Judd, B.F.Hampton and W.L.Brown: "UHF Partial Discharge Monitoring for 132 kV GIS", *10th International Symposium on High Voltage Engineering*, Vol. 4, pp. 227-230, 1997.

[32] K.Goto, T.Sakakibara, I.Kamata and S.Ikeda: "On-line Monitoring and Diagnostics of Gas Circuit Breakers", *IEEE Transactions on Power Delivery*, Vol. 4, No. 1, pp. 375-381, 1989.

[33] M.D.Judd, O.Farish and B.F.Hampton: "Broadband Couplers for UHF Detection of Partial Discharge in Gas-insulated Substations", *IEE Proceedings - Science, Measurement and Technology*, Vol. 142, No. 3, pp. 237-243, 1995.

[34] G.Schöffner and W.Boeck: "PD Measurements in N_2-SF_6 Gas Mixtures with the UHF Method", *11th International Symposium on High Voltage Engineering*, Vol. 5, pp. 86-89, 1999.

[35] B.F.Hampton and R.J.Meats: "Diagnostic Measurements at UHF in Gas Insulated Substations", *IEE Proceedings*, Vol. 135, Pt. C, No. 2, pp. 137-144, 1988.

[36] R.Kurrer and K.Feser: "The Application of Ultra-high-frequency Partial Discharge Measurements to Gas-insulated Substations", *IEEE Transactions on Power Delivery*, Vol. 13, No. 3, pp. 777-782, 1998.

[37] M.D.Judd, O.Farish and P.F.Coventry: "UHF Couplers for GIS - Sensitivity and Specification", *10th International Symposium on High Voltage Engineering*, Vol. 6, pp. 121-124, 1997.

[38] H.Maekawa, T.Ito and E.Yajima: "GIS Monitoring Sensors", *4th International Conference on Advances in Power System Control, Operation and Management*, Vol. 2, pp. 773-778, 1997.

[39] T.Sakakibara, H.Murase, E.Haginomori, S.Wakabayashi, K.Emoto and A.Ogawa: "Study of Propagation Phenomena of Partial Discharge Pulses in Gas Insulated Substation", *IEEE Transactions on Power Delivery*, Vol. 13, No. 3, pp. 768-776, 1998.

[40] H.Muto, M.Doi, H.Fujii and M.Kamei: "Resonance Characteristics and Identification of Modes of Electromagnetic Wave Excited by Partial Discharges in GIS", *11th International Symposium on High Voltage Engineering*, Vol. 5, pp. 70-73, 1999.

[41] M.D.Judd, O.Farish and B.F.Hampton: "The Excitation of UHF Signals by Partial Discharges in GIS", *IEEE Transactions on Dielectrics and Electrical Insulation*, Vol. 3, No. 2, pp. 213-228, 1996.

[42] H.Imagawa, K.Emoto, H.Murase, H.Koyama, R.Tsuge, S.Maruyama and T.Sakakibara: "Partial Discharge Propagation Characteristics in GIS and Realizability of Its Location System by Frequency Components Comparison", *1999 IEEE Transmission and Distribution Conference*, Vol. 2, pp. 526-533, 1999.

[43] S.Meijer, E.Gulski, J.J.Smit and A.J.L.M.Kanters: "Determination of PD Sensitivity of GIS Using Signal Reduction Measurements", *1998 IEEE International Symposium on Electrical Insulation*, Vol. 1, pp. 65-68, 1998.

[44] R.Kurrer, K.Klunzinger, K.Feser, N.de Kock and D.Sologuren: "Sensitivity of the UHF method for Defects in GIS with Regard to On-line Partial Discharge Detection", *1996 IEEE International Symposium on Electrical Insulation*, Vol. 1, pp. 95-98, 1996.

[45] M.Knapp, R.Feger, K.Feser and A.Breuer: "Application of the CIGRE-sensitivity Verification for UHF PD Detection in Three-phase GIS", *11th International Symposium on High Voltage Engineering*, Vol. 5, pp. 82-85, 1999.

[46] M.D.Judd and O.Farish: "High Bandwidth Measurement of Partial Discharge Current Pulses", *1998 IEEE International Symposium on Electrical Insulation*, Vol. 2, pp. 436-439, 1998.

[47] M.Hikita, T.Hoshino, T.Kato, N.Hayakawa, T.Ueda and H.Okubo: "Discrimination of Partial Discharge Electromagnetic Signal in SF_6 Gas from External Noises Using Phase Gate Control Method", *1996 IEEE International Symposium on Electrical Insulation*, Vol. 1, pp. 117-120, 1996.

[48] T.Tsurimoto, H.Muto, M.Doi, K.Ito and H.Fujii: "Correlation between Two Frequency Components of Various PD Pulses in GIS", *1998 International Symposium on Electrical Insulating Materials*, pp. 653-656, 1998.

[49] A.Lehtio, P.Oakonen, K.Kannus and E.Lakervi: "Recognition of Electrical Discharges in SF_6 and Atmospheric Air by RFI Measurements", *1992 Conference on Electrical Insulation and Dielectric Phenomena*, pp. 370-375, 1992.

[50] Z.M.Li, Y.P.Feng, J.Q.Chen and X.Z.Zhang: "UHF Partial Discharge Monitoring in GIS and Signal Processing", *1998 International Symposium on Electrical Insulating Materials*, pp. 67-70, 1998.

[51] M.Kozako, Z.Tian, H.Okubo, N.Shibata and M.Hikita: "Noise Reduction and PD Measurements Using Digital Filter and Signal Processing Technique in HV Substations", *1998 International Symposium on Electrical Insulating Materials*, pp. 561-564, 1998.

[52] A.Zargari and T.R.Blackburn: "Application of Adaptive Filters for the Estimation of Partial Discharge Signals in Noisy Environments", *5th International Conference on Properties and Applications of Dielectric Materials*, Vol. 1, pp. 212-215, 1997.

[53] E.Gulski: "Digital Analysis of Partial Discharges", *IEEE Transactions on Dielectrics and Electrical Insulation*, Vol. 2, No. 5, pp. 822-837, 1995.

[54] A.Lapp and H.-G.Kranz: "The Use of the CIGRE Data Format for PD Diagnosis Applications", *IEEE Transactions on Dielectrics and Electrical Insulation*, Vol. 7, No. 1, pp. 102-112, 2000.

[55] S.Meijer, E.Gulski, J.J.Smit and R.Brooks: "Digital Analysis of Multiple Faults in GIS", *1998 IEEE International Symposium on Electrical Insulation*, Vol. 1, pp. 69-72, 1998.

[56] I.Oki, T.Haida, S.Wakabayashi, R.Tsuge, T.Sakakibara and H.Murase: "Development of Partial Discharge Monitoring Technique Using a Neural Network in a Gas Insulated Substation", *1996 IEEE Transmission and Distribution Conference*, pp. 189-196, 1996.

[57] H.-G.Kranz: "Diagnosis of Partial Discharge Signals Using Neural Networks and Minimum Distance Classification", *IEEE Transactions on Electrical Insulation*, Vol. 28, No. 6, pp. 1016-1024, 1993.

[58] H.Okubo, M.Yoshida, A.Suzuki, T.Kato, N.Hayakawa and M.Hikita: "Discrimination of Partial Discharge Type in SF_6 Gas by Simultaneous Measurement of Current Waveform and Light Emission", *1996 IEEE International Symposium on Electrical Insulation*, Vol. 1, pp. 107-110, 1996.

[59] M.Yoshida, T.Takahashi, M.Hikita, H.Watanabe, N.Hashimoto and H.Okubo: "Investigation of Partial Discharge Mechanism by Simultaneous Measurement of Current Waveform and Light Emission", *Electrical Engineering in Japan*, Vol. 129, No. 4, pp. 58-65, 1999.

[60] I.Gallimberti and N.Wiegart: "Streamer and Leader Formation in SF_6 and SF_6 Mixtures under Positive Impulse Conditions: II. Streamer to Leader Transition", *Journal of Physics D: Applied Physics*, Vol. 19, No. , pp. 2363-2379, 1986.

[61] L.Niemeyer: "Leader Breakdown in Compressed SF_6: Recent Concepts and Understanding", *Gaseous Dielectrics VI*, pp. 49-59, Plenum Press, New York, 1991.

[62] N.Wiegalt, L.Niemeyer, F.Pinnekamp, W.Boeck, J.Kindersberger, R.Morrow, W.Zaengl, M.Zwicky, I.Gallimberti and S.A.Boggs: "Inhomogeneous Field Breakdown in GIS - The Prediction of Breakdown Probabilities and Voltages - Part III: Discharge Development in SF_6 and Computer Model of Breakdown", *IEEE Transactions on Power Delivery*, Vol. 3, No. 3, pp. 939-946, 1988.

[63] M.F.Fréchette, C.Hudon, M.Germain, R.Y.Larocque, S.Matsumoto and T.Umemura: "On the Stochastic Nature of SF_6 Partial Discharges Close to Onset Conditions", *2000 IEEE International Symposium on Electrical Insulation*, pp. 390-394, 2000.

[64] R.J.Van Brunt and M.Misakian: "Mechanisms for Inception of dc and 60-Hz ac Corona in SF_6", *IEEE Transactions on Electrical Insulation*, Vol. 17, No. 2, pp. 106-120, 1982.

[65] W.Pfeiffer, D.Schoen and C.Zender: "Corona Stabilisation in SF_6/N_2 Mixtures under VFT Stress", *11th International Symposium on High Voltage Engineering*, Vol. 3, pp. 84-87, 1999.

[66] S.Okabe, M.Sato and T.Hara: "Simulation of Positive Corona Discharge in SF_6 Gas by Multichannel Model When Bidirectional Diffusion of Ions is Considered", *1998 IEEE International Symposium on Electrical Insulation*, Vol. 1, pp. 309-312, 1998.

Chapter 2 Partial Discharge Mechanism in SF_6 Gas with Consideration of Space Charge Behavior

2.1 Introduction

PD phenomena in SF_6 gas are so faint and fast that PD measurement with high accuracy has many difficulties, and that PD mechanism based on space charge behavior has not been fully understood yet[1, 2]. Particularly, PD phenomena under ac voltage condition are considered to be much influenced by space charges generated by PD with counter polarity in the preceding half cycle[3]. Thus, in order to investigate the PD mechanism with consideration of space charge behavior, PD characteristics under ac voltage condition with variable frequency higher than the commercial power frequency are considered to be informative. Moreover, on-site testing for GIS with higher frequency application has been introduced[4], however, the effect of the applied power frequency on the PD mechanism and observed PD signal has not been discussed yet.

This chapter aims to clarify the PD mechanism and the space charge behavior affecting PD mechanism under ac voltage condition in terms of the voltage phase dependence of the PD characteristics. The main experimental parameters in this chapter are the frequency of the applied ac voltage, the radius of the needle tip and the gap length. Firstly, the measuring system for PD current pulse waveforms with wide-band frequency range from dc to over 1 GHz, and that for PD light emission images with large expansion rate are developed. Using such electrical and optical PD measuring systems, PD characteristics are investigated under ac voltage application with different frequencies and electrode configurations, as well as under positive dc voltage application. Based on these experimental results, the physical mechanism of PD in SF_6 gas under ac voltage application is discussed with consideration of space charge behavior.

2.2 Experimental Setup for Partial Discharge Measurements

2.2.1 Partial Discharge Generating System

Figure 2.1 shows the high voltage sources and the experimental system to generate PD in SF_6 gas. A needle electrode made of stainless steel with the length ℓ = 20 mm was fixed on the high voltage conductor of a 66 kV class model GIS in order to simulate the condition of the metallic particle contamination in the GIS. A needle-plane electrode system was built in the model GIS to make an inhomogeneous electric field configuration. Figure 2.2 shows the model GIS and Fig. 2.3 shows the electrode setup built at the end section of GIS.

As high voltage sources, three kinds of high voltage sources were used; a testing transformer (frequency f = 60 Hz), a rectifier unit and a variable frequency ac high voltage transformer. Tables 2.1, 2.2 and 2.3 show the specifications of the ac 60 Hz testing transformer, the rectifier unit, and the variable frequency ac high voltage source, respectively. The rectifier unit consists of two diodes and capacitors. The schematic diagram of the variable frequency ac voltage source is already shown in Fig. 2.1. As can be seen in Table 2.3, it can generate ac high voltage with the frequency from 120 to 600 Hz and the voltage up to 75 kV_{rms}. To generate such a high voltage, a sinusoidal wave of a designated wave signal is amplified by a power amplifier and a testing transformer.

2.2.2 Measuring System for Partial Discharge Current Pulse Waveforms

In order to measure a PD current pulse waveform in SF_6 gas as accurate as possible, the frequency range of the measuring devices such as a detecting impedance and an oscilloscope should be as wide as possible. In this experiment, PD current pulse waveform was measured by a high-speed digital oscilloscope (Tektronics TDS684B, sampling rate: 5 GS/s, analog bandwidth: 1 GHz) through the plane electrode and a detecting impedance. Figure 2.4 shows the experimental

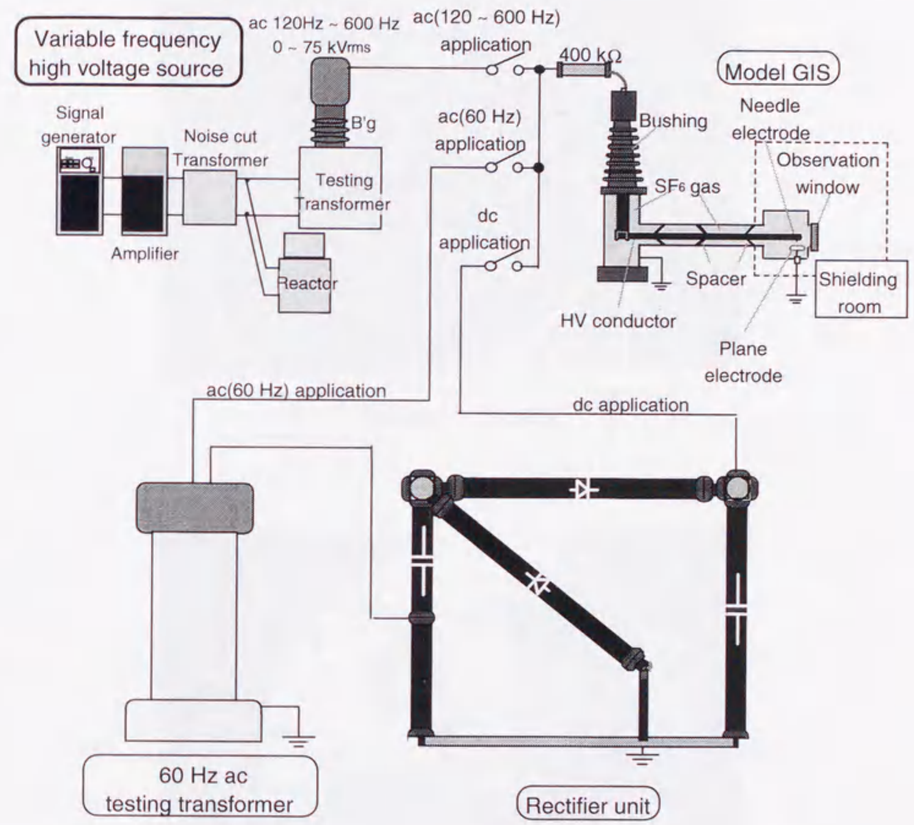

Fig. 2.1 Experimental setup for PD generation and high voltage circuit.

Fig. 2.2 Model GIS.

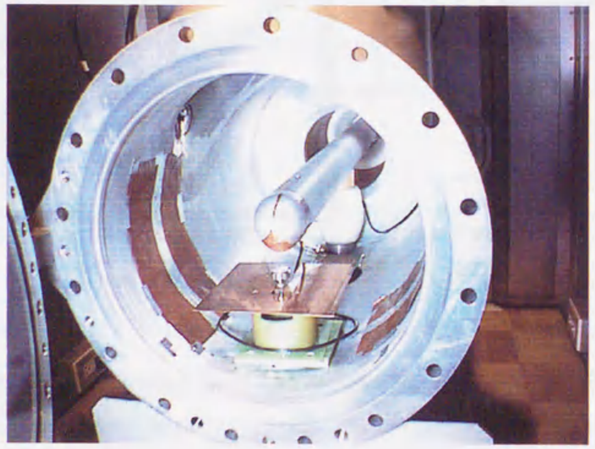

Fig. 2.3 Electrode setup and GIS end section.

Table 2.1 Specifications of testing transformer.

Rated voltage	250 kV_{rms}
Maximum output voltage	250 kV_{rms}
Rated frequency	60 Hz
Rated output current	0.12 A
Maximum output power	30 kVA
Operation mode	continuous operation

Table 2.2 Specifications of rectifier unit.

Rated voltage	350 kV
Maximum output voltage	350 kV
Rated current	5 mA (at 350 kV)
Ripple	≤ 3%
Maximum output power	2 kW
Operation mode	continuous operation

Table 2.3 Specifications of variable frequency ac high voltage transformer.

Rated voltage	75 kV_{rms}
Maximum output voltage	75 kV_{rms}
Rated frequency	120 ~ 600 Hz
Rated output current	0.43 A
Maximum output power	32 kVA
Operation mode	continuous operation

setup for PD current pulse measurement. For the detecting impedance, a chip-type impedance with a wide-band frequency range up to 1 GHz and more was used. This impedance had some features as follows;(1) Characteristic impedance of 50 Ω; which makes well matching to measuring cables. (2) High wattage of 250 W; which brings about strong surge-proof at breakdown. (3) Ceramics package; which permits to use it under vacuum or high gas pressure conditions. The circuit diagram, the top view of the matching circuit and the frequency characteristics of its voltage standing wave ratio (VSWR) are shown in Figs. 2.5 (a), (b) and (c), respectively. The frequency characteristics of VSWR was measured by a network analyzer (ANRITSU MS4662A, 100 kHz ~ 3 GHz). As can be seen in Fig. 2.5 (c), its VSWR was less than 3 up to 1 GHz and more, which proved that the impedance could be used from dc to 1 GHz and more.

Here, in order to guard the measuring equipment from the surge pulses generated at breakdown, a surge protector using an operational amplifier with a wide-band frequency range was placed between the impedance and the measuring equipment. The circuit diagram, external view, frequency characteristics and input - output characteristics are shown in Figs. 2.6 (a), (b), (c) and (d), respectively. As can be seen in Fig. 2.6 (c), its frequency characteristics, measured by the network analyzer (MS4662A), were flat up to 1.2 GHz. Moreover, the input - output characteristics in Fig. 2.6 (d) showed that the amplitude of output signal was saturated at the input signal with the amplitude of larger than 1.7 V. When a surge pulse was inputted into the surge protector, the operational amplifier was broken immediately to prevent the measuring equipment from failure.

In the case of ac voltage application, a signal synchronized with the applied ac voltage phase was inputted into the oscilloscope in order to trigger it at the designated applied voltage phase region. The triggering gate signal was generated by a pulse generator, which was triggered by the zero-cross signal of the applied ac high voltage. Therefore, the selection of the appropriate delay time and pulse width of the gate signal realized the measurement of PD current pulse waveform at the designated applied ac voltage phase region.

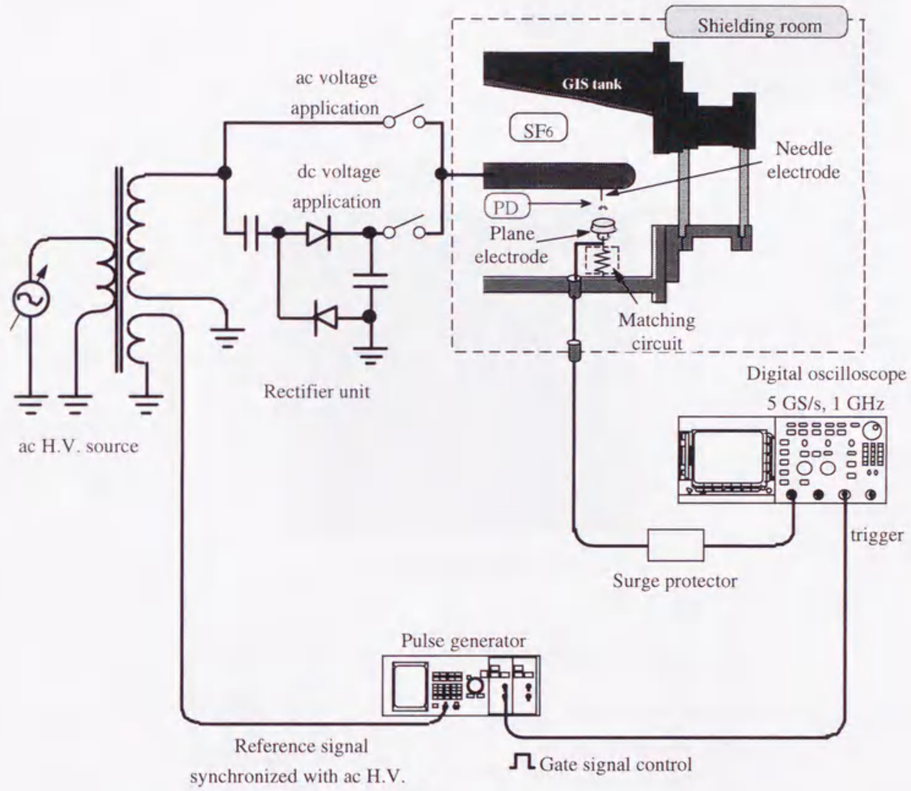

Fig. 2.4 Experimental setup for measuring PD current pulse waveform.

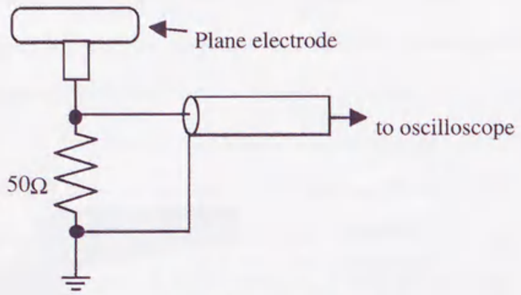

(a) Circuit diagram.

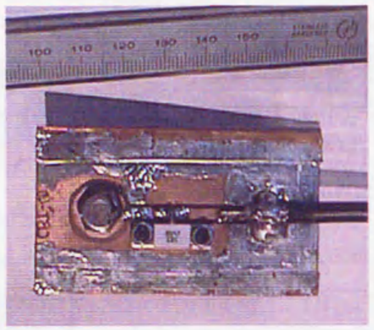

(b) Top view.

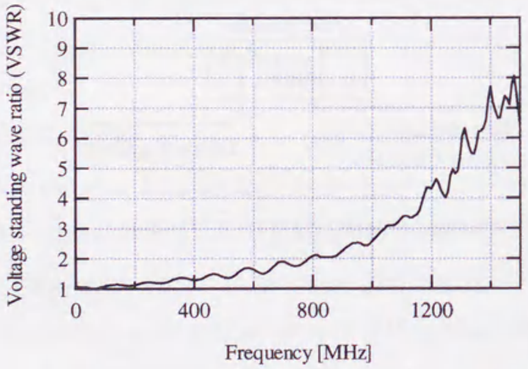

(c) Frequency characteristics of voltage standing wave ratio (VSWR).

Fig. 2.5 Specifications of matching circuit.

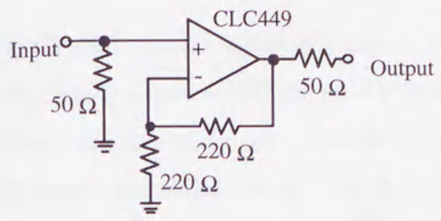

(a) Circuit diagram.

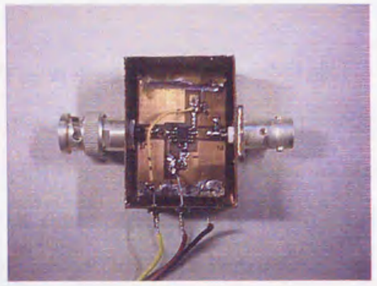

(b) Top view.

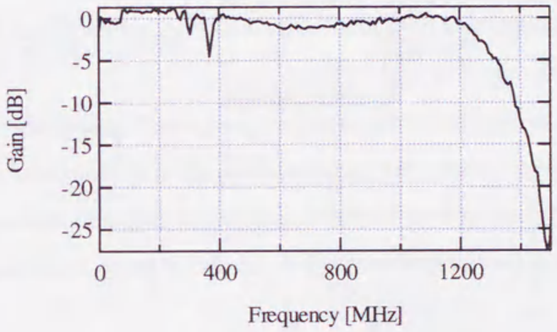

(c) Frequency characteristics

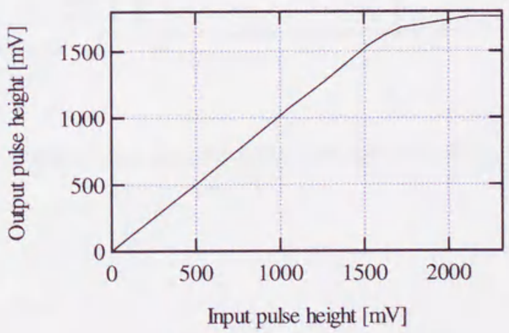

(d) Input - output characteristics.

Fig. 2.6 Specifications of surge protector.

2.2.3 Measuring System for Partial Discharge Light Emission Images

In order to recognize the type of PD and to measure the extension length of PD, PD light emission image and its intensity waveform should be observed. The measuring system for PD light emission images was established with an image intensifier and optical lenses, as shown in Fig. 2.7. PD light emission image was expanded by the lenses set inside and outside GIS, amplified by the image intensifier and recorded by a still camera. The expansion rate was approximately 20 times. PD light intensity was observed by two types of photo multiplier tubes (PMT-B and -R) and a digital oscilloscope (TDS684B) through dielectric mirrors and optical lenses, in order to observe PD light intensity waveforms for two different spectral ranges, 420 nm ~ 540 nm and 630 nm ~ 700 nm, respectively.

Under ac voltage condition, a trigger pulse in designated applied voltage phase was led into the image intensifier to record PD light emission image at the designated phase region. To generate the gate pulse, the same technique as mentioned in the previous subsection was used. Moreover, the exposure time was controlled by the number of pulses and frequency of the gate pulses.

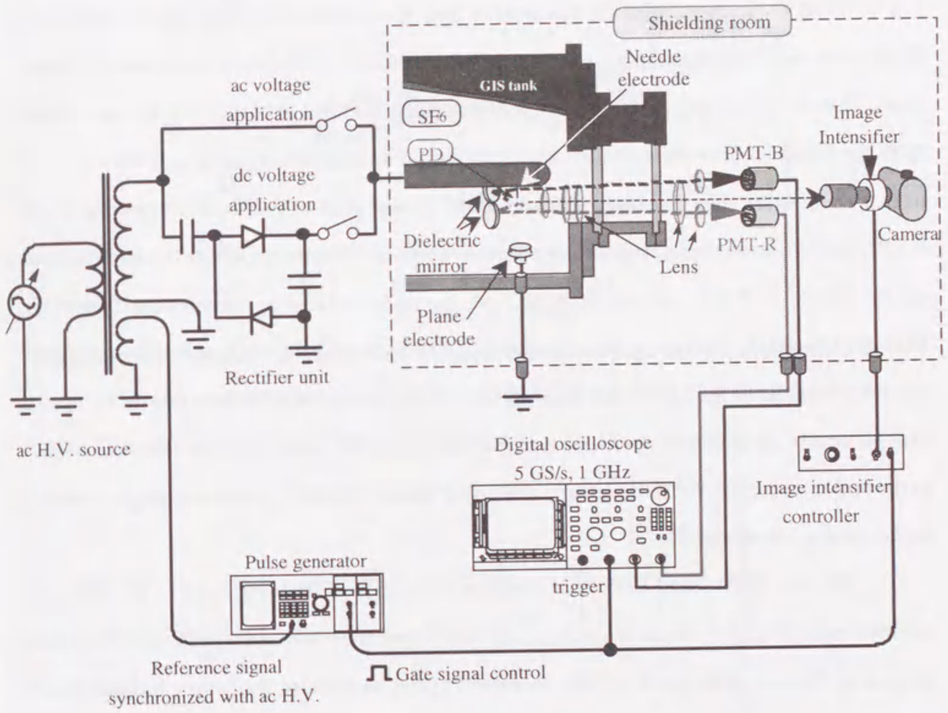

Fig. 2.7 Experimental setup for measuring light emission image of PD.

2.3 Partial Discharge Inception and Breakdown Voltages

Figure 2.8 shows the positive and negative PD inception voltages (PDIV+, PDIV-) and the breakdown voltage (BDV) as a function of the gas pressure for the applied power frequency f = 60 and 400 Hz at the gap length g = 10mm and the needle tip radius r = 500 μm. As can be seen in Fig. 2.8, PDIV- increased with the gas pressure and was independent of the power frequency. PDIV+ also increased with the gas pressure, however, clearly decreased with the increase of the power frequency from 60 to 400 Hz and finally reached the level of PDIV-. On the other hand, BDV for f = 60 Hz once increased as the gas pressure P increased to P_m at which BDV reached its maximum value, then decreased suddenly to the voltage level of PDIV+ at the pressure P_c. At $P \geq P_c$, BDV increased again with the gas pressure. This non-linearity of BDV curve also appeared for f = 400 Hz. At $P \leq P_m$, where the breakdown would be induced by the streamer-type PD[5], BDV for f = 400 Hz had almost the same value as that for f = 60 Hz, while at $P \geq P_m$, where the breakdown would be induced by the leader-type PD[5], it kept higher value than that for f = 60 Hz. This is because the generation probability of the leader-type PD would decrease with the increase in the power frequency due to the greater amount of space charges remaining in the gap space at higher power frequency.

PDIV+, PDIV- and BDV as a function of the power frequency at P = 0.1 MPa are summarized in Fig. 2.9. As shown in Fig. 2.9, PDIV- and BDV were irrespective of the power frequency. On the other hand, PDIV+ decreased as the increase in the power frequency and became the same level as PDIV- at $f \geq 300$ Hz.

In the following sections, PD characteristics at $P \leq P_m$, especially at P = 0.1 MPa are described, in order to compare the PD characteristics at the identical values of the applied ac voltage for different power frequencies. This is due to the similarities in BDV at $P \leq P_m$ as shown in Fig. 2.8, which means that the breakdown is always induced by the extension of the streamer-type PD.

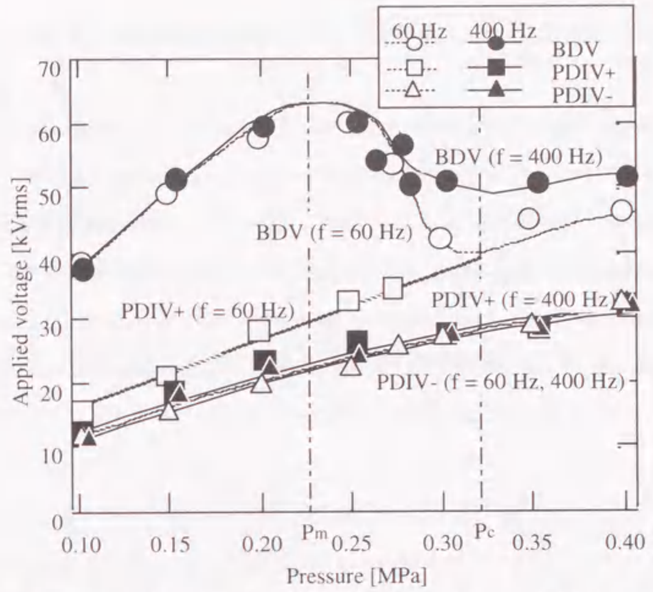

Fig. 2.8 PD inception voltage (PDIV) and breakdown voltage (BDV) characteristics as a function of gas pressure for f = 60 Hz and f = 400 Hz ac voltage application. (g = 10 mm, r = 500 μm, in SF_6 gas.)

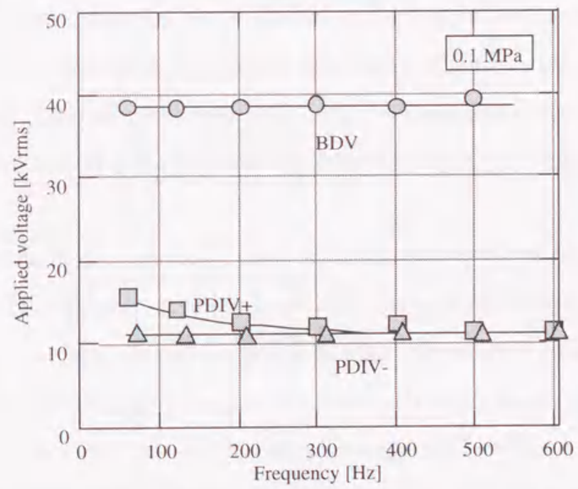

Fig. 2.9 Power frequency dependence of positive and negative PD inception voltage (PDIV+, PDIV-) and breakdown voltage (BDV). (g = 10 mm, r = 500 μm, in SF_6 gas, P = 0.1 MPa.)

2.4 Partial Discharge Current Pulse Waveforms under ac Voltage Conditions

Figures 2.10 (a) ~ (d) show typical PD current pulse waveforms observed at voltage phase 30° and 200° for f = 60 Hz, at 40° and 200° for f = 400 Hz, respectively, in the vicinities of the positive and negative PD inception phases for both applied power frequencies at the applied voltage $V_a = 30\,kV_{rms}$. As seen in Fig. 2.10, not only the pulse height but also the waveforms of PD current pulses were quite different at each frequency. In positive PD, the pulse height for f = 60 Hz in Fig. 2.10 (a) was larger than that for f = 400 Hz in Fig. 2.10 (c). In negative PD, the pulse height for f = 60 Hz in Fig. 2.10 (b) was smaller than that for f = 400 Hz in Fig. 2.10 (d).

PD occur one after another and their characteristics depend on the applied voltage phase as shown in Fig. 2.11. In Fig. 2.11, some of the PD current pulses could not be measured due to the short of the sampling rate of the measuring equipment, especially the oscilloscope. In order to observe the voltage phase characteristics of PD as precise as possible, the similar experiments as shown in Fig. 2.10 were carried out for different phase regions. A single ac cycle was divided into 36 regions (every 10°) and the current pulse waveforms were measured 30 times for each phase region. Figure 2.12 shows the phase dependence of PD current pulse height at g = 10 mm, r = 500 μm, f = 60 Hz and $V_a = 30\,kV_{rms}$. Note that each PD current pulse waveform achieved in the measurement had a pulse-like waveform with a steep wave front. As can be seen in Fig. 2.12, only at around positive PD inception phase (30° ~ 40°), PD had large magnitude of PD current pulse height.

In order to clarify the influence of the electric field distribution and the space charge behavior on the positive PD characteristics under ac voltage condition, PD characteristics were measured under different electrode conditions, as shown in Fig. 2.13. In Fig. 2.13 (a) at g = 10 mm, r = 500 μm and f = 400 Hz, which was a higher power frequency condition than the case in Fig. 2.12, a positive PD current pulse height increased with the phase and took the maximum value at around 130°. In Fig. 2.13 (b) at g = 10 mm, r = 200 μm and f = 60 Hz, whose needle tip radius was smaller than the case in Fig. 2.12, PD current pulse height increased with

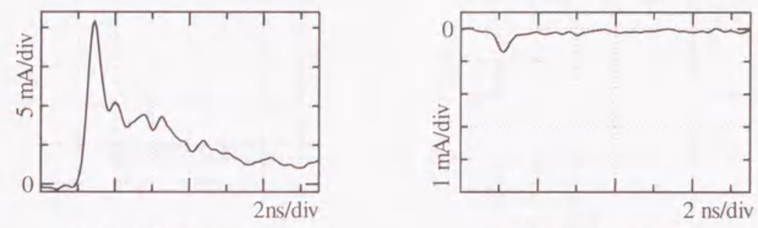

(a) f = 60 Hz, ϕ = 30°.
(b) f = 60 Hz, ϕ = 200°.
(c) f = 400 Hz, ϕ = 40°.
(d) f = 400 Hz, ϕ = 200°.

Fig. 2.10 Typical PD current pulse waveforms.
(g = 10 mm, r = 500 μm, in SF_6 gas, P = 0.1 MPa, $V_a = 30\,kV_{rms}$.)

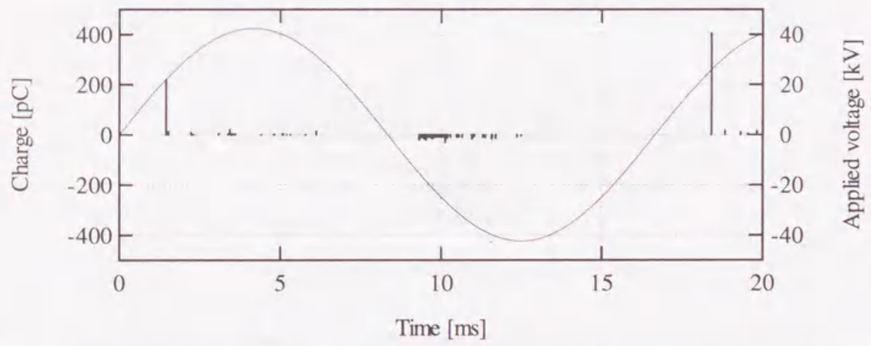

Fig 2.11 Typical sequential generation characteristics of PD current pulse under ac condition.

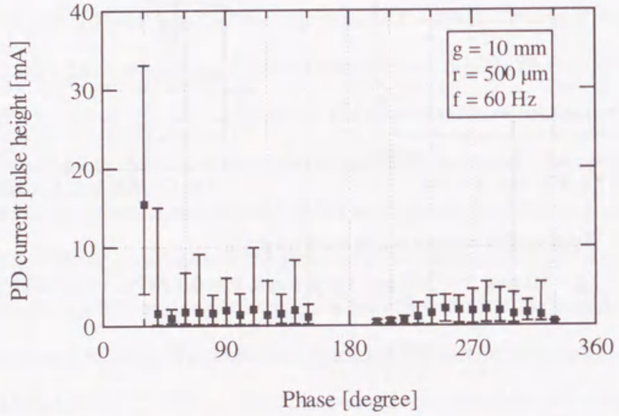

Fig. 2.12 Phase dependence of PD current pulse height under ac condition.
(g = 10 mm, r = 500 μm, in SF_6 gas, P = 0.1 MPa, f = 60 Hz, V_a = 30 kV_{rms}.)

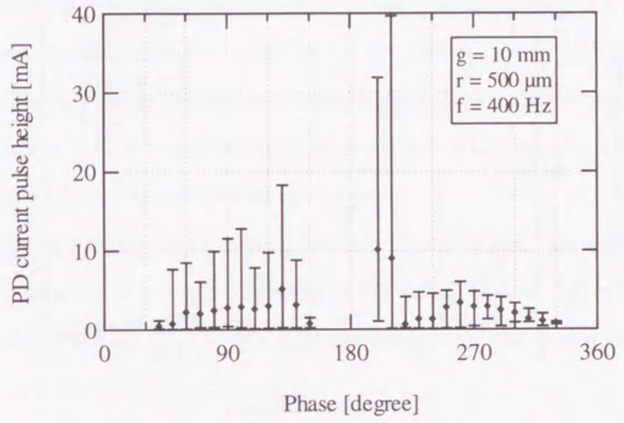

(a) g = 10 mm, r = 500 μm and f = 400 Hz.

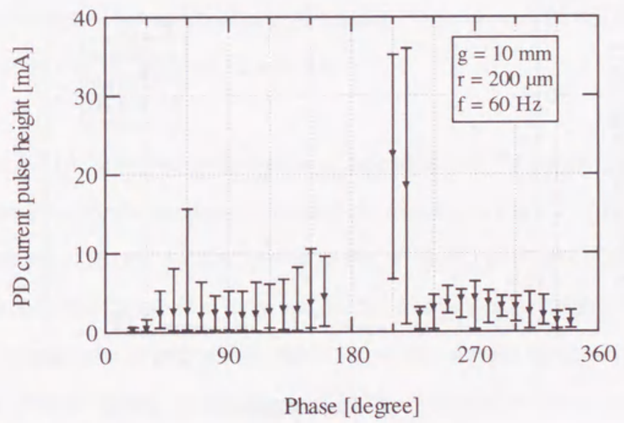

(b) g = 10 mm, r = 200 μm and f = 60 Hz.

Fig. 2.13 Phase dependence of PD current pulse height under ac condition.
(in SF_6 gas, P = 0.1MPa, V_a = 30 kV_{rms}.)

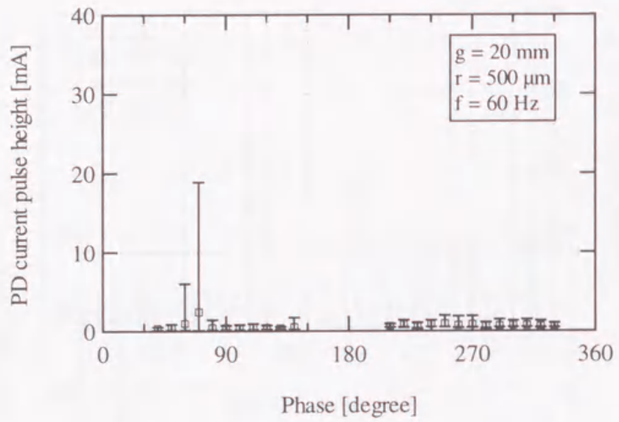

(c) g = 20 mm, r = 500 μm and f = 60 Hz.

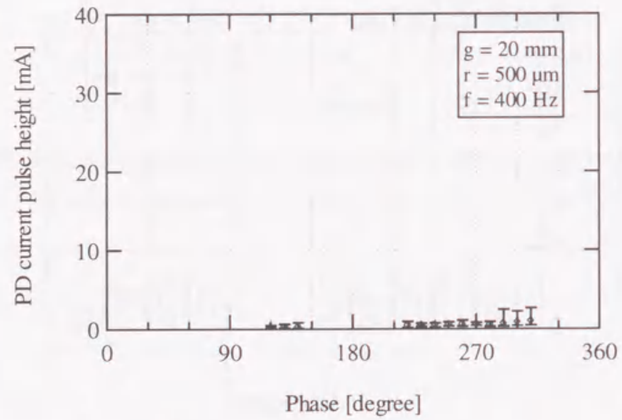

(d) g = 20 mm, r = 500 μm and f = 400 Hz.

Fig. 2.13 Phase dependence of PD current pulse height under ac condition. (in SF_6 gas, P = 0.1 MPa, V_a = 30 kV_{rms}.) continued.

the phase at around PD inception phase (20° ~ 60°) and was followed by PD with relatively small magnitude of PD current pulse height. In Fig. 2.13 (c) at g = 20 mm, r = 500 μm and f = 60 Hz, which was larger gap length condition than the case in Fig. 2.12, PD current pulse height increased with the applied voltage phase at around positive PD inception phase, and was followed by small ones at the subsequent phase regions. On the contrary, for g = 20 mm, r = 500 μm and f = 400 Hz in Fig. 2.13 (d), which was longer gap length and higher power frequency conditions than the case in Fig. 2.12, PD in positive half cycle had only small magnitude of current pulse at the narrow phase region after the applied voltage peak.

Comparison of positive PD characteristics in Figs. 2.12 and 2.13 suggests that Fig. 2.12 can be discriminated from the others in terms of PD pattern with the larger magnitude of PD current pulse at around the positive PD inception phase. This can be explained by the space charge behavior to be described in Section 2.7.

2.5 Comparison of Partial Discharge Characteristics between under ac and under Positive dc Voltage Conditions

Figure 2.14 shows the applied voltage dependence of PD current pulse height under positive dc condition for the same gap configurations as those in Figs. 2.13 (c) and (d), that is, g = 20 mm and r = 500 μm. As can be seen in Fig. 2.14, PD only at just above positive PD inception voltage (32.1 kV) had the large magnitude of current pulse height.

PD characteristics in Figs. 2.13 (c), (d) and 2.14 were compared in terms of the instantaneous value of applied voltage. Figure 2.15 shows the instantaneous voltage dependence of PD current pulse height at (a) 0° ~ 90° and (b) 90° ~ 180° under ac condition and that under positive dc condition. Figures 2.15 (a) and (b) also include PD characteristics under the gap configuration of g = 20 mm and r = 500 μm, at V_a = 54 kV_{rms} for f = 60 Hz. In Fig. 2.15 (a), PD current pulse height at around PD inception voltage under positive dc condition was different

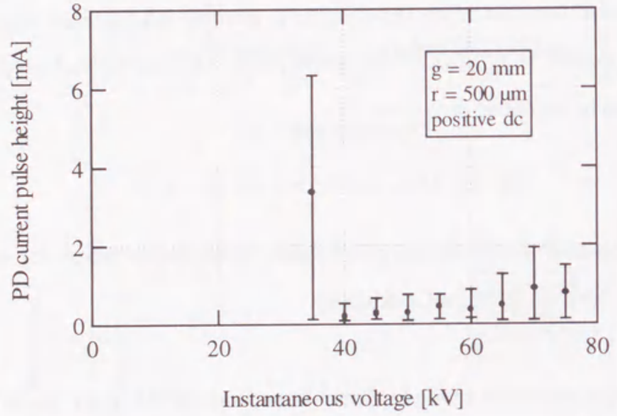

Fig. 2.14 Phase dependence of PD current pulse height under positive dc condition.
(g = 20 mm, r = 500 μm, in SF_6 gas, P = 0.1 MPa.)

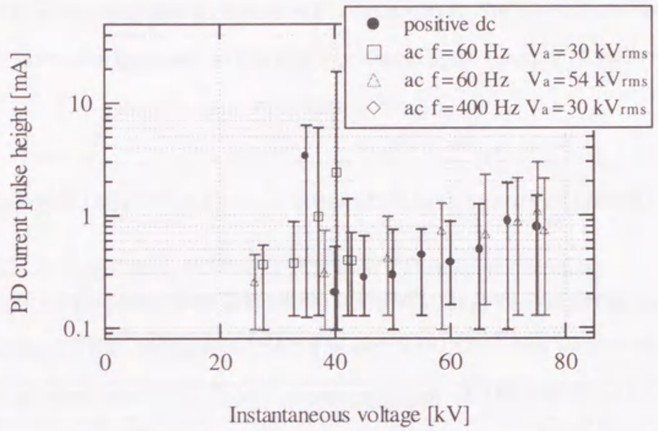

(a) Voltage phase 0° ~ 90°.

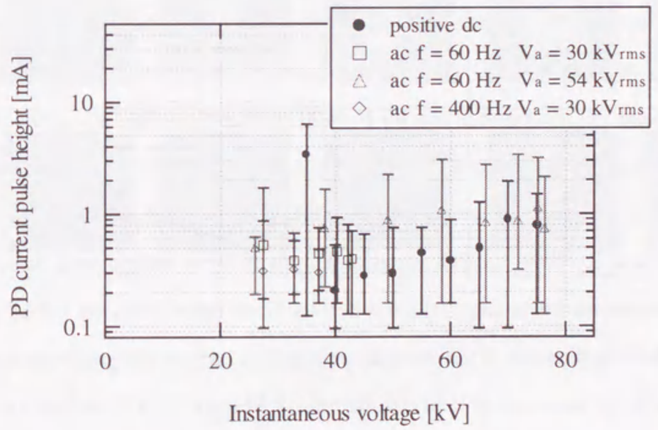

(b) Voltage phase 90° ~ 180°.

Fig. 2.15 PD current pulse height characteristics as a function of instantaneous value of applied voltage under positive dc and ac conditions.
(g = 20 mm, r = 500 μm, in SF_6 gas, P = 0.1 MPa.)

from that at PD inception phase under ac condition, although PD inception voltage were different from each experimental condition to the other, due to the fluctuation. Except at around the PD inception region, PD characteristics under ac and under positive dc conditions agreed with each other in terms of the instantaneous voltage dependence. The difference and agreement in PD characteristics can be also explained by space charge behavior, which will be discussed in Section 2.7.

2.6 Light Emission Image and Extension Length of Partial Discharge

Table 2.4 shows light emission images of positive PD under ac condition of g = 20 mm and r = 500 μm at around positive PD inception phase, peak phase and PD extinction phase, respectively, for f = 60 and 400 Hz. As can be seen in Table 2.4, PD light emission images at each phase region for f = 60 Hz and at 130° for f = 400 Hz were brush-like, where the pulse-like PD current waveforms were observed as was shown in Figs. 2.13 (c) and (d). The results of such optical and electrical PD measurements allowed us to recognize the positive PD in these phase regions as the streamer-type PD with electron avalanche. On the other hand, PD light emission image at around PD inception phase for f = 400 Hz was film-like, where the pulse-like PD current waveforms were not detected as was shown in Fig. 2.13 (d). This means that the positive PD at around the PD inception phase for f = 400 Hz can be identified as the glow-type PD.

Figure 2.16 shows the PD extension length under ac and positive dc conditions as a function of instantaneous voltage, which is derived from Table 2.4 as the longest length of PD light emission in the direction of the electrode axis. In Fig. 2.16, ℓ_{cr} designates the critical distance from the needle tip, where the critical electric field of SF_6 gas (87.8 V/(m·Pa))[6] is satisfied. PD extension length increases with the increase in the instantaneous voltage at both (a) increasing part (voltage phase: 0° ~ 90°) and (b) decreasing part (voltage phase: 90° ~ 180°) in the positive half cycle under ac condition. The slope of PD extension length against the instantaneous voltage was identical under both ac and positive dc conditions. Furthermore, the PD extension length

Table 2.4 Light emission images of positive PD under ac conditions.
(g = 20 mm, r = 500 μm, V_a = 30 kV_{rms}, in SF_6 gas, P = 0.1MPa, superimposed for 60 cycles.)

	ac voltage phase			
	Around PD inception		Peak	Around PD extinction
60 Hz				
400 Hz	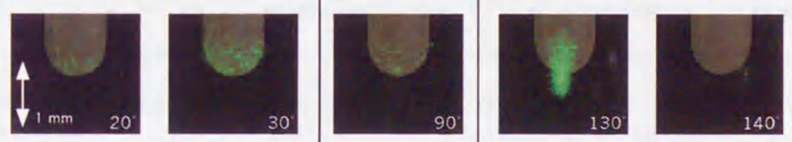			

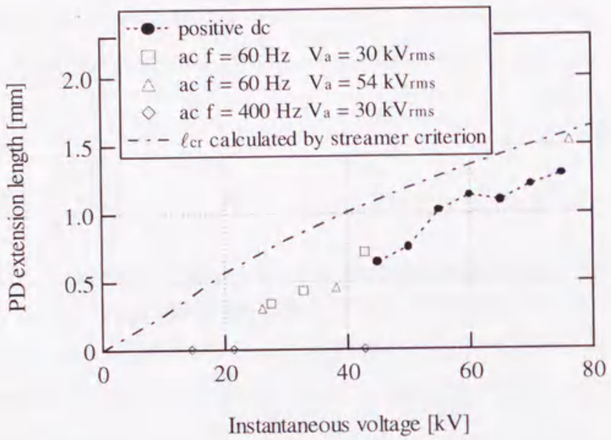

(a) Voltage phase 0° ~ 90°.

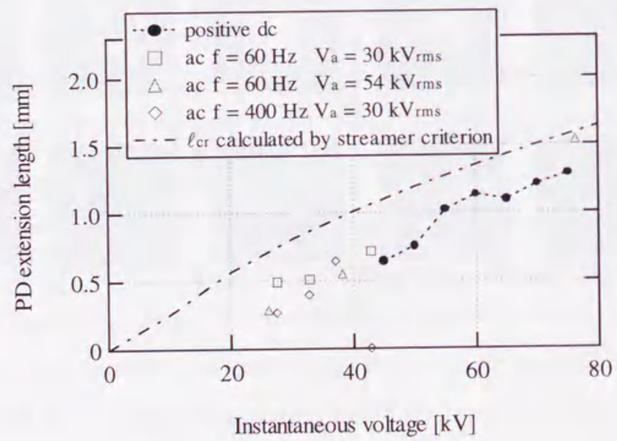

(b) Voltage phase 90° ~ 180°.

Fig. 2.16 Instantaneous voltage dependence of extension length of positive PD. (g = 20 mm, r = 500 μm, in SF_6 gas, P = 0.1 MPa.)

was always shorter than ℓ_{cr}, which also confirms that the brush-like PD corresponds to the streamer-type PD. These results suggest that PD characteristics and their mechanisms at streamer region in SF_6 gas would be irrespective of applied voltage waveforms, but determined by the instantaneous voltage.

2.7 Space Charge Behavior and Positive Partial Discharge Generation Mechanism

The positive PD characteristics under low frequency / large radius of needle tip / short gap conditions, which corresponds to the case in Fig. 2.12, showed that PD with large magnitude of current pulse height at around positive PD inception phase occurred. On the other hand, those under high frequency / small radius of needle tip / long gap conditions which correspond to the cases in Figs. 2.13 (a), (b), (c) and (d), respectively, showed that PD with only small magnitude of current pulse height at around positive PD inception phase occurred. These differences in the positive PD characteristics for different electrode and power frequency conditions allow us to expect the contribution of space charge behavior to positive PD generation mechanism in SF_6 gas. Figure 2.17 schematically shows positive PD generation mechanism under ac condition for (a) low frequency / large radius of needle tip / short gap conditions, and (b) high frequency / small radius of needle tip / long gap conditions.

2.7.1 Low Frequency / Large Radius of Needle Tip / Short Gap Conditions

In Fig. 2.17 (a), relationship between space charge behavior and PD generation mechanism can be explained as follows, which corresponds to the case in Fig. 2.12;

(i) Low frequency:

Time interval from the preceding negative PD extinction to the voltage polarity reversal

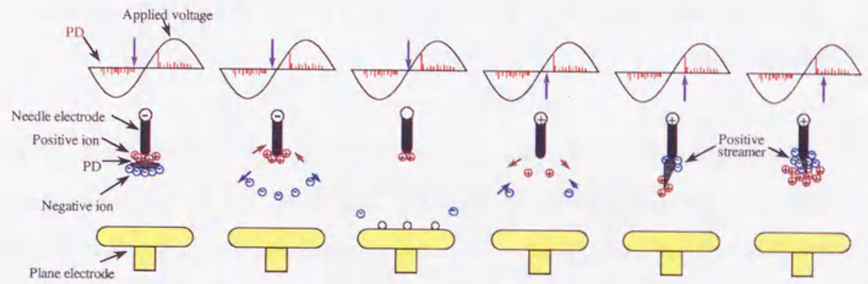

(a) Low frequency / large radius of needle tip / short gap conditions.

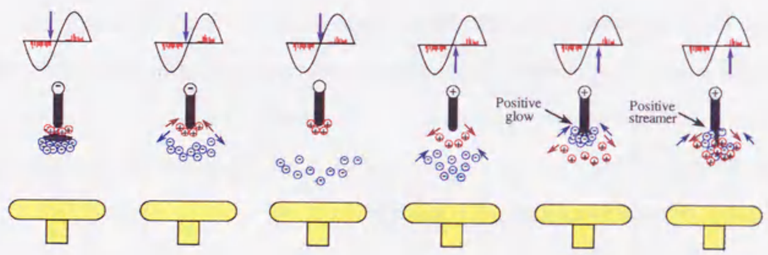

(b) High frequency / small radius of needle tip / long gap conditions.

Fig. 2.17 Schematic illustrations of positive PD generation mechanism under ac condition.

to the positive polarity is longer than that in the case of high frequency condition. Thus, negative ions generated by negative PD can drift long distance until the polarity reversal.

(ii) Large radius of needle tip:

Electric field distribution in the vicinity of the needle tip is less inhomogeneous, compared with that in the small tip radius electrode. Thus, negative ions generated by negative PD can be driven away from the needle tip by relatively large electrostatic force.

(iii) Short gap length:

When the gap length is short, negative ions generated by negative PD can more easily reach the plane electrode.

In the above cases, the positive and negative ions generated by PD in the preceding negative half cycle can easily reach both the needle and the plane electrodes, respectively, and be neutralized. Thus, in the subsequently coming positive half cycle, the residual ion density in the gap space becomes low, which reduces not only the corona stabilization effect by positive ions at around the needle tip, but also the generation probability of initial electrons for PD inception. When an initial electron is occasionally created in the highly stressed volume, a streamer-type PD with a large magnitude of current pulse height can be induced with less effective corona stabilization effect.

2.7.2 High Frequency / Small Radius of Needle Tip / Long Gap Conditions

In Fig. 2.17 (b), the opposite process of space charge behavior to that discussed in Fig. 2.17 (a) should be promoted, which corresponds to the cases in Figs. 2.13 (a), (b), (c) and (d). Then, the higher density of positive and negative ions generated by the preceding negative PD can remain in the gap space even at the polarity reversal of the applied ac voltage. In the subsequently coming positive half cycle, the generation probability of initial electrons is increased, and a film-like cloud of positive ions can cover the needle tip. Then, the electric field strength outside the positive ion cloud can be reduced due to the activated corona stabilization effect. In

this case, the electric field strength between the needle tip and the film-like ion cloud can be enhanced with the homogeneous electric field distribution, which induces the stable Hermstein glow discharge with quite small PD extension length [7]. Then, streamer-type PD with a small magnitude of PD current pulse height or glow-type PD with film-like light emission can be induced, depending on the surrounding conditions.

2.7.3 Post Partial Discharge Inception / Positive dc Voltage Conditions

After the first PD in the positive half cycle once occurs, the density of positive and negative ions in the gap space is further increased. Then, the corona stabilization and the generation of initial electrons can be highly activated. Therefore, only PD with a small magnitude of PD current pulse height can follow as shown in Figs. 2.12 and 2.13. In the case at g = 20 mm, r = 500 μm, f = 60 Hz in Fig. 2.13 (c), PD with large current pulse height occurred at around 70°, which could be cosidered not as PD inception phase. This is due to the fluctuation of the PD inception phase in each cycle; in case the amount of the residual negative ions at the polarity reversal is so small, the positive PD with large current pulse height occurs at the latter PD inception phase in the subsequently coming positive polarity, which corresponds to the process mentioned in Subsection 2.7.1. In case the amount of the residual negative ions at the polarity reversal is large, the positive PD with only a small current pulse height occurs at the early PD inception phase in the subsequent coming positive polarity, which corresponds to the process mentioned in Subsection 2.7.2.

Such a PD generation mechanism should also be applied to that for positive dc condition, where plenty of PD are generated under a continuous high voltage, e.g. $V_a \geq 40$ kV in Fig. 2.15. Therefore, post PD characteristics except at around the PD inception region can be regardless of ac or dc condition as shown in Figs. 2.12 and 2.13.

2.8 Ion Drift Simulation

In order to quantitatively verify the existence of the larger residual ions in the gap space for higher frequency, smaller tip radius and longer gap, the negative ion drift was calculated for two situations; for the PD inception measured by first pulse detection as shown in Figs. 2.8 and 2.9, and for the PD inception at the PD inception phase for higher voltage application, i.e., at V_a = 30 kV_{rms} as shown in Figs. 2.12 and 2.13. The calculations were carried out with the following assumptions;

(1) The negative ion mobility was considered to be 0.65×10^{-4} $m^2/(V\cdot sec)$[8].

(2) Collisions between the negative ion and the other particles were neglected.

(3) The electric field formed by space charges was neglected.

(4) The static electric field distribution in the gap space was calculated by the electric image method.

(5) The ion was initially located at 0.3 mm below the needle tip, where the extension length of negative PD got the maximum.

Moreover, the ion position was calculated in every 0.001° phase step. Figure 2.18 shows the flow chart of the calculation.

Firstly the negative ion trajectories were calculated for just above the negative PD inception voltage for f = 60 and 400 Hz with the electrode configurations of g = 10 mm and r = 500 μm, in order to verify the applied frequency dependence on the PD inception voltage as shown in Fig. 2.8 and 2.9. For the calculation, the initial condition was set as follows; (a) the negative ion was generated at 270° of the applied voltage phase. (b) The applied voltage was set at 12.7 kV_{rms} as just above PDIV- for both f = 60 Hz and f = 400 Hz.

Figure 2.19 shows the trajectories of the negative ion drift along the gap axis calculated for g = 10 mm, r = 500 μm, f = 60 Hz and f = 400 Hz as functions of (a) voltage phase and (b) time after the ion generation. In Fig. 2.19, the time when the negative PD was generated (270°) and that when the applied voltage polarity was reversed from negative to positive for f = 60 Hz

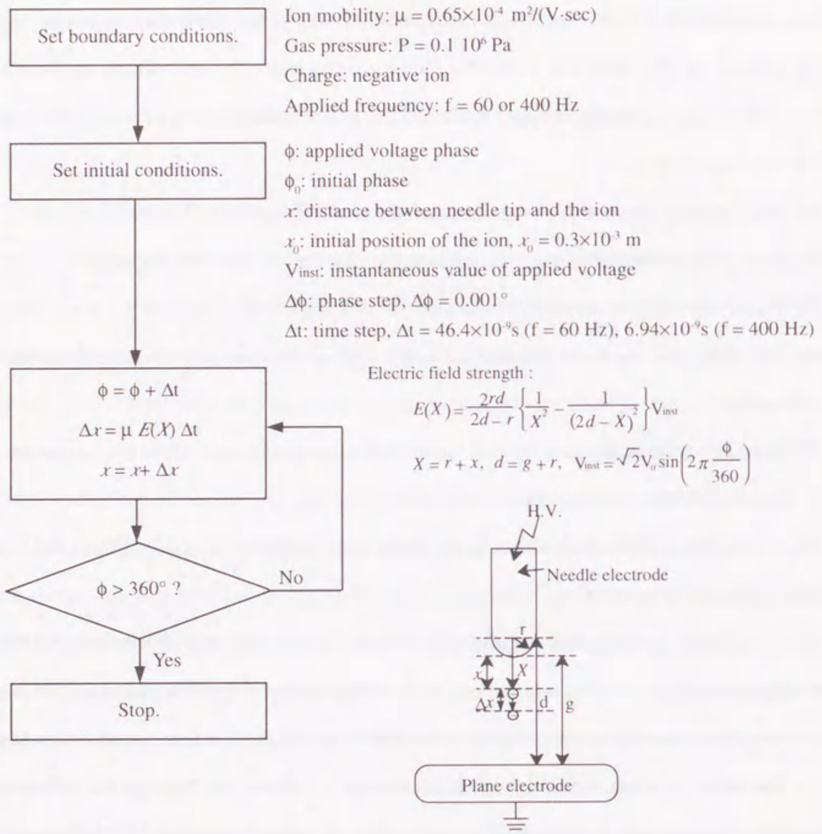

Fig. 2.18 Flow chart of the ion drift calculation.

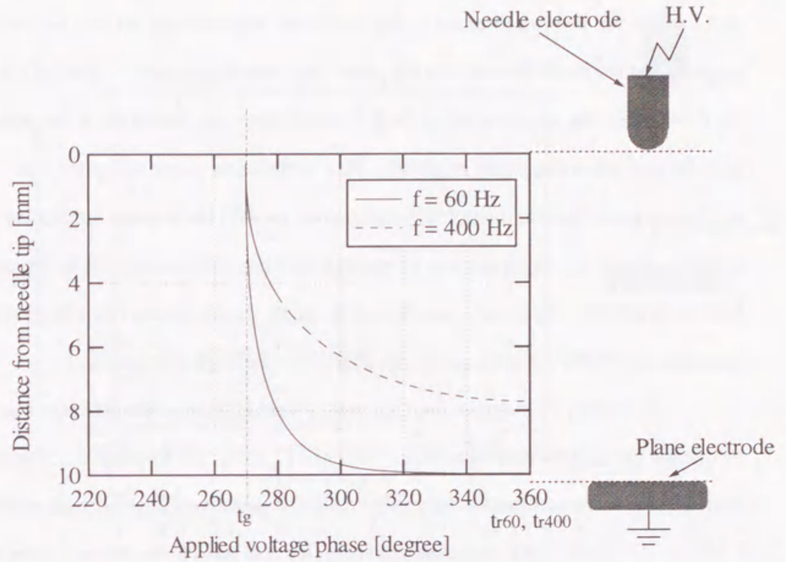

(a) Voltage phase characteristics.

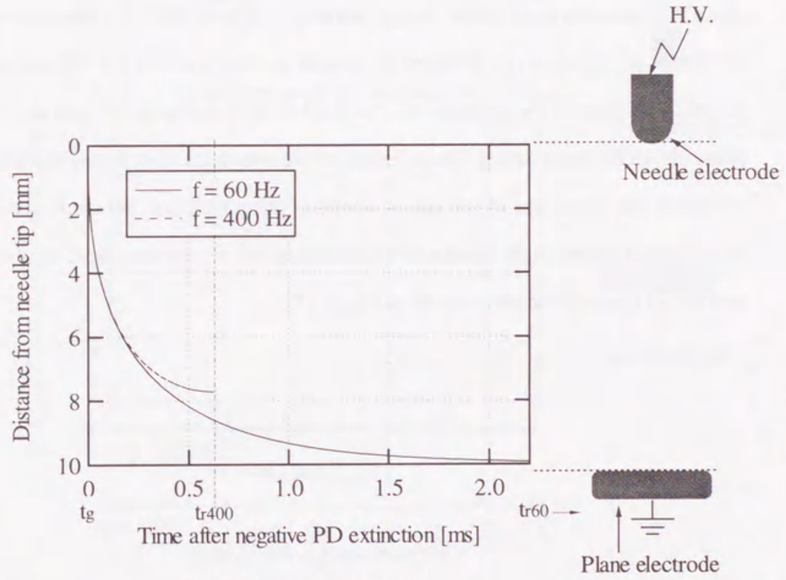

(b) Time characteristics.

Fig. 2.19 Calculation of trajectories of the negative ion drift.
(in SF_6 gas, P = 0.1 MPa, V_a = 12.7 kV_{rms}.)

and f = 400 Hz were defined as t_g, t_{r60} and t_{r400}, respectively. As can be seen in Fig. 2.19, the negative ion for f = 60 Hz reached the plane electrode at the polarity reversal t_{r60}. On the contrary, for f = 400 Hz, the negative ion drifted 7.7 mm below the needle tip at the polarity reversal t_{r400} and did not reach the plane electrode. This simulation result suggests that the amount of the residual negative ions at the polarity reversal for f = 400 Hz is much larger than that for f = 60 Hz at PDIV-. Thus, the larger amount of residual negative ions could exist in the subsequent positive half cycle at higher frequency, which would supply the initial electrons for positive PD inception and resultant PDIV+ decreases toward PDIV- for the higher frequency.

Secondly, the negative ion trajectories were calculated for different electrode and applied frequency conditions corresponding to Figs. 2.12 and 2.13. In these calculations, negative ions such as SF_6^- were assumed to be generated at the negative PD extinction phase (325°). Figures 2.20 (a) ~ (d) shows the simulation results for different conditions. In Fig. 2.20 (a) under g = 10 mm, r = 500 μm and f = 60 Hz, corresponding to the case of Fig. 2.12, the negative ions could almost reach the plane electrode at the voltage polarity reversal (360°). On the other hand, in the cases of (b) higher frequency (f = 400 Hz), (c) smaller needle tip radius (r = 200 μm) and (d) longer gap length (g = 20 mm), the negative ions stopped drifting at 4 mm, 1.8 mm and 8.3 mm above the plane electrode, respectively. Those negative ions which could not reach the plane electrode will remain in the gap space in the subsequently coming positive half cycle and contribute to the activation of corona stabilization effect at around the needle electrode, as was described in the positive PD generation mechanism in Fig. 2.17.

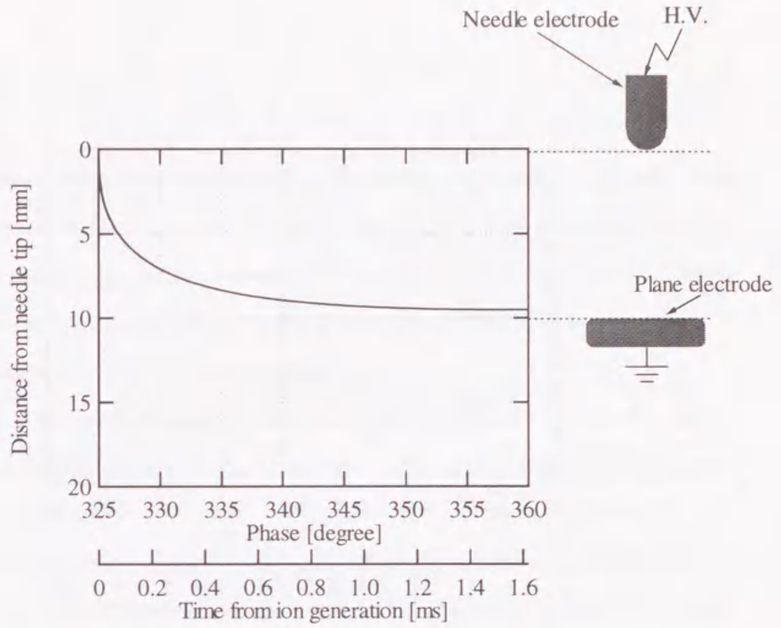

(a) g = 10 mm, r = 500 μm, f = 60 Hz.

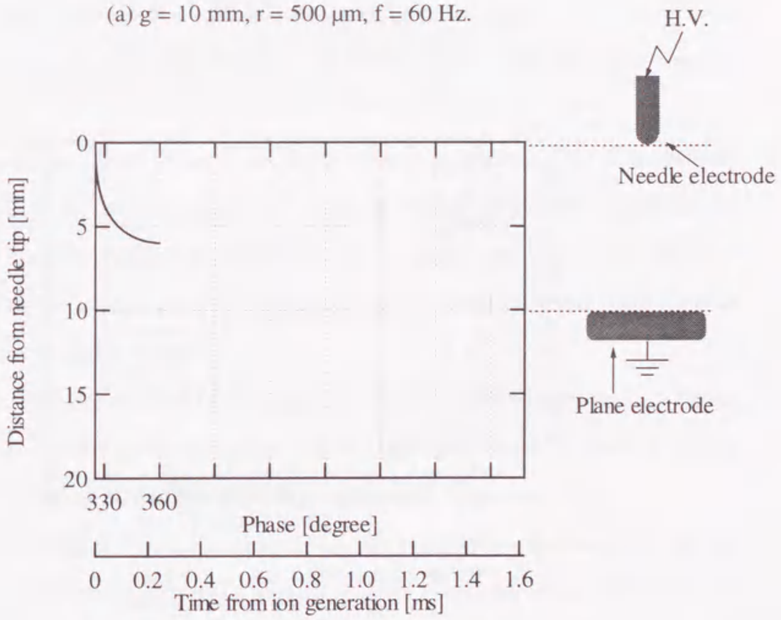

(b) g = 10 mm, r = 500 μm, f = 400 Hz.

Fig. 2.20 Calculation of trajectories of the negative ion drift.
(in SF_6 gas, P = 0.1 MPa, V_a = 30 kV_{rms}.)

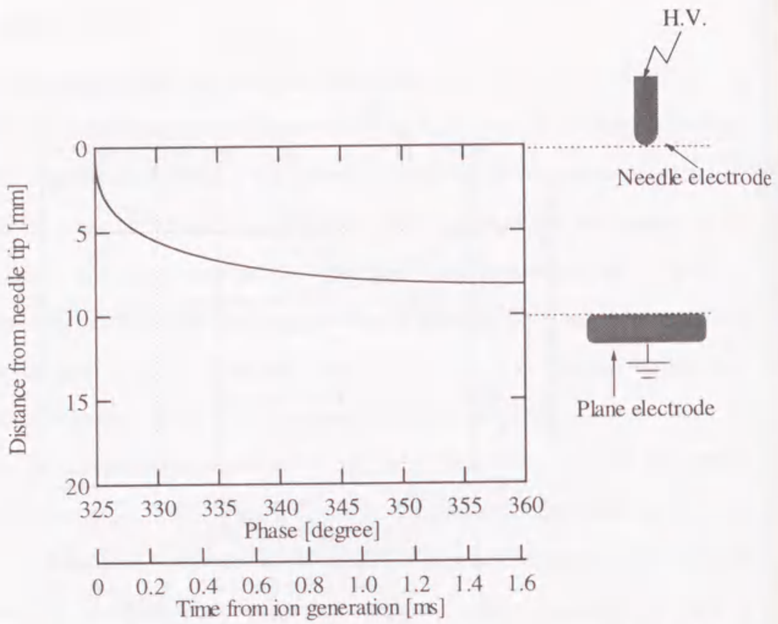

(c) g = 10 mm, r = 200 μm, f = 60 Hz.

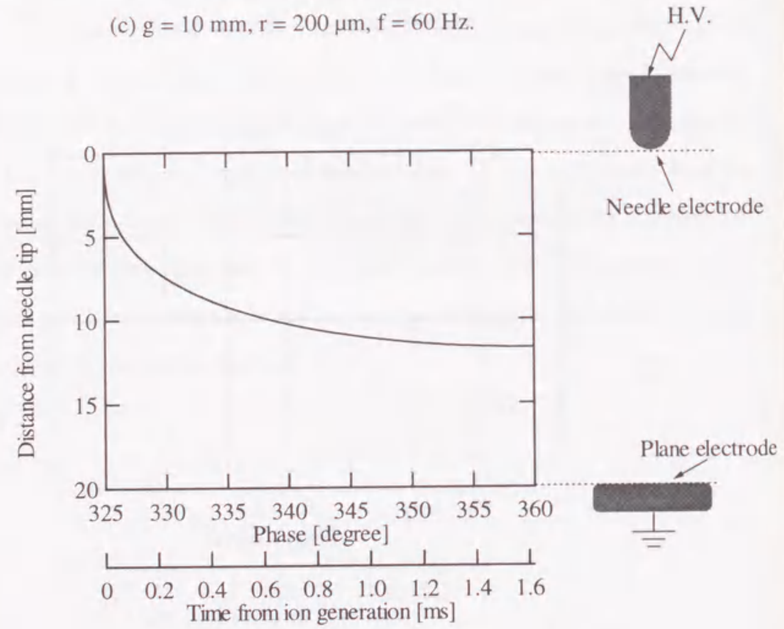

(d) g = 20 mm, r = 500 μm, f = 60 Hz.

Fig. 2.20 Calculation of trajectories of the negative ion drift.
(in SF_6 gas, P = 0.1 MPa, V_a = 30 kV_{rms}.) continued.

2.9 Conclusions

In this chapter, the measuring systems for PD current pulse waveform with wide band frequency response and for PD light emission images with large expansion rate were established. Then, the effect of space charge behavior on the PD characteristics in SF_6 gas under ac voltage application was investigated under different power frequencies and electrode configurations.

Consequently, the followings were clarified:

(1) Positive PD inception voltage decreased with the increase of the frequency and finally reached the level of negative PD inception voltage, while negative PD inception voltage was irrespective of the power frequency.

(2) Under low frequency / large radius of needle tip / short gap conditions, streamer-type PD with a large magnitude of current pulse height occurred at around positive PD inception phase. This is due to the reduced corona stabilization effect and generation probability of initial electrons, because most of space charges could be swept out in the preceding negative half cycle.

(3) Under high frequency / small radius of needle tip / long gap conditions, PD with relatively small magnitude of current pulse height was induced at around positive PD inception phase. The glow-type PD with film-like light emission images having no pulse-like current waveforms was observed in some of these cases. This is because the corona stabilization effect could be activated by residual space charges.

(4) PD with only a small magnitude of PD current pulse height occurred with the highly activated corona stabilization effect, in the cases of post PD inception phase under ac condition as well as positive dc condition, where lots of PD were continuously generated.

Finally, a sequential model of positive PD in SF_6 at streamer region under ac voltage condition was proposed taking account of sequential space charge behavior. The model was verified by the calculation of the trajectories of the space charge for several conditions.

References

[1] O.Farish, O.E.Ibrahim and A.Kurimoto: "Prebreakdown Corona Process in SF_6 and SF_6/N_2 Mixtures", *3rd International Symposium on High Voltage Engineering*, No. 31.15, 1979.

[2] R.Baumgartner, B.Fruth, W.Lanz and K.Pettersson: "Partial Discharge - Part IX: PD in Gas-insulated Substations - Fundamental Considerations", *IEEE Electrical Insulation Magazine*, Vol. 7, No. 6, pp. 5-13, 1992.

[3] L.Niemeyer, B.Fruth and H.Kugel: "Phase Resolved Partial Discharge Measurements in Particle Contaminated SF_6 Insulation", *Gaseous Dielectrics VI*, pp. 579-585, Plenum Press, New York, 1991.

[4] W.Hauschild, J.Spiegelberg and E.Lemke: "Frequency-tuned Resonant Test Systems for High Voltage On-site Testing of SF_6-insulated Apparatus", *10th International Symposium on High Voltage Engineering*, Vol. 4, pp. 457-460, 1997.

[5] F.Pinnekamp and L.Niemeyer: "Qualitative Model of Breakdown in SF_6 in Inhomogeneous Gaps", *Journal of Physics D: Applied Physics*, Vol. 16, pp. 1293-1312, 1983.

[6] M.S.Bhalla and J.D.Craggs: "Measurement of Ionization and Attachment Coefficients on Sulphur Hexafluoride in Uniform Fields", *Proceedings of Physical Society*, Vol. 80, pp. 151-160, 1962.

[7] W.Hermstein: "Die Stromfaden-entladung und ihr Übergang in das Glimmen", *Archiv für Elektrotechnik*, Vol. 45, No. 3, pp. 209-224, 1960.

[8] J.de Urquijo-Carmona, I.Albarez, H.Martinez and C.Cisneros: "Mobility and Longitudinal Diffusion of SF_5^- and SF_6^- in SF_6", *Journal of Physics D: Applied Physics*, Vol. 24, No. 5, pp. 664-667, 1991.

Chapter 3 Sequential Generation Characteristics of Partial Discharges in SF_6 Gas with Consideration of Space Charge Behavior and Corona Stabilization

3.1 Introduction

A leader-type PD is well-known to induce breakdown easily. Some investigations have been carried out for the leader-type PD under steep-front pulse voltage condition so far[1-3], due to the space charge free environment. However, great number of PD would occur in gas insulated electric power apparatus under operation with ac and dc voltage conditions, which generate huge amount of positive and negative space charges in the vicinity of the PD source. The space charges bring much influence to the following PD, because of the distortion of the electric field distribution and the increase in the generation probability of initial electrons. Therefore, it is important to clarify the sequential generation characteristics of PD for the breakdown prediction in the actual power apparatus and the discussion of the space charge behavior. Though some investigations focused on the sequential PD characteristics were carried out so far[4-6], almost all of them dealt with PD in air or in void of solid dielectrics[4, 5].

In this chapter, firstly a measurement system with high time-resolution is constructed for sequential PD characteristics in SF_6 gas. Secondly, the sequential PD characteristics for ac and dc voltage conditions are measured in order to estimate the relationship between the magnitude of PD charge q and its preceding time Δt. Finally, the sequential PD characteristics are discussed taking consideration of the space charge behavior and its influence to the corona stabilization effect by schematic models and numerical calculations of ion diffusion and drift.

3.2 Experimental Setup for Sequential Partial Discharge Generation Characteristics

Figure 3.1 shows an experimental setup for the measurement of sequential PD generation characteristics. The model GIS, the high voltage sources and the matching circuit were the same as those introduced in Section 2.2. As a PD source, a needle electrode (made of stainless-steel, tip radius r = 500 μm, length ℓ = 20 mm) was set on the high voltage conductor of the model GIS. Positive dc or ac high voltage was applied to the model GIS in order to generate PD at the needle tip. A needle-plane electrode system with the gap length of 10 mm was built in the model GIS. The model GIS was filled with SF_6 gas at pressure P = 0.1 MPa in order to discuss PD characteristics at the region of streamer-type discharge[7] and their mechanism in SF_6 gas.

PD signals were observed by a digital oscilloscope (LeCroy 9374M, sampling rate: 1 GS/s, analog band width: 1 GHz, acquisition length: 1 Mpoints) through the matching impedance mentioned in Section 2.2 and an integrator to estimate charge magnitude of a single PD. The integrator was consisted by a high-speed operational amplifier so that it had a short time constant of 33 ns and an output impedance of 50 Ω to achieve high time-resolution. The highest sensitivity of PD charge detection was 1.8 pC.

In order to determine the integration constant for the integrator, pulse signals with the rise time of several ns and the pulse height of several 100 mV were inputted into the integrator. Figure 3.2 shows the example of a pair of the input and output signals of the integrator. In Fig. 3.2, the input signal had a rise time of 1.1 ns, a fall time of 8 ns and the pulse height of 250 mV, which corresponded to a signal of 25 pC. The amplitude of the output signal was 91.6 mV. The same measurements were carried out for different input pulses. As a result, the integration constant was determined as 274 pC/V.

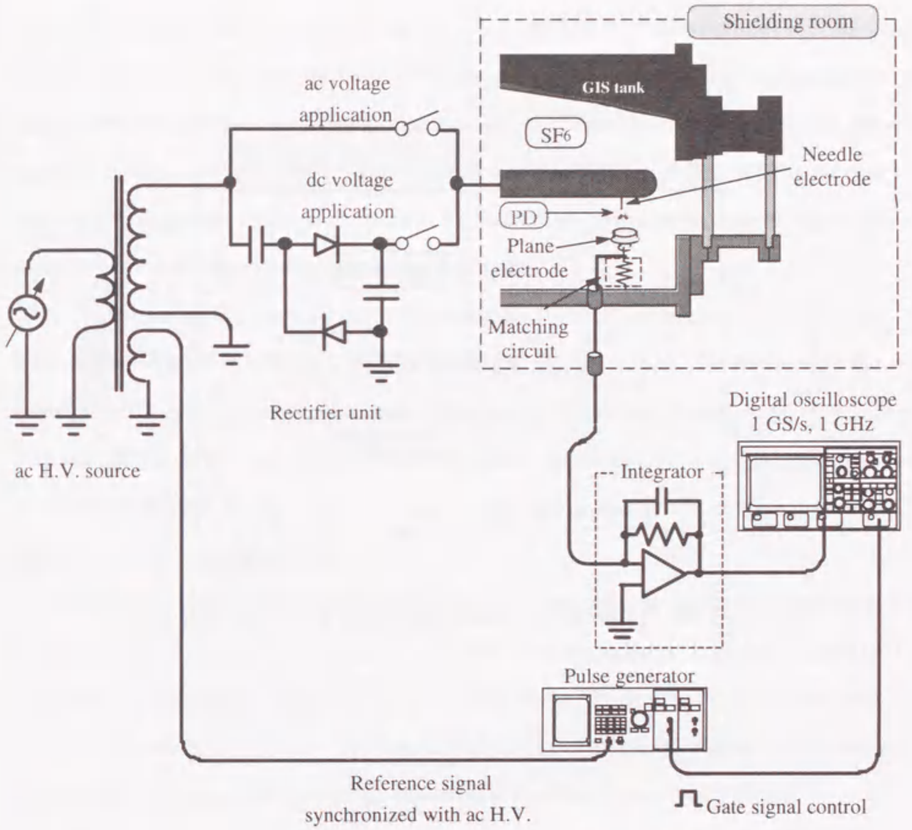

Fig. 3.1 Experimental setup for measuring sequential generation characteristics of PD pulses.

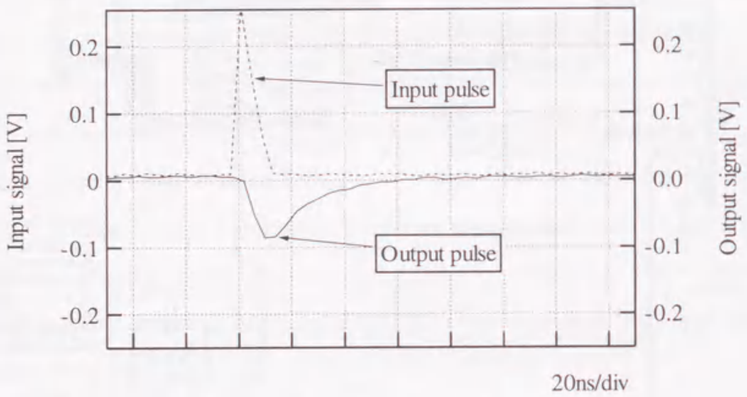

Fig. 3.2 A pair of typical input and output signal waveforms of integrator.

3.3 Sequential Generation Characteristics of Partial Discharge for ac Voltage Condition

Figure 3.3 shows the typical time-resolved PD characteristics under ac condition with frequency f = 60 Hz at (a) applied voltage V_a = 20 kV_{rms} and (b) V_a = 30 kV_{rms} for a single power frequency cycle. In Fig. 3.3, the solid vertical lines show the individual PD pulse and the broken curve shows the applied voltage. As seen in Fig. 3.3 (a), the first PD with relatively large magnitude of charge occurred at 44° and was followed by plenty of subsequent PD with small magnitude of charge at V_a = 20 kV_{rms}. The sequential generation of the first PD and the subsequent PD was repeated in the same half cycle. On the other hand, at V_a = 30 kV_{rms} in Fig. 3.3 (b), the first PD had a larger magnitude of charge than that at V_a = 20 kV_{rms} and the subsequent PD with a higher repetition rate were observed in the positive half cycle.

The sequential PD characteristics were measured 10 times for each condition. The resultant relationship between PD charge q and instantaneous applied voltage V_{inst} for the first PD and subsequent PD in the positive half cycle is shown in Fig. 3.4. As can be seen in Fig. 3.4, though V_{inst} scattered from 19.5 to 24 kV, the charge magnitude of the first PD was proportional to V_{inst} at the PD generation, irrespective of V_a. In contrast, charge magnitude of subsequent PD was small and independent of V_{inst} and V_a.

Figure 3.5 shows the relationship between the time interval Δt between sequential PD pulses and V_{inst} at (a) V_a = 20 kV_{rms} and (b) V_a = 30 kV_{rms}, respectively. Note that V_{inst} in Fig. 3.5 shows the instantaneous voltage at the second PD of the two sequential PD pulses, thus, Δt means the preceding time. At V_a = 20 kV_{rms} in Fig. 3.5 (a), Δt decreased slightly with the increase of V_{inst}. The reduction of Δt was clearly observed at V_a = 30 kV_{rms} in Fig. 3.5 (b).

The instantaneous voltage dependence on the charge magnitude of the first PD in Fig. 3.4 can be explained with the space charge behavior mentioned in Section 2.7, as follows; ions generated by PD in the negative half cycle reach both needle and plane electrode surfaces and most of them are neutralized at the polarity reversal of applied ac voltage with the power frequency f = 60 Hz. The residual ions contribute to the positive PD generation in the subsequent positive

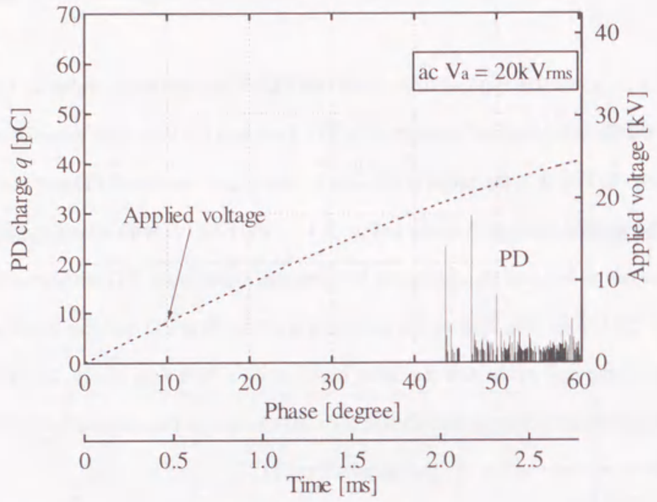

(a) Va = 20 kVrms.

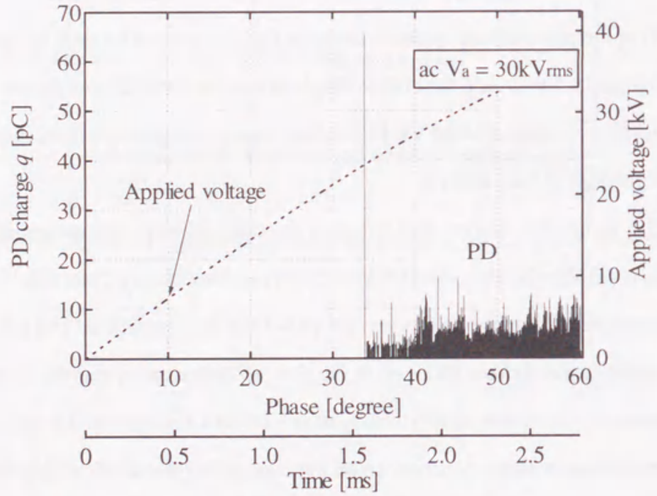

(b) Va = 30 kVrms.

Fig. 3.3 Sequential PD generation characteristics at around positive PD inception phase under ac voltage condition.
(g = 10 mm, r = 500 μm, in SF6 gas, P = 0.1 MPa.)

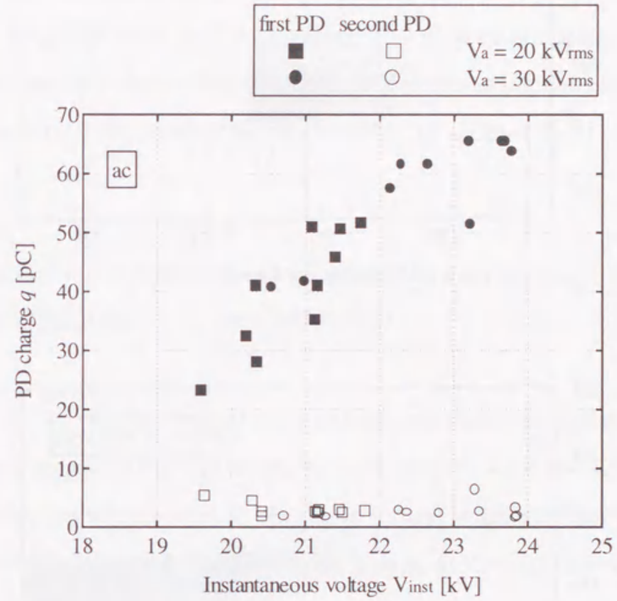

Fig. 3.4 Relationship between PD charge and instantaneous voltage for first and second PD in the positive half cycle.
(g = 10 mm, r = 500 μm, in SF6 gas, P = 0.1 MPa.)

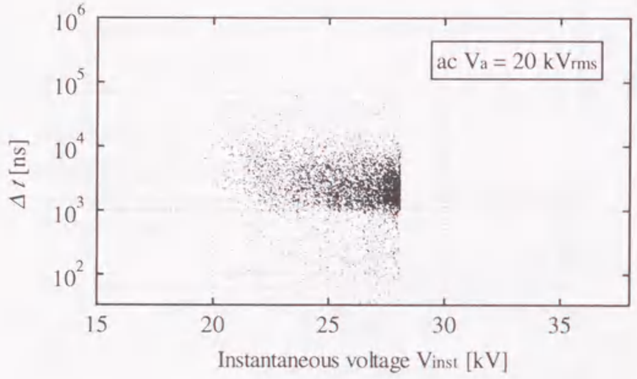

(a) V_a = 20 kV_{rms}.

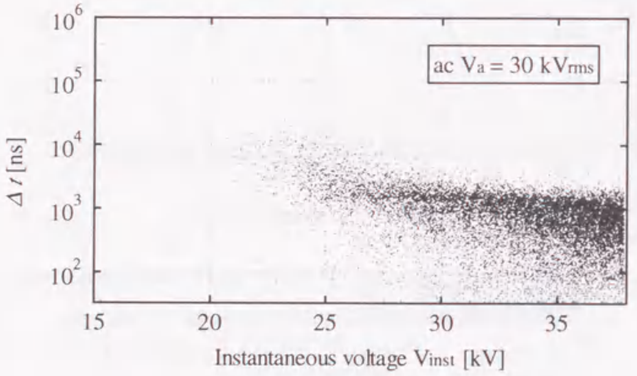

(b) V_a = 30 kV_{rms}.

Fig. 3.5 Relationship between time interval Δt of sequential PD pulses and instantaneous voltage under ac condition.
(g = 10 mm, r = 500 μm, in SF_6 gas, P = 0.1 MPa.)

half cycle. The charge magnitude of the first PD would be proportional to the size of the critical volume, namely the instantaneous voltage. The scattering of V_{inst} is related to the generation probability of an initial electron. On the contrary, PD subsequent to the first PD had small magnitude of charge. This is because the first PD generates large amount of positive ions at around the needle tip, which reduce the electric field strength at the needle tip and activate corona stabilization effect. Therefore, the ionization by PD is restrained and PD with small magnitude of charge only occur. Here, the increase of V_{inst} raises the probability of PD generation due to the enhancement of electric field strength at the needle tip and the concentration of negative ions at the needle tip. Thus, Δt would be reduced in Fig. 3.5 at higher V_{inst}.

3.4 Sequential Generation Characteristics of Partial Discharge for Positive dc Voltage Condition

Figures 3.6 (a) ~ (d) show typical sequential PD generation characteristics under positive dc voltage application at (a) V_a = +25 kV, (b) V_a = +30 kV, (c) V_a = +35 kV and (d) V_a = +40 kV, respectively. Note that PD inception and breakdown voltages in this condition were +23 kV and +54 kV, respectively, at the positive dc voltage application. At V_a = +25 kV in Fig. 3.6 (a), a PD with large magnitude of charge was generated and was followed by several PD with small magnitude of charge. After a certain time interval without PD generation, a PD with relatively large magnitude of charge was generated again. At V_a = +30 kV in Fig. 3.6 (b), the magnitude of individual PD charge decreased and the repetition rate of PD pulses increased. The repetition rate of PD pulses increased more at V_a = +35 kV in Fig. 3.6 (c) and at V_a = +40 kV in Fig. 3.6 (d).

Figure 3.7 shows the applied voltage dependence of the time interval Δt between subsequent PD pulses. Note that Δt is the reciprocal of the repetition rate, and that the vertical range lines show the min / max values of the obtained data. In Fig. 3.7, Δt gradually decreased with the increase in the applied voltage, which also corresponded to the result under ac condition in Figs.

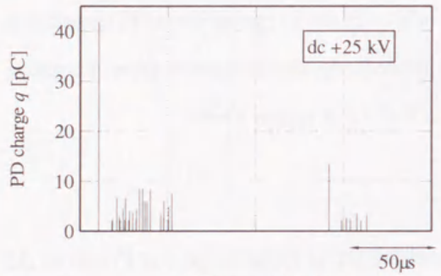

(a) V_a = +25 kV.

(b) V_a = +30 kV.

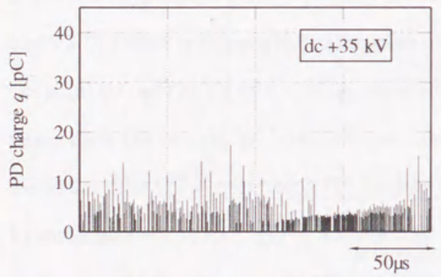

(c) V_a = +35 kV.

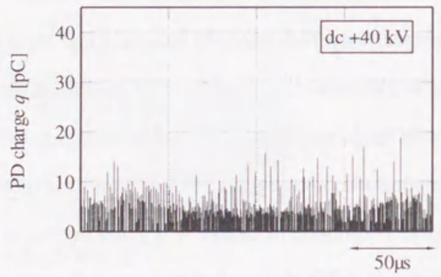

(d) V_a = +40 kV.

Fig. 3.6 Sequential PD generation characteristics under positive dc voltage condition. (g = 10 mm, r = 500 m, in SF_6 gas, P = 0.1 MPa.)

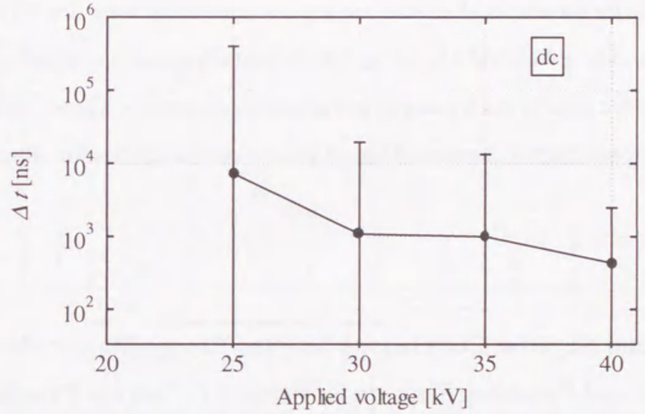

Fig. 3.7 Applied voltage dependence of time interval Δt of sequential PD pulses under positive dc condition.

3.5 (a) and (b).

In order to discuss PD mechanism from the PD generation sequence, the PD charge magnitude q_n and the time interval Δt_n of sequential PD pulses are defined as shown in Fig. 3.8, where n is the sequential number of PD pulses. This means that PD(q_n) occurs with time interval Δt_n after the previous PD(q_{n-1}) generation. Figures 3.9 (a) ~ (d) show the relationship between q_n and Δt_n for (a) V_a = +25 kV, (b) V_a = +30 kV, (c) V_a = +35 kV and (d) V_a = +40 kV, respectively. Each plot corresponds to a pair of sequential PD pulses during 2 ms. At V_a = +25 kV in Fig. 3.9 (a), q and Δt were in the positive correlation at $\Delta t > 1$ μs and in the negative correlation at $\Delta t < 1$ μs. The similar characteristics could also be seen at V_a = +30 kV in Fig. 3.9 (b) and at V_a = +35 kV in Fig. 3.9 (c), where the boundaries of positive and negative correlations were Δt = 250 and 150 ns, respectively. However, at V_a = +40 kV in Fig. 3.9 (d), neither positive nor negative correlation could be recognized clearly. Such positive and negative correlations will be explained with consideration of space charge behavior and time-depended corona stabilization effect in the next section.

3.5 Positive and Negative Correlations between Charge Magnitude of Partial Discharge and Preceding Time under Positive dc Voltage Condition

Figure 3.10 shows the schematic illustration of the space charge behavior associated with positive PD generation. At first, PD(q_{n-1}) generates positive ions around the PD channel, as shown in Fig. 3.10 (I). Next, just after the generation of PD(q_{n-1}), the electric field strength at around the needle tip would not be relaxed, because remaining positive ions could not diffuse in the radial direction of needle electrode, but longitudinally distribute along the past PD channel, as shown in Fig. 3.10 (II). Thus, the corona stabilization effect is not enough activated at this moment. PD(q_n) would be generated (Fig. 3.10 (II-a)), if an initial electron due to the photo detachment or collisional detachment of the negative ions is created in a limited volume

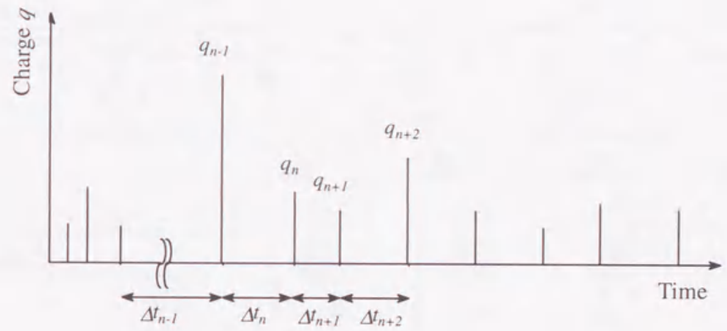

Fig. 3.8 Definition of PD charge q and time interval Δt of sequential PD pulses.

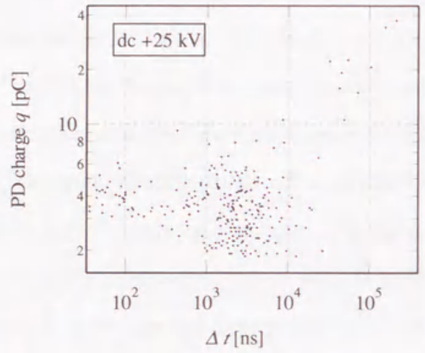

(a) V_a = +25 kV.

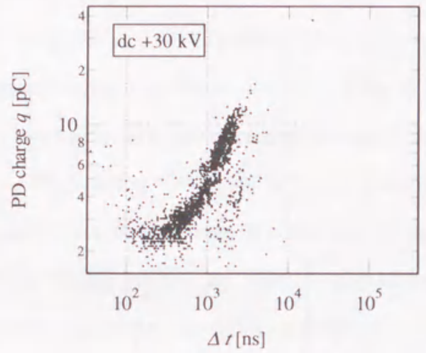

(b) V_a = +30 kV.

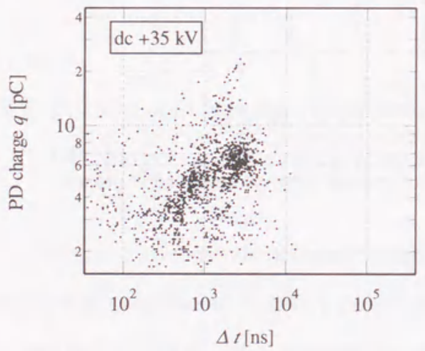

(c) V_a = +35 kV.

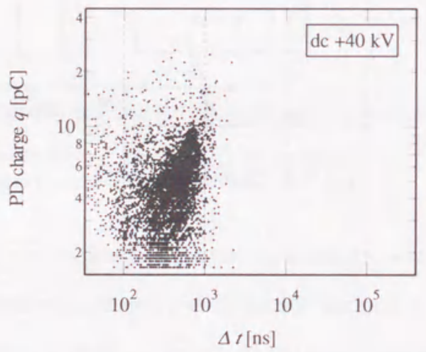

(d) V_a = +40 kV.

Fig. 3.9 Relationship between PD charge q and time interval Δt of sequential PD pulses under positive dc voltage condition.
(g = 10 mm, r = 500 μm, in SF_6 gas, P = 0.1 MPa.)

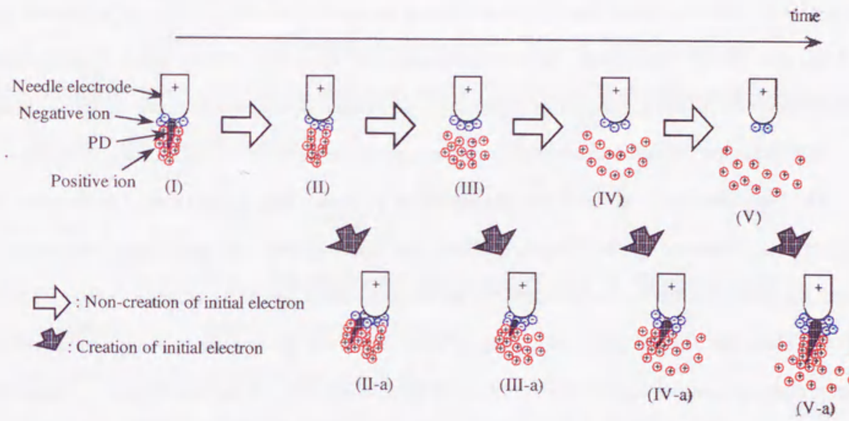

Fig. 3.10 Schematic illustration of space charge behavior and PD generation.

(hereinafter, critical volume) where the electric field strength is larger than the critical strength of SF_6 (87.8 V/(m·Pa))[8]. The PD(q_n) has relatively large magnitude of charge, because the corona stabilization effect has not been activated enough to suppress the generation and extension of PD(q_n), as described above. Therefore, at very small Δt region such as at the stages of (II) and (II-a) in Fig. 3.10, the charge magnitude of PD(q_n) becomes relatively large.

As the time goes on from the previous PD(q_{n-1}) generation, the positive ions generated by the PD(q_{n-1}) diffuse in the radial direction of the symmetrical axis of the needle - plane electrode system, and then the corona stabilization effect becomes active, as shown in Fig. 3.10 (III). At this moment, when an initial electron is created in the critical volume, PD(q_n) is generated (Fig. 3.10 (III-a)). The PD(q_n) would have small magnitude of charge due to the activated corona stabilization effect. Then, the charge magnitude of PD(q_n) decreases with the increase in Δt at the small Δt region, which corresponds to the negative correlation of q - Δt characteristics.

On the other hand, at the larger Δt region of μs order after the PD(q_{n-1}) generation, the positive ions generated by the PD(q_{n-1}) diffuse and drift into the gap space from the needle tip toward the plane electrode, and the corona stabilization effect would be relaxed in Fig. 3.10 (IV) and (V). Thus, the electric field strength at around the needle tip becomes strong and the critical volume expands. An initial electron created at the critical volume in this situation triggers the PD(q_n) with large charge magnitude (Fig. 3.10 (IV-a) and (V-a)). Then, the charge magnitude of PD(q_n) increases with the increase in Δt at the large Δt region, which corresponds to the positive correlation of q - Δt characteristics. The selection of the process described in Fig. 3.10 (II-a), (III-a), (IV-a) and (V-a) depends on the probability of initial electron generation.

3.6 Calculation of Ion Diffusion and Drift

For the quantitative understanding of the space charge behavior in Fig. 3.10, the space charge behavior is theoretically calculated with consideration of (a) ion diffusion and (b) ion drift, respectively, after PD generation.

3.6.1 Ion Diffusion

The positive ion distribution was calculated with consideration of ion diffusion in the radial direction of needle electrode. The ion diffusion coefficient is given by Eq. (3.1).

$$\text{Ion diffusion coefficient} \quad D = \mu \frac{kT}{e} \tag{3.1}$$

k : Boltzmann constant (1.38×10^{-23} J/K)

T : temperature [K]

μ : mobility of positive ion (represented by SF_5^+: 0.7×10^{-4} $m^2/(V\cdot sec)$[9])

Here, the temperature distribution in and around a PD channel is assumed with the gaussian-type distribution expressed by Eq. (3.2).

$$T = 1700\ exp\left[-\left(\frac{d}{50\times10^{-6}}\right)^2\right] + 300 \tag{3.2}$$

d : distance in radial direction from the central axis of PD channel [m]

Equation (3.2) is derived from the followings;

(1) Temperature of circumstance gas is 300 K.

(2) Maximum temperature at the central axis of PD channel is 2000 K[1].

(3) Half-width of the temperature distribution is 50 μm, as shown by broken curve in Fig. 3,11, which corresponds to the radius of the PD channel[10].

(4) Temperature distribution is time-independent.

The distribution of positive ion density can be calculated by Eq. (3.3).

$$\frac{n}{n_0} = \frac{1}{\sqrt{4\pi Dt}}\ exp\left[-\frac{d^2}{4Dt}\right] \tag{3.3}$$

n : number of ions at the time t after PD generation and at the distance d

n_0: number of ions at $t = 0$ at $d = 0$

The calculation results for different time after PD generation are shown by solid curves in Fig. 3.11. As the time goes on, the number of ions at $d = 0$ decreased drastically, while the width

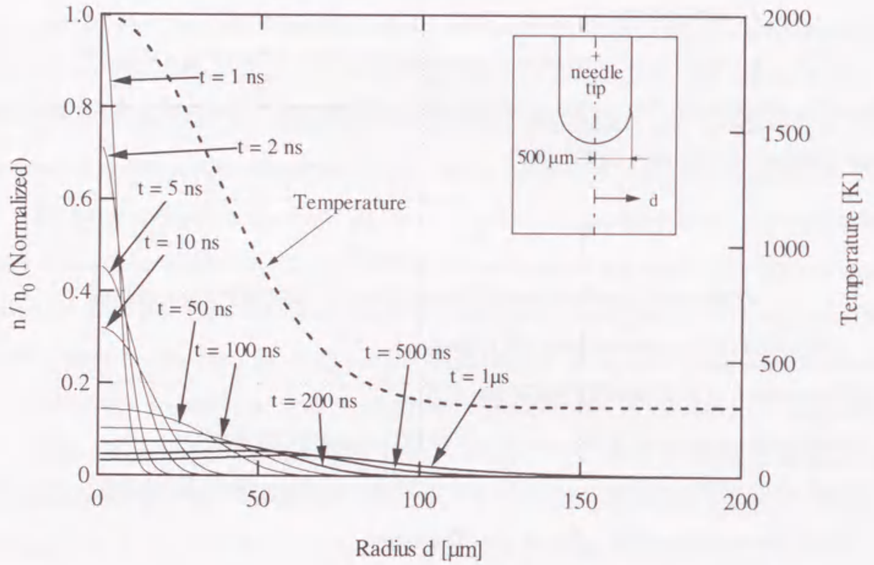

Fig. 3.11 Positive ion distribution due to ion diffusion.

of ion distribution increases in the radial direction of needle electrode. In comparison with the needle tip radius of 500 μm, it is reasonable to recognize that positive ions could diffuse in the radial direction of needle electrode from 200 ns to 1 μs after PD generation.

3.6.2 Ion Drift

The trajectory of a positive ion drift into the gap space was calculated using the calculation method mentioned in Section 2.8 under the following assumptions;

(1) Positive ions are generated at the region in 0.3 mm below the needle tip, which corresponds to the PD length.

(2) Ion mobility is considered to be 0.7×10^{-4} m^2/(V·sec)[9].

(3) Collisions between the positive ion and the other particles are neglected.

(4) Electric field formed by space charges is neglected.

Figure 3.12 shows the calculated trajectories of positive ion drift for different applied voltages. Figure 3.12 means that positive ions generated by PD at the needle tip could reach the plane electrode after 1 ms, irrespective of the applied voltage under the gap space of 10 mm. The enlarged trajectory within 1 μs is shown in Fig. 3.13 for V_a = +25 kV. Figure 3.13 also includes the width of ion distribution associated with ion diffusion at 200 ns, 500 ns and 1 μs, respectively, calculated in Fig. 3.11, where the number of ions decreased into 3% of that at d = 0. In other words, the hatched area in Fig. 3.13 schematically shows the prospective volume of positive ions. In comparison with the scale and shape of needle tip illustrated in Fig. 3.13 as well as the gap length of 10 mm, it is reasonable to recognize that the positive ions could remain in the vicinity of the needle tip at 1 μs after PD generation.

Considering the scattering in the location of PD inception on the needle tip, the above two calculated results confirm that the PD-induced positive ions diffuse at first in the radial direction of needle electrode, and afterwards, they begin to drift into the gap space. These results support the sequential PD generation characteristics and their mechanism in SF_6 gas described in the

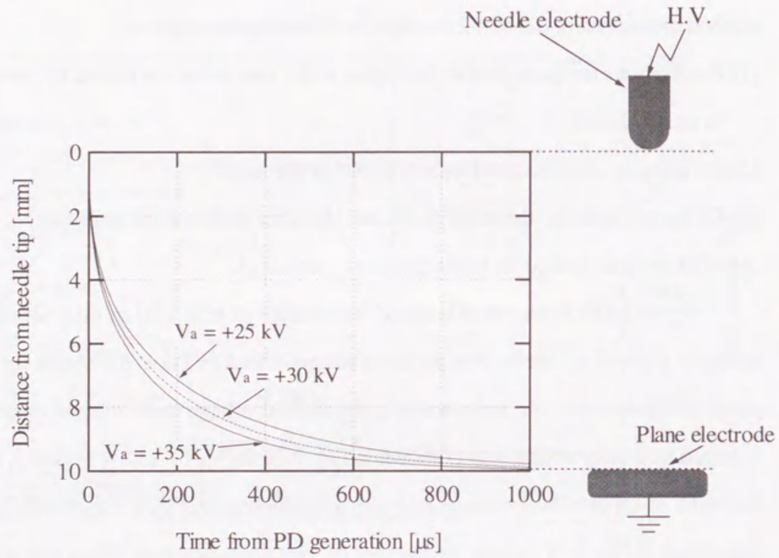

Fig. 3.12 Trajectories of positive ion drift.
(g = 10 mm, r = 500 μm, in SF_6 gas, P = 0.1 MPa, positive dc.)

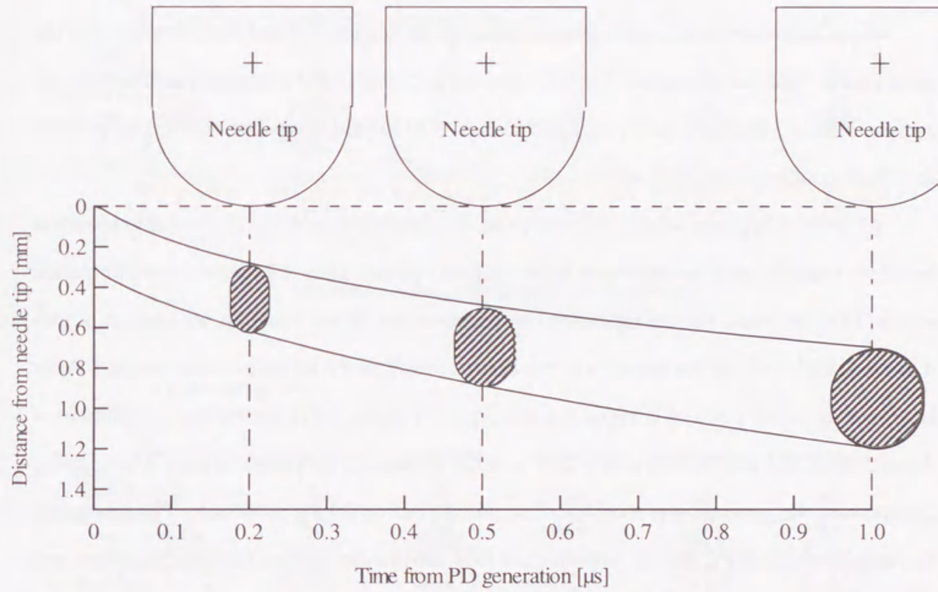

Fig. 3.13 Trajectories of positive ion drift and prospective volume of positive ions.
(g = 10 mm, r = 500 μm, in SF_6 gas, P = 0.1 MPa, positive dc.)

previous section with the schematic illustration of space charge behavior and corona stabilization effect in Fig. 3.10.

3.7 Applied Voltage Dependence of Space Charge Behavior under Positive dc Voltage Condition

From the model of the space charge behavior in Section 3.5 and the calculation of the space charge behavior in Section 3.6, the relationship between PD generation mechanism and the space charge behavior can be concluded in Figs. 3.14 (a) and (b) at lower and higher positive dc voltage conditions, respectively.

At lower voltage application of positive dc, the generation probability of an initial electron decreases together with the reduction of the critical volume. Thus, there can be certain period without PD generation, i.e., the repetition rate becomes low. In this situation, the number of ions at around the needle tip decreases, and the corona stabilization effect becomes weaker. After that, once an initial electron is created in the critical volume, a PD with a large magnitude of charge occurs and newly generates a large number of positive and negative ions. The negative ions increase the generation probability of an initial electron for the subsequent PD, increasing the repetition rate of PD pulses. The positive ions activate the corona stabilization effect and make the charge magnitude of the subsequent PD small. Thus, a number of PD with small magnitude of charge are generated after the large PD pulse.

On the other hand, at higher voltage application of positive dc, the critical volume is larger than that at lower voltage application, and the generation probability of an initial electron becomes higher. Therefore, the subsequent PD can be generated more easily than that at lower voltage application. The charge magnitude of subsequent PD becomes small due to the activated corona stabilization effect by plenty of positive ions derived from the previous PD with high repetition rate. This model can be applied to the region where plenty of small PD occurs under positive half

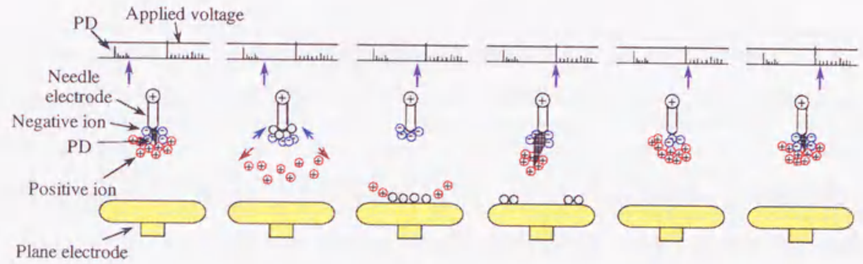

(a) Lower voltage application of positive dc.

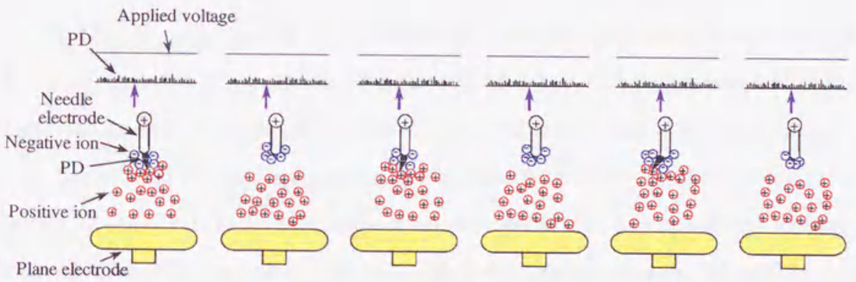

(b) Higher voltage application of positive dc.

Fig. 3.14 Schematic illustration of PD generation mechanism under positive dc condition.

cycle of ac voltage condition. This is because the temporal change of the instantaneous applied voltage value under ac voltage application, which is in ms order, is quite longer than the time interval between two successive PD of several 100 ns.

3.8 Conclusions

In this chapter, the measurement system for sequential generation characteristics of PD in SF_6 gas with long-term, high time-resolution was constructed. Then, the sequential PD generation characteristics for ac and dc voltage conditions were measured. In order to clarify the sequential PD characteristics, the relationship between the magnitude of PD charge and its preceding time was discussed with consideration of space charge behavior as follows;

(1) The sequential PD generation characteristics for ac voltage condition showed the larger magnitude of PD (first PD) and the smaller magnitude of PD (subsequent PD) in positive half cycle. The charge magnitude of the first PD depended on the instantaneous voltage, while that of subsequent PD was small and irrespective of the instantaneous voltage.

(2) PD with large magnitude of charge was followed by the subsequent PD with small magnitude of charge for lower voltage application of positive dc. On the contrary, PD with only small magnitude of charge was generated under higher voltage application of positive dc.

(3) Negative correlation of $q - \Delta t$ characteristics was found at small Δt region, which was derived from the activated corona stabilization effect due to the ion diffusion in the radial direction of needle electrode. On the other hand, positive one was found at large Δt region, which was attributed to the relaxed corona stabilization effect due to the ion drift into the gap space.

(4) A simulation model of space charge behavior was established that positive ions firstly diffuse in the radial direction of needle electrode and secondly drift into the gap space, and verified by numerical calculations of diffusion and drift processes for positive ions after PD generation.

References

[1] I.Gallimberti and N.Wiegart: "Streamer and Leader Formation in SF_6 and SF_6 Mixtures under Positive Impulse Conditions: II. Streamer to Leader Transition", *Journal of Physics D: Applied Physics*, Vol. 19, No. , pp. 2363-2379, 1986.

[2] L.Niemeyer: "Leader Breakdown in Compressed SF_6: Recent Concepts and Understanding", *Gaseous Dielectrics VI*, pp. 49-59, Plenum Press, New York, 1991.

[3] N.Wiegalt, L.Niemeyer, F.Pinnekamp, W.Boeck, J.Kindersberger, R.Morrow, W.Zaengl, M.Zwicky, I.Gallimberti and S.A.Boggs: "Inhomogeneous Field Breakdown in GIS - The Prediction of Breakdown Probabilities and Voltages - Part III: Discharge Development in SF_6 and Computer Model of Breakdown", *IEEE Transactions on Power Delivery*, Vol. 3, No. 3, pp. 939-946, 1988.

[4] C.Heitz: "A Generalized Model for Partial Discharge Processes Based on a Stochastic Process Approach", *Journal of Physics D: Applied Physics*, Vol. 32, pp. 1012-1023, 1999.

[5] R.J.Van Brunt, P.von Glahn and T.Las: "Nonstationary Behaviour of Partial Discharge during Discharge Induced Ageing of Dielectrics", *IEE Proceedings - Science, Measurement and Technology*, Vol. 142, No. 1, pp. 37-45, 1995.

[6] M.F.Fréchette, M.Côté, N.G.Trinh and R.Y.Larocque: "Partial-discharge Activity for a Negative dc Corona in Atmospheric SF_6", *1994 IEEE International Symposium on Electrical Insulation*, pp. 301-304, 1994.

[7] J.P.Novak: "Empirical Model of Breakdown in SF_6: Corona-shielding Effect", *Journal of Applied Physics*, Vol. 66, No. 12, pp. 5791-5797, 1989.

[8] M.S.Bhalla and J.D.Craggs: "Measurement of Ionization and Attachment Coefficients on Sulphur Hexafluoride in Uniform Fields", *Proceedings of Physical Society*, Vol. 80, pp. 151-160, 1962.

[9] J.de Urquijo-Carmona, I.Alvarez, H.Martinez and C.Cisneros: "Mobility and Longitudinal Diffusion of SF_3^+ and SF_5^+ in SF_6", *Journal of Physics D: Applied Physics*, Vol. 23, No. 7, pp. 778-783, 1991.

[10] S.K.Dhali and A.K.Pal: "Numerical Simulation of Streamers in SF_6", *Journal of Applied Physics*, Vol. 65, No. 5, pp. 1355-1362, 1988.

Chapter 4 Long-term Sequential Characteristics of Negative Partial Discharge in Pressurized SF_6 Gas

4.1 Introduction

SF_6 gas insulated electric power apparatus such as GIS and GIL have been operated under high gas pressure condition at around 0.5 MPa·abs[1, 2], in order to achieve the higher insulation property. Here, metallic particle contaminants in GIS would generate negative partial discharges (PD) firstly, because negative PD inception voltage is lower than positive one. In such high gas pressure condition, there is a possibility that breakdown occurs without replete positive PD precursor to it. In this case, only the measurement of negative PD could be a method for the insulation diagnosis. Moreover, some dc GIS have been introduced into the electric power transmission system recently[3]. Free metallic particle contaminants in dc GIS with positive polarity stand up on the inner surface of GIS by the electrostatic force[4], and generate negative PD. Therefore, in the commissioning process and under operation, it is important for the insulation diagnosis at the early stage to clarify the negative PD mechanism under high gas pressure condition.

In this chapter, an inhomogeneous electric field configuration with a low voltage needle electrode is used in order to simulate the condition just after a needle protrusion stands. Moreover, taking consideration of the actual on-site testing process of GIS, the negative PD characteristics are measured up to 6 hours. The generation mechanism of the negative PD and temporal transition of the negative PD characteristics are discussed.

4.2 Approach

The electrical signals generated by PD at minor defects contain relevant information for aging by the defects in the early stages. The information could serve to define and detect precursor signs to a PD phenomenology leading to further degradation or major faults of a gas-insulated system.

The sudden apprearance of PD must be observed with high-time resolution. In addition to the time resolution which allows us to access to pulse-to-pulse relationships, the present approach permits to record a large amount of data, consisting of consecutive time frames. With this approach, the early stage of PD phenomena featuring erratic and low-intensity discharges could be studied[5, 6]. Moreover, once a set of parameters defining a discharge regime is unraveled and defined monitoring these parameters could assist confirming the insulation reliability and performance of GIS for a long term. In the chapter, the approach is applied to the situation at which a lot of PD occur. The study aims at establishing the capabilities of the approach to a situation characterized by a high discharge activity.

4.3 Experimental Setup

Figure 4.1 shows the experimental setup. In the experimental chamber shown in Fig. 4.2, a plane-needle-plane electrode system was constructed with two plane electrodes made of brass, both of which had a Rogowski-like profile with the radius of 85 mm. Figure 4.3 shows the electrodes configuration. One plane electrode was connected to a dc high voltage source, below which the other one was placed and grounded. A needle electrode with the diameter of 0.55 mm was set through a hole of the grounded plane electrode without touching it. The material of the needle electrode was Tin having low melting point, due to unraveling the influence of the needle tip condition on negative PD for a long term easily. The tip of the needle electrode was cut off

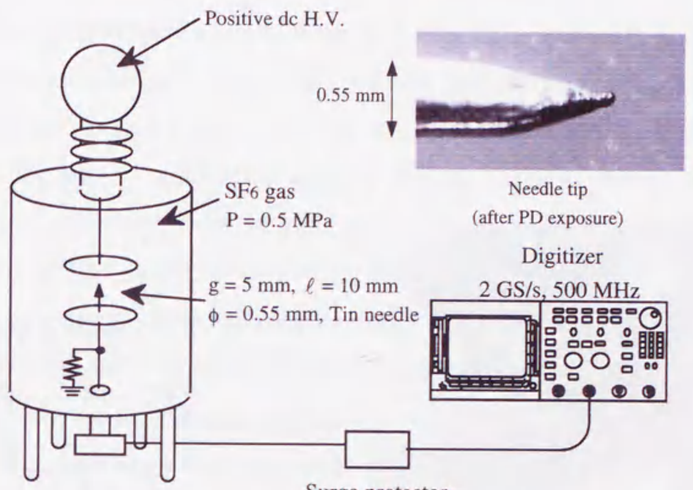

Fig. 4.1 Experimental setup.

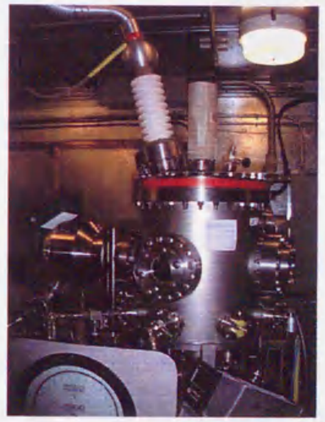

Fig. 4.2 Experimental chamber.

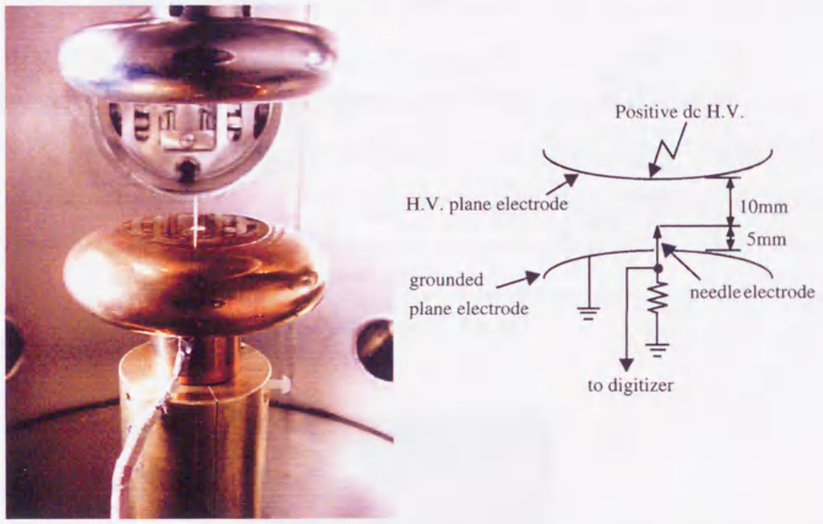

Fig. 4.3 Electrode setup.

sharply, as shown in Fig. 4.1. The length of the needle electrode was 10 mm and the gap length was 5 mm. The positive dc high voltage was applied to the upper electrode in order to generate the negative PD at the tip of the needle electrode.

The needle electrode was grounded through a detecting impedance of 50 Ω having wide band frequency response from dc to 1 GHz and more. The PD current pulse flowing on the needle electrode was measured by a high speed digitizer (Tektronics RTD720A, sampling rate: 2 GS/s, analog bandwidth: 500 MHz, acquisition length: 1 Mpoints) through the detecting impedance. The minimum sensitivity of the measuring system was about 0.02 mA, which is equivalent to 0.02 pC, because the rise time and the fall time of the PD current pulse waveform in SF_6 gas are generally 1 ns and the integration of the waveform corresponds to the magnitude of charge. The digitizer was controlled by a personal computer through GP-IB connection and the obtained data was stored in the computer.

The PD current pulses were measured as the sequential generation characteristics of PD pulses by the digitizer for 0.5 ms per acquisition. Thus, a frame was defined as one acquisition of the digitizer for 0.5 ms. The data acquisitions could achieve at least every 20 seconds. The obtained data, which was stored into the computer, were analyzed with 3 stages; the noise reduction, the location of PD pulse occurrence and the statistical analyses.

In this experiment, the chamber was filled with SF_6 gas with the pressure P = 0.5 MPa converted to 20 °C. All experiments were carried out under room temperature.

4.4 Sequential Characteristics of Negative Partial Discharge

Figure 4.4 shows the typical sequential characteristics of negative PD at applied voltage V_a = +59 kV obtained by 20-minute voltage application. As can be seen in Fig. 4.4, a PD train with high repetition rate occurred, and after time with sporadic PD generation elapsed, successive PD generation could be observed again.

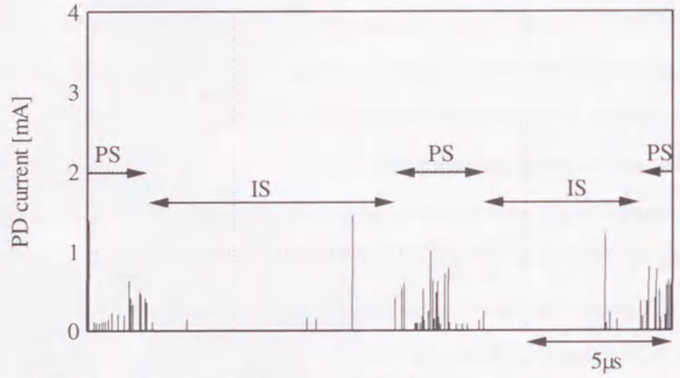

Fig. 4.4 Typical sequential PD generation characteristics.
($g = 5$ mm, $\phi = 0.55$ mm, in SF_6 gas, $P = 0.5$ MPa, $V_a = 59$ kV, negative dc, by 20-minute voltage application.)

Figure 4.5 shows the relationship between PD current pulse height I and its preceding time Δt by 20-minute voltage application. As can be seen in Fig. 4.5, PD with smaller preceding time had smaller pulse height, however, PD with smaller pulse height was accompanied with not only smaller preceding time but also larger one. Thus, 95% of the obtained PD were satisfied with Eq. (4.1), whose limit was determined taking consideration of the scattering and is shown in Fig. 4.5.

$$I \leq 0.641 \cdot \log(\Delta t) + 1.573 \tag{4.1}$$

I: PD current pulse height [mA]

Δt: preceding time [μs]

Here, the inception of Δt axis was fixed as 3.5 ns, which was corresponding to the minimum time interval between two individual PD pulses. The relationship between I and Δt shown in Fig. 4.5 closely related to the electric field distribution in the vicinity of the needle tip will be discussed in Section 4.6.

From Fig. 4.4, successive PD pulses with shorter time interval could be found. Thus, a pulse train consisted by the successive 6 or more PD pulses with time interval between each PD pulses of less than 600 ns was focused on and determined it as a pulse sequence (PS), and PD excluded PS were defined as an inter sequence (IS). Figure 4.6 shows the relationship between the number of PD pulses in PS and the time duration of the PS observed in one acquisition (0.5 ms). As can be seen in Fig. 4.6, the number of PD pulses in PS was proportional to the time duration of the PS.

4.5 Long-term Temporal Transition of Sequential Partial Discharge Characteristics

Figure 4.7 shows the temporal transition of the number of PD in each acquisition (0.5 ms). Note that the data acquisition were carried out for 10 times in each measuring point of time, so that the number of PD shown in Fig. 4.7 shows the averages and standard deviations for the 10 acquisitions as plots and error bars, respectively. As can be seen in Fig. 4.7, the number of PD

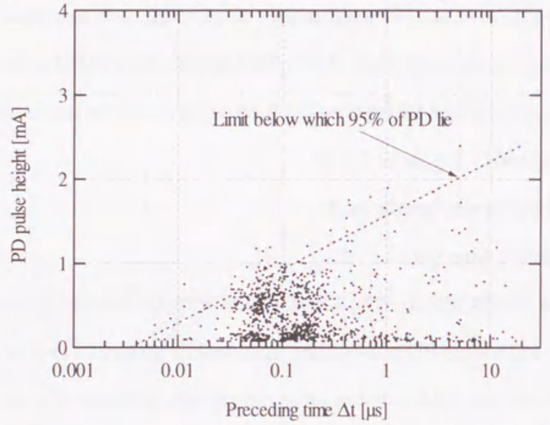

Fig. 4.5 Relationship between PD pulse height I and preceding time Δt.
(g = 5 mm, ϕ = 0.55 mm, in SF_6 gas, P = 0.5 MPa, V_a = 59 kV, negative dc, by 20-minute voltage application.)

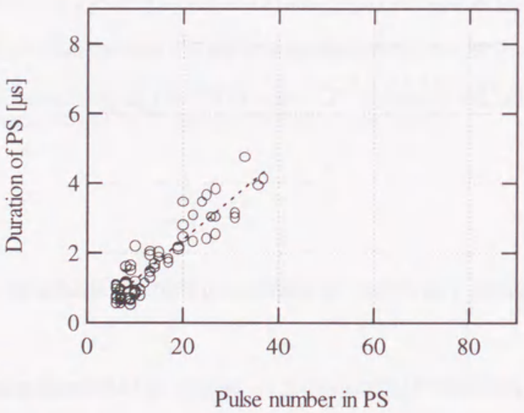

Fig. 4.6 Relationship between number of PD pulses in PS and duration of PS.
(g = 5 mm, ϕ = 0.55 mm, in SF_6 gas, P = 0.5 MPa, V_a = 59 kV, negative dc, by 20-minute voltage application.)

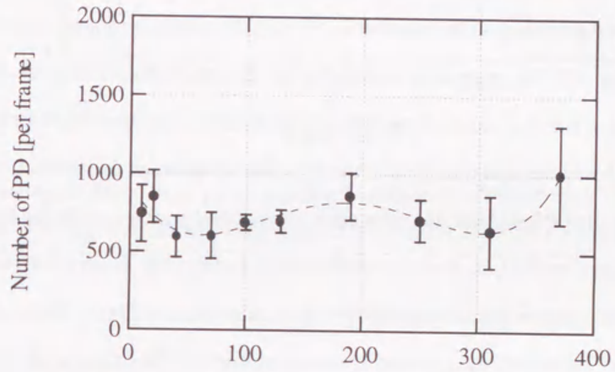

Fig. 4.7 Temporal transition of number of PD in each acquisition (0.5 ms).
(g = 5 mm, ϕ = 0.55 mm, in SF_6 gas, P = 0.5 MPa, V_a = 59 kV, negative dc.)

decreased with some fluctuation for the first 1 hour and fluctuated widely after that.

The relationship between I and Δt was evaluated for other measuring points of time as shown in Fig. 4.5 and the limit below which 95% of PD lie such as Eq. (4.1) was calculated for each case. Figure 4.8 shows the temporal transition of the slope of the limiting line. As can be seen in Fig. 4.8, the slope had little time trend. This means that the electric field distribution in the vicinity of the needle tip had little time dependency, whose detail will be discussed in Section 4.6.

The duration of PS differes from each other and can be a characteristic parameter to desctibe the discharge regime. Thus, the number of PS with longer duration was estimated. Figure 4.9 shows the temporal transition of the number of PS with 20 pulses or more in one acquisition. As can be seen in Fig. 4.9, the generation probability of PS with 20 pulses or more decreased with some fluctuation at the beginning of the voltage application, and then increased after voltage application at 310 minutes and more. Here, the relationship between the number of PD pulses in PS and the duration of PS was evaluated for each acquisition by means of fitting to a straight line using a least square method as shown in dodtted line in Fig. 4.6. Figure 4.10 shows the time dependency of the slope of the calculated lines. As can be seen in Fig. 4.10, the slope had little time dependency. Therefore, the generation characteristics of PD pulses with small preceding time, namely PD within PS, had little time dependency, however, the number of PD pulses and the duration of PS had time trend.

Here, PD train constructed with less than 6 pulses and PD with preceding time of longer than 600 ns were excluded from the analyses of PS as shown in Figs. 4.9 and 4.10. Thus, the characteristics of PD pulses in IS were evaluated. Figure 4.11 shows the ratio of the number of PD pulses in IS to the number of total PD pulses in each acquisition as a function of the time for voltage application. As can be seen in Fig. 4.11, the ratio had the similar time trend to the inverse of the time trend of the number of total PD pulses in Fig. 4.7.

Moreover, the total amount of charge during one acquisition was calculated with consideration that the PD with magnitude of 1 mA was equivalent to the charge amount of 1 pC. The total amount of charge for all PD shown in Fig. 4.12 (a) had the same time dependency as

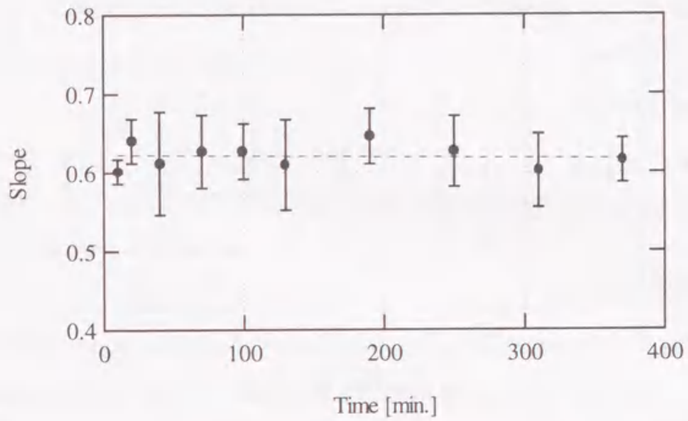

Fig. 4.8 Time dependence of slope of limiting I - Δt curve below which 95% of PD lie.
(g = 5 mm, ϕ = 0.55 mm, in SF_6 gas, P = 0.5 MPa, V_a = 59 kV, negative dc.)

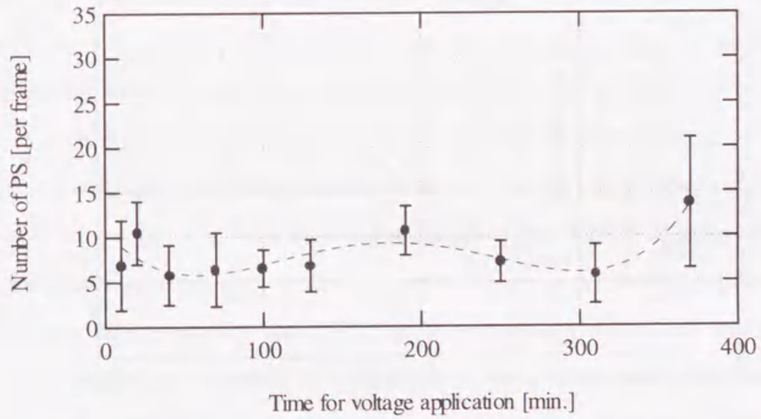

Fig. 4.9 Temporal transition of number of PS with 20 pulses or more.
(g = 5 mm, ϕ = 0.55 mm, in SF_6 gas, P = 0.5 MPa, V_a = 59 kV, negative dc.)

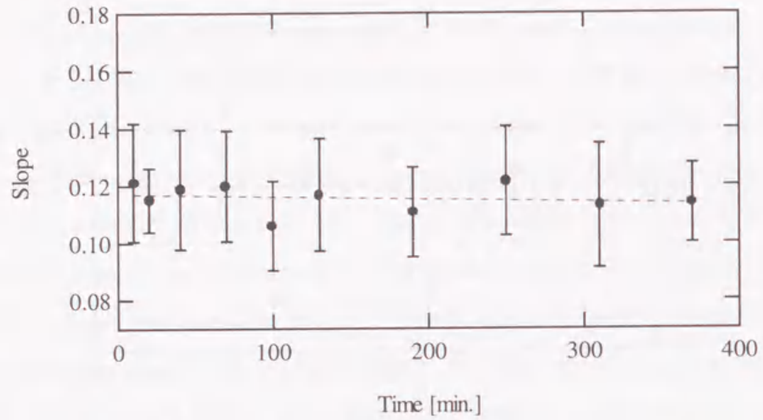

Fig. 4.10 Time dependence of slope of relationship between number of PD in PS and duration of PS.
(g = 5 mm, ϕ = 0.55 mm, in SF_6 gas, P = 0.5 MPa, V_a = 59 kV, negative dc.)

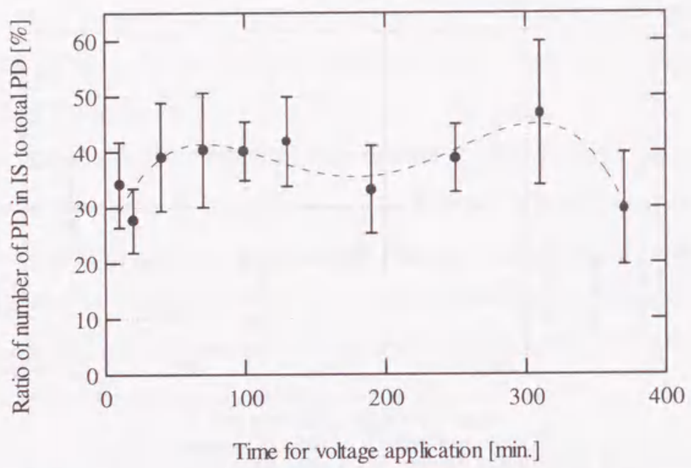

Fig. 4.11 Time dependence of number of PD in IS to number of total PD ratio.
(g = 5 mm, ϕ = 0.55 mm, in SF_6 gas, P = 0.5 MPa, V_a = 59 kV, negative dc.)

that for the number of PD pulses as shown in Fig. 4.7, etc. The total amount of charge for PD in PS shown in Fig. 4.12 (b) had the same trend as that for the total amount of charge for all PD in Fig. 4.12 (a). However, the total amount of charge for PD in IS in Fig. 4.12 (c) showed little time dependency. Therefore, the total charge for all PD was dominated by the PD occurring in PS.

4.6 Sequential Negative Partial Discharge Generation Mechanism under Higher Gas Pressure Condition

The results mentioned in the previous sections can be explained from viewpoints of the space charge behavior and the condition of the needle tip surface as follows.

Once negative PD occurs, a lot of positive and negative ions are generated in the vicinity of the needle tip. The negative ions relax the electric field strength at around the needle tip. The positive and negative ions drift toward the needle surface and the plane electrode, respectively. Thus, the longer the time elapses from the preceding PD generation, the less the relaxation of the electric field at around the needle tip becomes, which limits the PD current pulse height as shown in Fig. 4.5 and Eq. (4.1). Here, an initial electron for a negative PD is an electron emitted from the needle surface due to the field emission, the positive ion bombardment, etc. In case the electron emitted from the needle surface collides with the SF_6 molecular with an energy too small to ionize it, the electron would be attached to the SF_6 molecular and form a negative ion[5]. Thus, a lot of negative ions would exist in the gap space even without PD generation. In this case, the electric field strength at around the needle tip is weakened by such negative ions and consequently, PD with smaller magnitude of pulse height would be generated even with larger preceding time. This process would be independent of the condition of the needle tip surface and shape. Therefore, PD characteristics inside the pulse train having smaller preceding time, namely PD in PS, had little time trend.

In case the negative ions are accumulated in the gap space and their amount increases

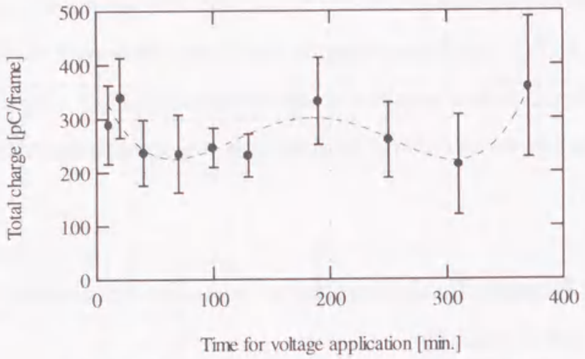

(a) Total amount of PD charge for all PD pulses.

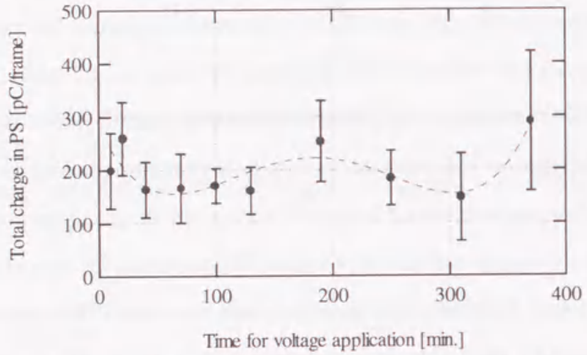

(b) Total amount of PD charge for PD pulses in PS.

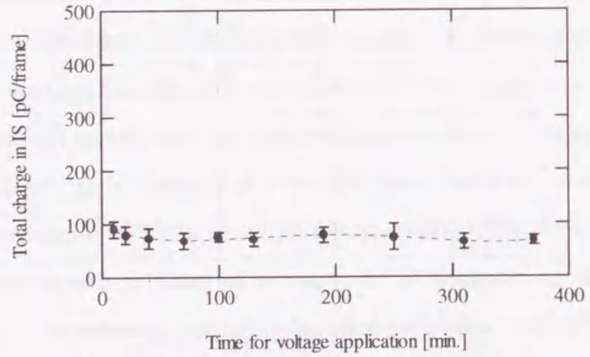

(c) Total amount of PD charge for PD pulses in IS.

Fig. 4.12 Time dependence of total amount of PD charges in one acquisition.
(g = 5 mm, ϕ = 0.55 mm, in SF_6 gas, P = 0.5 MPa, V_a = 59 kV, negative dc.)

enough to suppress the generation probability of the initial electron, the pulse train ceases. Here, the generation probability of the initial electron depends on the surface condition of the needle tip such as surface roughness and the accumulated discharge decomposition, which depends on the exposure of PD and much affects the field emission. The degree of the surface roughness decreases and the amount of the discharge decomposition on the needle tip increases with the PD exposure. Thus, the generation probability of the initial electron would once decrease in the early stage of voltage application due to the decrease of the surface roughness, and fluctuate in further stage due to the accumulation of the discharge by-products. Therefore, the number of PD pulses and PS with 20 pulses or more once decreased with some fluctuation and then showed larger scattering as shown in Figs. 4.7 and 4.9, respectively.

From comparison between Figs. 4.12 (a), (b) and (c), the total charge amount of all PD pulses was dominated by the total amount of PD pulses in PS. Moreover, the time trend of the number of PD pulses in Fig. 4.5 had the same trend as that of the number of the PD with larger number of pulses. Therefore, the time trend mentioned before were characteristic features for negative PD in the highly pressurized SF_6 gas.

4.7 Conclusions

The sequential generation characteristics of negative PD under high gas pressure condition were observed for a long term up to 6 hours. The statistical analyses were carried out for the obtained sequential PD pulses focused on the PD current pulse height and the preceding time. Consequently, the followings were revealed:

(1) The sequential PD generation with smaller preceding time occurred, which sometimes ceased.

(2) The pulse sequence (PS), which was determined as the pulse train consisted by 6 or more successive PD pulses having time interval between each two PD pulses of less than 600 ns,

was analyzed. The duration of PS depended strongly on the number of PD pulses in PS.

(3) The duration of PS decreased in the early stage of the long-term PD generation, and then fluctuated. On the other hand, the sequential PD generation characteristics in PS showed little time trend.

(4) The number of PD pulses also had a time dependency; it decreased in the early stage, and then fluctuated as the similar tendency as the time transition of the number of PS with larger number of pulses.

(5) The time transition of the number of PD and the number of PS with larger number of pulses were explained by the initial electron generation mechanism; surface roughness of the needle electrode was degraded in the early stage and the discharge decomposition was accumulated in the later stage, which caused the decrease and fluctuation of the generation probability of the initial electron, respectively.

(6) Temporal transition of the total amount of charge per one acquisition showed that the most determinant pulses were included in PS. Moreover, its time trend was the same as that of the total number of PD, the number of PS with larger number of pulses and the inverse of ration of the number of PD in IS to that of total PD.

Consequently, it was concluded that the PD pulse train with short preceding time was characteristic and dominant phenomena in negative PD under highly pressurized SF_6 gas condition. The measurement of the sequential PD generation characteristics can be easily applied to the actual gas insulated apparatus. Furthermore, this technique for the negative PD is important for the beginning of the particle behavior. Therefore, the experimental results and analyzing techniques mentioned in this chapter are expected to be developed into the insulation diagnosis, especially the status analysis of PD characteristics and insulation condition.

References

[1] H.Okubo, T.Hoshino, T.Takahashi, M.Hikita and A.Miyazaki: "Insulation Design and On-site Testing Method for a Long Distance, Gas Insulated Transmission Line (GIL)", *IEEE Electrical Insulation Magazine*, Vol. 14, No. 6, pp. 13-22, 1998.

[2] V.F.Salatko, J.R.Villalba, F.Kemper, V.Fleury and H.P.Szente Varga: "500 kV SF_6 GIS at Itaipu Hydro-station", *IEEE Transactions on Power Delivery*, Vol. 4, No. 1, pp. 186-200, 1989.

[3] T.Hasegawa, K.Yamaji, M.Hatano, F.Endo, T.Rokunohe and T.Yamagiwa: "Development of Insulation Structure and Enhancement of Insulation Reliability of 500 kV dc GIS", *IEEE Transactions on Power Delivery*, Vol. 12, No. 1, pp. 194-202, 1997.

[4] C.M.Cooke, R.E.Wootton and A.H.Cookson: "Influence of Particles on ac and dc Electrical Performance of Gas Insulated Systems at Extra-high-voltage", *IEEE Transactions on Power Apparatus and Systems*, Vol. 96, No. 3, pp. 768-776, 1977.

[5] P.S.Gardiner and J.D.Craggs: "Negative Ions in Trichel Corona", *IEEE-IAS Conference on Electrostatistics*, pp. 148-151, 1978.

Chapter 5 Propagation Characteristics of Electromagnetic Wave Caused by Partial Discharge in Long-distance Gas Insulated Transmission Line

5.1 Introduction

A long-distance SF_6 gas insulated transmission line (GIL) has been developed and is being introduced into the underground electric power transmission system in urban area[1 - 3]. However, the metallic particle contamination in GIL would cause PD leading to breakdown, as is the case with GIS. Thus, it is strongly needed to establish the on-site PD testing method for GIL to verify its insulation performance. Conventional PD testing method for GIS[4, 5] cannot be directly applied to long-distance GIL of several km, because PD signal, especially the electromagnetic wave signal radiated by PD, would be attenuated during a long-distance propagation. Thus, for PD measurement and the reliable insulation diagnosis of GIL with accuracy, it is important to clarify the propagation and attenuation characteristics of PD signal in GIL.

In this chapter, PD current pulse waveforms and its electromagnetic waveforms are measured simultaneously in a full-scale 275 kV GIL model with the length of 168 m. Using the phase gate control method with UHF sensors, the propagation characteristics of PD-induced electromagnetic wave signal in GIL are revealed. Moreover, the wavelet analysis is applied to the estimation of attenuation ratio for different frequency components.

5.2 Experimental Setup

Figure 5.1 shows a single-phase 275 kV class GIL model with a length of 168 m (outer diameter of high voltage conductor: 170 mm, inner diameter of GIL enclosure: 460 mm). Figure 5.2 shows the electrode configuration in GIL. A needle electrode made of stainless-steel with a tip radius r = 500 μm and a length of 20 mm was fixed on the high voltage conductor of the end section of GIL as a PD source. A needle-plane electrode system with the gap length of 30 mm was constructed in the GIL using a plane electrode with the diameter of 30 mm. Only the gas pressure and medium at the end section of GIL could be changed in order to generate PD in different gas conditions. The experimental conditions such as gas pressure, gas medium and applied voltage are shown in Table 5.1. Note that the model GIL except for the end section was filled with SF_6 gas at 0.44 MPa.

Figure 5.3 shows the experimental setup for the simultaneous measurement of PD current pulse waveforms and propagated electromagnetic waveforms in the model GIL. PD current pulse waveforms flowing into the plane electrode were measured by a high-speed digital oscilloscope (LeCroy 9360, sampling rate: 5 GS/s, analog bandwidth: 300 MHz) through a wide-band matching circuit having a frequency response of 1 GHz and more[6]. On the other hand, the propagated electromagnetic waveforms were received by disk-type UHF sensors (diameter: 250 mm, frequency response: 30 MHz to 1.5 GHz and more) and measured by a high-speed wide-band

Table 5.1 Experimental conditions.

Gas medium	Gas pressure	Applied voltage
Air	atmospheric pressure	15 kV_{rms}
SF_6	0.15 MPa	58 kV_{rms}
SF_6	0.40 MPa	58 kV_{rms}

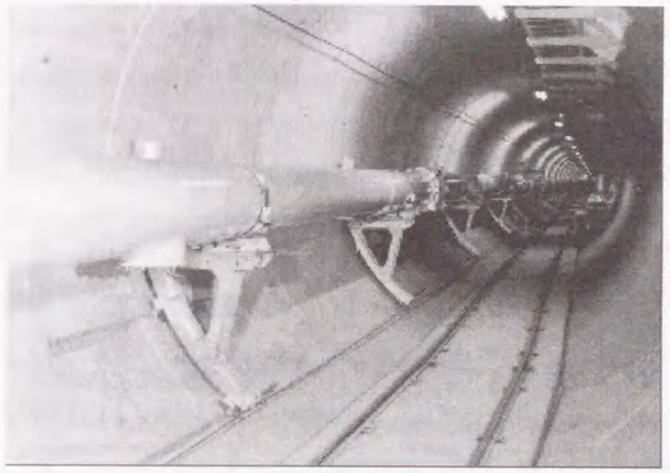

Fig. 5.1 Full-scale 275 kV GIL model.

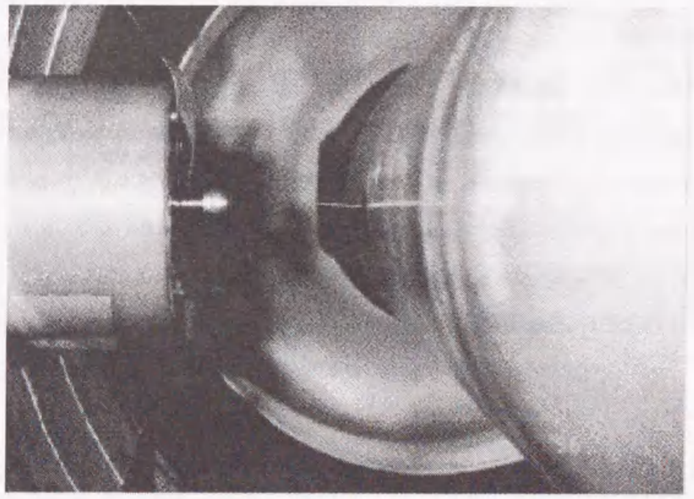

Fig. 5.2 Electrode setup in full-scale 275 kV GIL model.

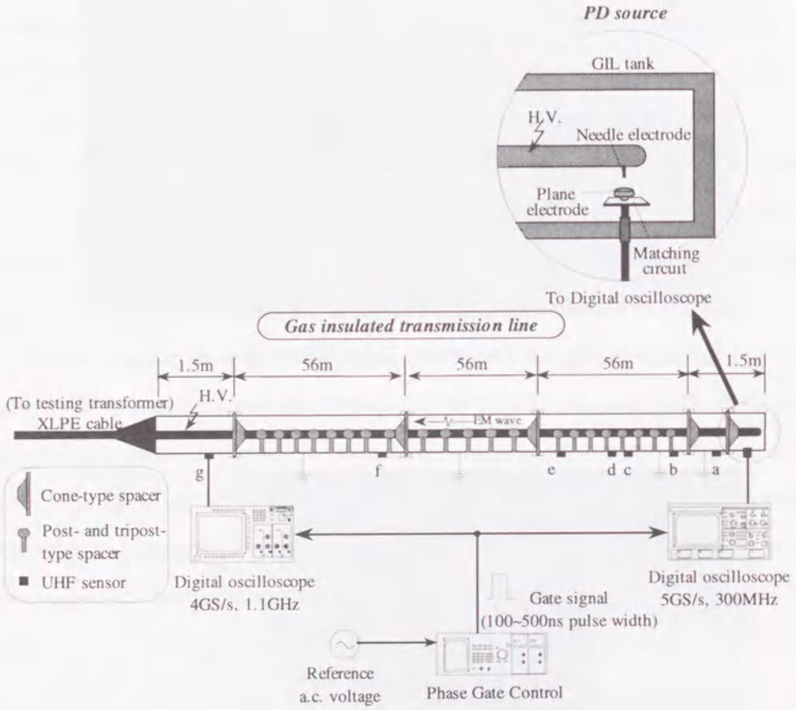

Fig. 5.3 Experimental setup for simultaneous measurement of PD current pulse and electromagnetic waveform in GIL.

digital oscilloscope (Hewlett-Packard, 54720D with plug-in 54721A, sampling rate: 4 GS/s, analog bandwidth: 1.1 GHz) through a wide-band amplifier with the amplitude of 25 dB.

Here, a gate signal with the width of 100 to 500 ns synchronized with the applied ac voltage phase was inputted into two digital oscilloscopes simultaneously in order to achieve the correspondence between the PD current pulse waveform and the electromagnetic waveform emitted from the exact PD. Moreover, the cable lengths into two oscilloscopes were the same in order to use the gate signal as the reference of the propagation time measurement.

5.3 Simultaneous Measurement of Partial Discharge Current Pulse Waveform and Its Electromagnetic Waveform

Figure 5.4 shows the typical PD current pulse waveforms and the corresponding electromagnetic waveforms. Figure 5.4 (a) was measured in the atmospheric air at 270° of the applied ac voltage phase, and Figs. 5.4 (b), (c) and (d) were measured in SF_6 gas with the gas pressure P = 0.15 MPa at 90° of the applied ac voltage phase. Moreover, Figs. 5.4 (a), (b), (c) and (d) were measured at the measuring point g (169.5 m from PD source), c (28 m from PD source), f (112.2 m from PD source) and g (169.5 m from PD source), respectively. The charge magnitude of PD shown in Fig. 5.4 (d) was about 1 pC, which was calculated by the integration of the current waveform. This means that the electromagnetic waveform radiated by such a small PD could be detected clearly at 169.5 m from PD source using the internal UHF sensor.

5.3.1 Propagation Velocity of Electromagnetic Wave in GIL

In Fig. 5.4 (d), the time difference between the rise of the gate signal and that of the PD current pulse waveform was about 30 ns, while about 620 ns passed from the rise of the gate signal to that of the observed electromagnetic waveform. Thus, the electromagnetic wave could

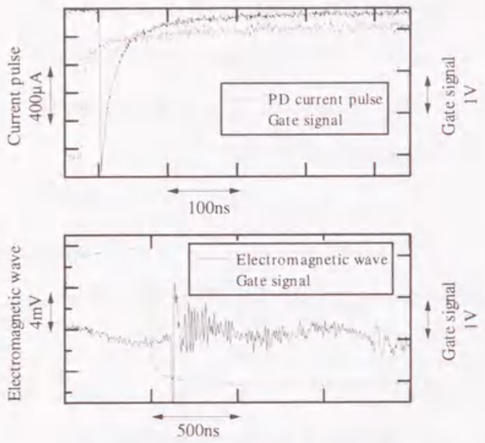

(a) air, $\phi = 270°$, point g (169.5 m).

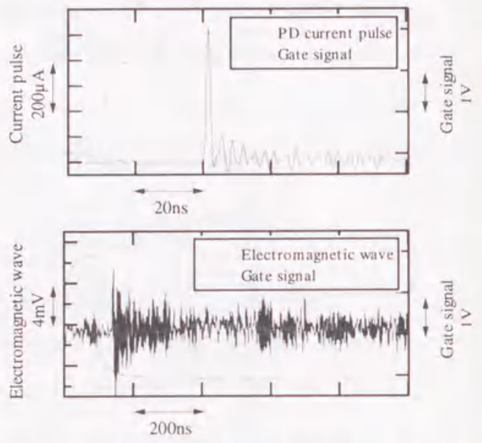

(b) SF_6 gas, 0.15 MPa, $\phi = 90°$, point c (28 m).

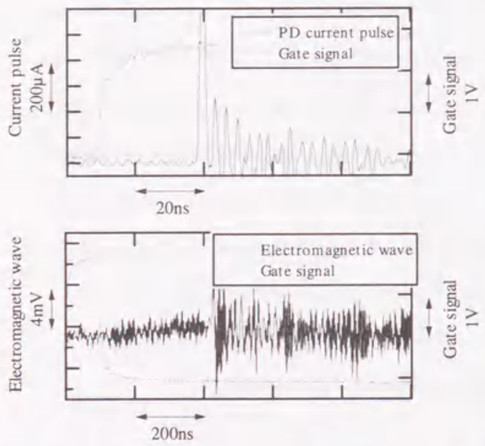

(c) SF_6 gas, 0.15 MPa, $\phi = 90°$, point f (112.2 m).

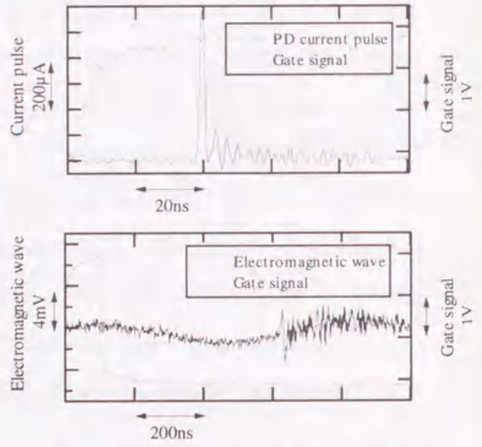

(d) SF_6 gas, 0.15 MPa, $\phi = 90°$, point g (169.5 m).

Fig. 5.4 Simultaneous measurement of PD current pulse and electromagnetic waveforms.

be detected at about 590 ns after PD generation at the measuring point g. The same evaluation was carried out for the other gas conditions. After compensating time delay of the measuring system, the average propagation velocity of the electromagnetic wave was calculated and summarized in Fig. 5.5. As can be seen in Fig. 5.5, the propagation velocity of the electromagnetic wave in the GIL model was 97% to 100% of the velocity of light. Therefore, the electromagnetic wave propagated at almost the same velocity as the velocity of light, in spite of the existence of several kinds and number of spacers in the model GIL.

5.3.2 Relationship between Partial Discharge Current Pulse Waveform and Corresponding Propagated Electromagnetic Waveform

Figure 5.6 shows the relationship between the peak value of PD current pulse and the corresponding electromagnetic wave in SF_6 gas at P = 0.15 MPa. As shown in Fig. 5.6, PD current pulse height had a linear correlation with the height of the corresponding electromagnetic wave signal. Furthermore, the slope of the correlation decreases with increase in the distance from PD source. This is due to the attenuation of electromagnetic wave signal during the long-distance propagation.

Figures 5.7 (a), (b), (c) and (d) show the frequency spectra of PD current pulse waveforms and electromagnetic waveforms, which correspond to those in Figs. 5.4 (a), (b), (c) and (d), respectively. As can be seen in Fig. 5.7 (a), the power gain of PD current pulse in air expanded up to 400 MHz and decreased with the increase in the frequency. On the other hand, in Figs. 5.7 (b), (c) and (d), the power gain of PD current pulse in SF_6 gas consisted of the frequency components higher than 400 MHz. The frequency spectra of the electromagnetic waveforms in Figs. 5.7 (b), (c) and (d) exhibited the peak of power gain at around 300 MHz, and decreased at 400 MHz to 600 MHz down below the noise level. Moreover, peak value of power gain at around 300 MHz decreased gradually with the increase in the distance from the PD source to the measuring point.

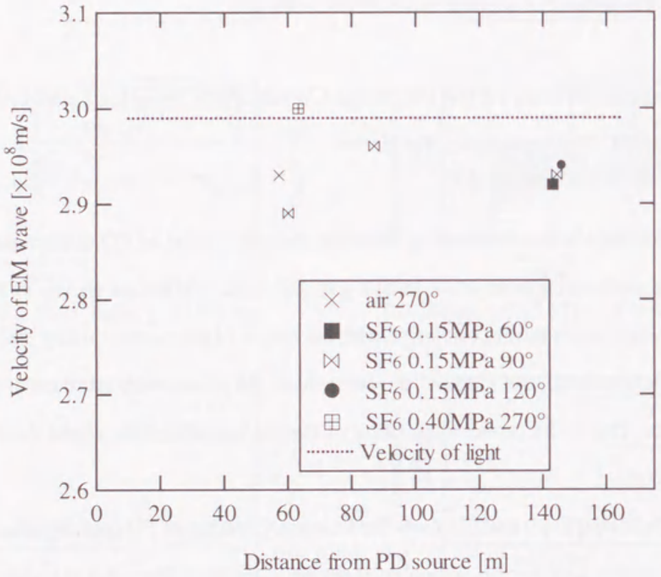

Fig. 5.5 Propagation velocity of electromagnetic wave in GIL.

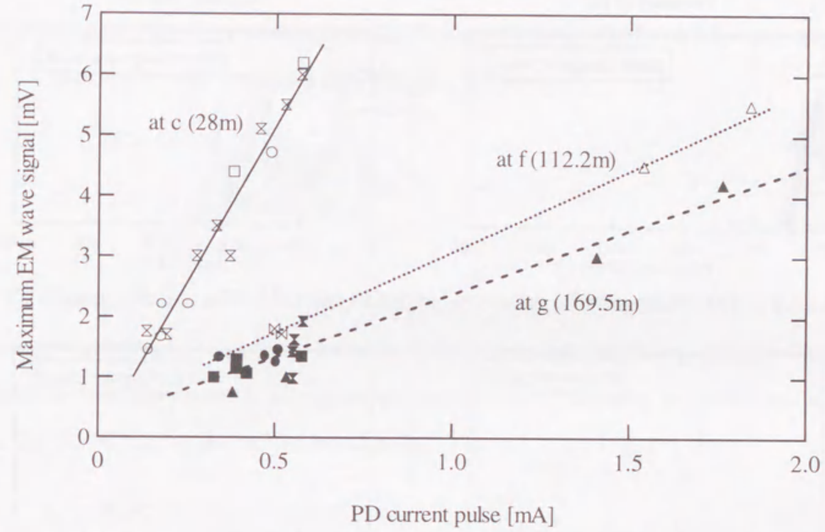

Fig. 5.6 Relationship between PD current pulse height and its electromagnetic wave signal.

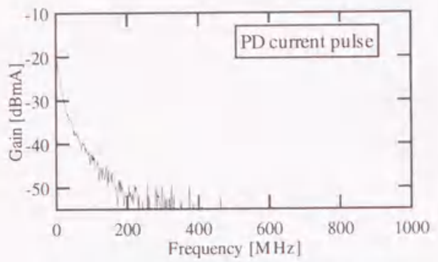

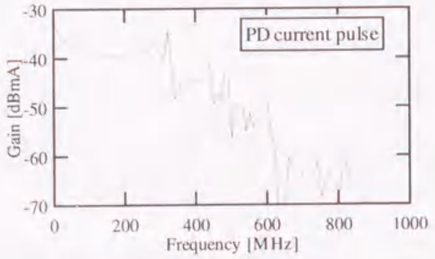

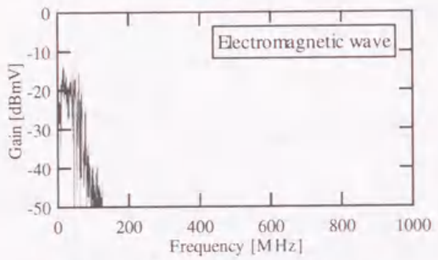

(a) air, $\phi = 270°$, point g (169.5 m).

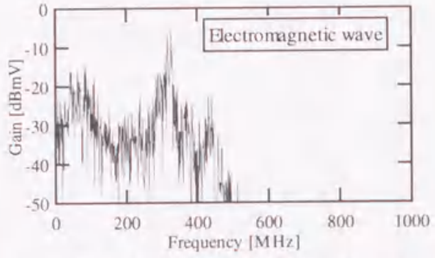

(b) SF_6 gas, 0.15 MPa, $\phi = 90°$, point c (28 m).

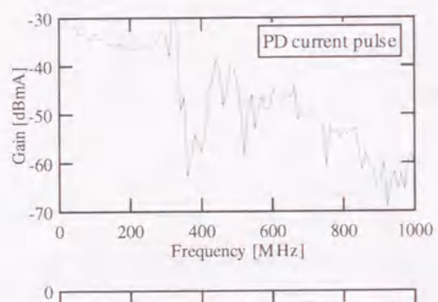

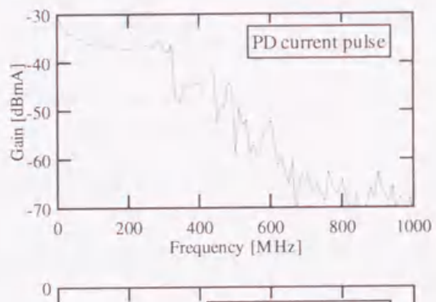

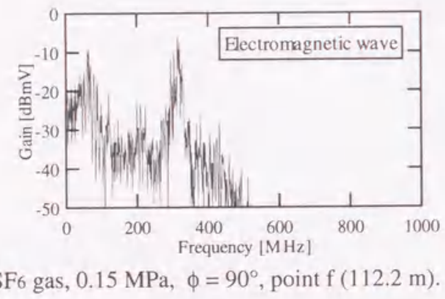

(c) SF_6 gas, 0.15 MPa, $\phi = 90°$, point f (112.2 m).

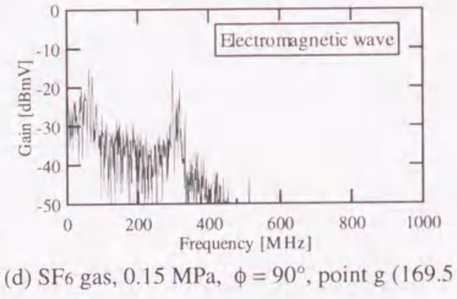

(d) SF_6 gas, 0.15 MPa, $\phi = 90°$, point g (169.5 m).

Fig. 5.7 Frequency spectra of PD current pulse and its electromagnetic waveforms.

5.3.3 Time-frequency Analysis of Electromagnetic Waveform

The wavelet analysis develops the time-domain waveform into the time and frequency axes using the wavelet transform, which is calculated by the convolution of the measured signal and a function called "mother wavelet" that is finite in time and frequency domains. In this subsection, the wavelet analysis is applied to the PD current pulse waveform and the corresponding electromagnetic waveform in order to clarify the temporal transition of each frequency component.

Here, the wavelet transform shown in Eq. (5.1) is used.

$$W_\Psi(a,b) = \int_{-\infty}^{\infty} \frac{1}{\sqrt{|a|}} \overline{\Psi\left(\frac{x-b}{a}\right)} f(x)\, dx \tag{5.1}$$

$f(x)$: obtained signal

$\psi(x)$: mother wavelet

Since the mother wavelet determines the resolution in time and frequency domains, the appropriate selection of a correct mother wavelet is necessary for the effective time-frequency analysis. The Gabor wavelet with relatively narrow in both frequency and time domains shown in Eq. (5.2) is used as the mother wavelet.

$$\Psi(x) = \frac{1}{2\sqrt{\pi}\sigma} e^{-\frac{x^2}{\sigma^2}} e^{-jx}, \quad \sigma = 8 \tag{5.2}$$

As the calculation results can be obtained by the complex value, the signal magnitude of each frequency and time component was expressed by the absolute value. Figure 5.8 shows the time-frequency analysis of the received electromagnetic wave shown in Fig. 5.4 (d). In Fig. 5.8, brighter color means the larger magnitude of signal components. As can be seen in Fig. 5.8, there were several peaks at around 50 to 100 MHz at (a) to (c) and also at around 300 to 450 MHz at (d) to (h), which corresponded to the frequency spectrum with the peak values of power gain in Fig. 5.7 (d). Moreover, the sequential peaks from (a) to (c) and (d) to (h) in Fig. 5.8 meant the temporal transition of each frequency component. Comparison between Fig. 5.4 (d) and Fig. 5.8 suggested that the peaks in the time and frequency domains at the regions (a) and (d) in Fig. 5.8 corresponded to the rise of the electromagnetic wave. The subsequent peaks at the regions (b),

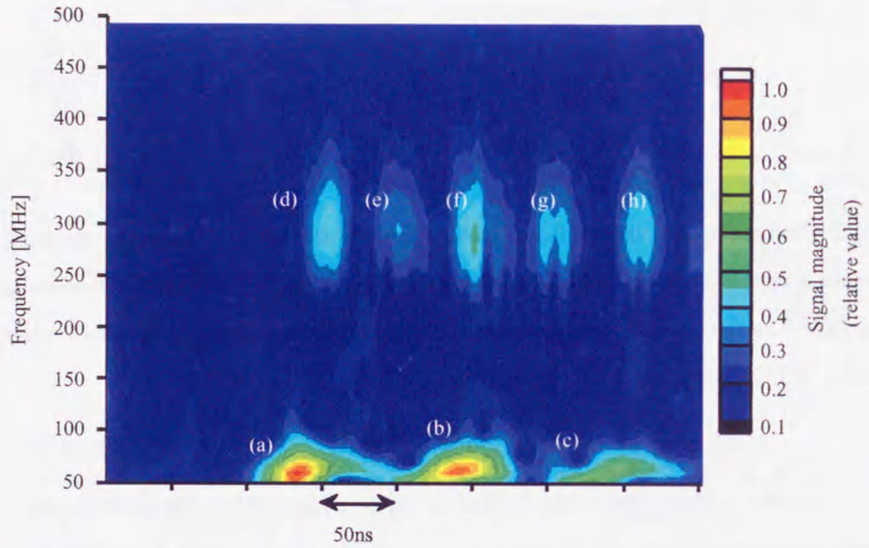

Fig. 5.8 Time-frequency analysis of electromagnetic wave shown in Fig. 5.4 (d).

(c) and (e) to (h) would be due to the signal reflected by the spacers in the GIL model, taking consideration with the time delay from the rise of the signal. Therefore, the wavelet analysis of the electromagnetic waveform allows us to figure out the transient phenomena such as the signal reflection of each frequency component.

5.4 Propagation Characteristics of Electromagnetic Wave in GIL

5.4.1 Attenuation Characteristics of Propagated Electromagnetic Wave

As was shown in Fig. 5.6, the PD current pulse height and the height of the corresponding electromagnetic wave were in positive linear correlation. Thus, the height of the electromagnetic wave can be normalized by the PD current pulse height. Figure 5.9 shows the distance characteristics of the normalized electromagnetic wave signal. As shown in Fig. 5.9, the normalized electromagnetic wave signal was attenuated with increase in the distance from PD source. The slope shows the attenuation rate, which is calculated as about 7.5 dB/100 m. The calculated attenuation rate is relatively small compared with those in the other reports[7, 8], which may be attributed to the selective measurement of the propagated electromagnetic wave corresponding to the PD current pulse waveform.

5.4.2 Frequency Characteristics of Attenuation Rate of Propagated Electromagnetic Wave

In the previous subsection, the attenuation characteristics of the propagated electromagnetic wave were evaluated by means of the normalization by the corresponding PD current pulse height. In this subsection, the attenuation characteristics of the electromagnetic wave are calculated for each frequency component, assuming that each frequency component of the PD current pulse emits the electromagnetic wave with the same frequency component.

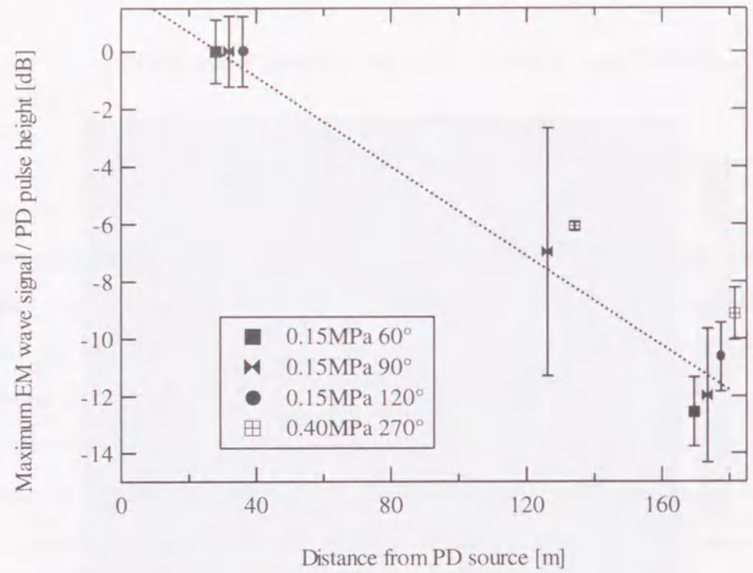

Fig. 5.9 Distance characteristics of normalized magnitude of received electric wave.

Firstly, the time-frequency analyses were carried out for the PD current pulse waveforms and the corresponding electromagnetic waveforms measured at 60°, 90° and 120° of the applied ac voltage phase in SF_6 gas at P = 0.15 MPa. In the analyses, the maximum value of each frequency component of the electromagnetic wave signal was normalized by the same frequency component of the corresponding PD current pulse waveform. The resultant signal magnitude of the propagated electromagnetic wave at the different measuring points was normalized by that at the measuring point c (28 m from PD source). Figure 5.10 shows the distance characteristics of normalized signal magnitude for 50 MHz and 300 MHz components. As can be seen in Fig. 5.10, the attenuation rate increased with the distance from PD source as well as the frequency component, irrespective of the applied ac voltage phase. The attenuation rate at 50 MHz and 300 MHz could be calculated as 2.5 dB/100 m and 8.7 dB/100 m, respectively.

As for the attenuation rate of the electromagnetic wave propagating in the GIL, the results calculated by the other methods have been reported[9, 10]. Table 5.2 shows the attenuation rate of PD signal in GIL for different measuring methods. As can be seen in Table 5.2, a discrepancy exists between the results of simultaneous PD measurement and electromagnetic wave and spectrum observation. This is due to the differences in the PD measuring methods. In other words, simultaneous measurement could obtain data which depended on single PD generation and propagation characteristics, while spectrum observation could measure the average PD characteristics.

Table 5.2 Attenuation rate of PD signal in GIL[9, 10].

Measuring method	Attenuation rate	Comment
Simultaneous measurement of PD current pulse and its electromagnetic wave	50MHz: 2.5 dB/100 m 300MHz: 8.7 dB/100 m	Oscilloscopes and wavelet analysis were used with a comparison of each frequency component.
Frequency span spectrum measurement	Average of 200 to 500 MHz: 5.85 dB/100 m	A spectrum analyzer was used.
Zero span spectrum measurement	50 MHz: 0.72 dB/100 m 300 MHz: 4.5 dB/100 m 400 MHz: 12.2 dB/100 m	A spectrum analyzer and phase gate control method were used.
	Post- and tripost-type spacers: 0.14 to 0.24 dB/one spacer Cone-type spacers: 0.8 to 1.1 dB/one spacer	A spectrum analyzer and gate control method were used at 300 MHz.

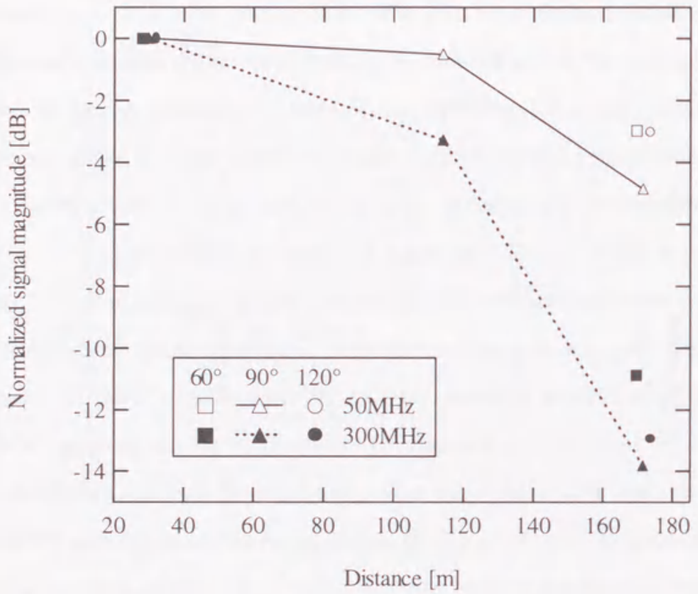

Fig. 5.10 Distance characteristics of attenuation rate of electromagnetic wave for different frequency components.

5.5 Conclusions

In this chapter, PD current pulse waveforms and corresponding electromagnetic waveforms were measured simultaneously in the full-scale 275 kV class GIL model. The propagation and attenuation characteristics of PD-induced electromagnetic wave in GIL were discussed, as follows;

(1) Electromagnetic wave signal emitted by PD with a charge magnitude of about 1 pC could be detected clearly at 169.5 m, apart from PD source, using the internal UHF sensor.

(2) PD-induced electromagnetic wave propagated in GIL with a velocity of 97% to 100% of the velocity of light, irrespective of the applied ac voltage phase where PD occurred.

(3) The electromagnetic wave signal was attenuated during its propagation in GIL. The attenuation rate of electromagnetic wave signal was calculated about 7.5 dB/100 m based on its magnitude.

(4) The attenuation rate for 50 MHz and 300 MHz components were calculated as 2.5 dB/100 m and 8.7 dB/100 m, respectively, by means of the time frequency analysis (wavelet analysis).

Moreover, the wavelet analysis for the measured electromagnetic waveform was pointed out to be most effective method to figure out the transient phenomena such as the signal reflection.

The achieved propagation and attenuation characteristics are important to determine the distribution of UHF sensors for GIL and to localize PD source in GIL with accuracy by the PD measurement. In particular, the frequency dependence of the attenuation rate can be applied to the location of PD source with the least UHF sensors. These results have been applied to the on-site, after-lying test in 275 kV actual GIL constructed and operated by Chubu Electric Power Co., Inc.

References

[1] Y.Kuroyanagi, A.Toya, T.Hayashi and T.Araki: "Construction of 8000 A Class 275 kV Gas Insulated Transmission Line", *IEEE Transactions on Power Delivery*, Vol. 5, No. 1, pp. 14-20, 1990.

[2] T.Hillers and H.Koch: "Gas Insulated Transmission Lines for High Power Transmission over Long Distances", *1998 International Conference on Energy Management and Power Delivery*, Vol. 2, pp. 613-618, 1998.

[3] T.Nojima, M.Shimizu, A.Miyazaki, T.Araki, H.Nishima, H.Hata, H.Yamaguchi, T.Yamauchi and M.Miysashita: "Study on an After-laying Test for a Long-distance GIL", *IEEE Transactions on Power Delivery*, Vol. 13, No. 3, pp. 718-727, 1998.

[4] M.D.Judd, O.Farish and B.F.Hampton: "Broadband Couplers for UHF Detection of Partial Discharge in Gas-insulated Substations", *IEE Proceedings - Science, Measurement and Technology*, Vol. 142, No. 3, pp. 237-243, 1995.

[5] G.Schöffner and W.Boeck: "PD Measurements in N_2-SF_6 Gas Mixtures with the UHF Method", *11th International Symposium on High Voltage Engineering*, Vol. 5, pp. 86-89, 1999.

[6] H.Okubo, A.Suzuki, T.Kato, N.Hayakawa and M.Hikita: "Frequency Component of Current Pulse Waveform in Partial Discharge Measurement", *9th International Symposium on High Voltage Engineering*, No. 5634, 1995.

[7] T.Utsumi, F.Endo, T.Ishikawa, S.Iwaasa and T.Yamagiwa: "Preventive Maintenance System with a Different Gas Injecting Facility for GIS", *IEEE Transactions on Power Delivery*, Vol. 8, No. 3, pp. 1107-1113, 1993.

[8] B.F.Hampron, J.S.Pearson, C.J.Jones, T.Irwin, I.M.Welch and B.M.Pryor: "Experience and Progress with UHF Diagnostics in GIS", *CIGRE*, paper 15/23-03, 1992.

[9] T.Hoshino, M.Yoshida, T.Takahashi, M.Hikita, A.Miyazaki and H.Okubo: "Comparative Measurement of Sensor Performance by Partial Discharge in Full-scale 275 kV Gas Insulated Transmission Line", *Transactions on IEE Japan*, Vol. 117-B, No. 8, pp. 1197-1203, 1997 (in Japanese).

[10] M.Yoshida, T.Takahashi, T.Hoshino, M.Hikita, A.Miyazaki and H.Okubo: "Generation of Partial Discharge Current Pulse and Its Radiation / Propagation Characteristics of Electromagnetic Wave in GIL", *Transactions on IEE Japan*, Vol. 117-B, No. 8, pp. 1204-1209, 1997 (in Japanese).

Chapter 6 Summary

In order to meet the increasing demand for electric power with stable and quality supply, SF_6 gas insulated electric power apparatus such as GIS and GIL have been widely introduced into the electric power transmission and distribution system. Metallic particle contaminants in such apparatus could induce PD and finally lead to breakdown. Thus, PD measurement and analysis based on its physical mechanism should be developed into the insulation diagnosis, the breakdown prediction and the preventative maintenance for SF_6 gas insulated power apparatus.

However, PD mechanism in SF_6 gas has never been clarified yet, because PD phenomena in SF_6 gas are too faint and fast to be measured accurately and are affected by the space charges. Moreover, under ac voltage condition, temporal transition of polarity and instantaneous applied voltage value makes the space charge behavior quite complicated.

From these viewpoints, this dissertation aims at revealing PD generation mechanisms in SF_6 gas under ac voltage condition taking the space charge behavior into account to increase the accuracy of the insulation diagnosis by PD measurement. PD measuring system using high sensitive and time-resolved techniques were established. Through the measuring system, statistical and sequential characteristics of PD generation were investigated for different experimental conditions. Moreover, propagation characteristics of PD signals in long-distance GIL were discussed. The composition of each chapter is summarized in the following sections.

6.1 Partial Discharge Mechanism in SF_6 Gas with Consideration of Space Charge Behavior

In Chapter 2, in order to elucidate PD mechanisms taking space charge behavior into account, PD characteristics under ac voltage condition with different power frequencies and gap configurations were measured, as well as those under positive dc voltage condition. The measuring systems were constructed with a wide band frequency response from dc to 1 GHz and more for PD current pulse waveform and with large expansion rate for PD light emission image.

Experimental results revealed that positive PD inception and breakdown voltage characteristics against gas pressure were clearly affected by the applied power frequency. PD characteristics at streamer region under ac voltage condition were classified into two situations; low frequency / large radius of needle tip / short gap conditions, and the opposite conditions. In the former case, PD with a large magnitude of current pulse height occurred at around the positive PD inception phase. This was due to the reduction of corona stabilization effect and generation probability of initial electrons. On the other hand, in the latter case, PD with relatively small magnitude of current pulse height was induced at around the positive PD inception phase, due to the activated corona stabilization effect. In the cases of post PD inception phase under ac and dc conditions, where lots of PD were continuously generated, PD with only a small magnitude of current pulse height occurred due to the highly activated corona stabilization effect.

Finally, a sequential model of positive PD in SF_6 gas under ac condition was proposed and verified by the calculation of the space charge trajectories for several conditions.

These results are expected to unravel the influence of the space charge behavior on the transition process from the streamer type PD to the leader type PD under ac and dc voltage conditions, which can be developed to establish the breakdown and lifetime prediction techniques of GIS by means of the precise leader-type PD measurement based on the physical PD mechanism. Moreover, they demonstrate that the influence of applied power frequency on the PD characteristics should be considered in the on-site PD testing of gas insulated power apparatus using ac high voltage source with higher power frequency.

6.2 Sequential Generation Characteristics of Partial Discharges in SF_6 Gas with Consideration of Space Charge Behavior and Corona Stabilization

In Chapter 3, to clarify the PD mechanism leading to breakdown, the sequential PD generation characteristics under ac and dc voltage conditions were observed using the measuring system with long-term high-temporal resolution. The experimental results under ac voltage condition revealed that the larger magnitude of PD was generated firstly in positive half cycle, whose charge magnitude depended on the instantaneous voltage. On the contrary, the subsequent PD had a smaller charge magnitude, which was irrespective of the instantaneous voltage. Then, the relationship between PD charge q and the preceding time Δt under positive dc condition was discussed to explain the sequential PD characteristics from viewpoint of the space charge behavior. The $q-\Delta t$ characteristics had two correlations; negative one and positive one. Negative one was found at small Δt region, derived from the activated corona stabilization effect due to the ion diffusion in the radial direction of the previous PD channel. Positive one was lied at large Δt region, attributed to the relaxed corona stabilization effect due to the ion drift into the gap space.

Finally, in order to discuss the sequential PD characteristics taking account of the space charge behavior, a model of space charge behavior and PD generation mechanism was established and confirmed by the numerical calculations of diffusion and drift processes for positive ions after PD generation.

The measuring and analysis method used in Chapter 3 is expected to be easily developed into the insulation diagnosis and the breakdown prediction techniques by means of the development of the existing PD measuring equipment and analyzing system situated on the actual GIS, because they can observe the PD signals corresponded to its charge magnitude.

6.3 Long-term Sequential Characteristics of Negative Partial Discharge in Pressurized SF_6 Gas

In Chapter 4, to clarify the sequential characteristics of negative PD in pressurized SF_6 gas and its temporal transition, the negative PD characteristics were continuously measured for 6 hours and statistically analyzed from viewpoint of the relationship between the PD current pulse height and the preceding time.

Firstly, negative PD was characterized by pulse sequence (PS) consisted by 6 or more successive PD pulses having preceding time of less than 600 ns. The length of PS strongly depended on the number of PD pulses in PS. Then, the long-term sequential PD characteristics were analyzed. The length of PS and the number of total PD pulses in one acquisition decreased in the early stage of the long-term PD generation, and then fluctuated. This is because surface roughness of the needle electrode were degraded in the early stage and the discharge decomposition was accumulated on the needle surface in the later stage, which decreased and fluctuated the generation probability of the initial electron, respectively. Then, the temporal transition of the total amount of charge in each acquisition revealed that the most determinant pulses for negative PD characteristics in pressurized SF_6 gas were included in PS.

The results achieved in Chapter 4 are expected to be developed into the diagnosis of the insulation property in testing and under operation of gas insulated power apparatus, especially in the beginning stage, because there is a probability that the gas pressure and voltage regions where the positive PD could not occur, and negative PD always starts lower voltage than positive PD.

6.4 Propagation Characteristics of Electromagnetic Wave Caused by Partial Discharge in Long-distance Gas Insulated Transmission Line

In Chapter 5, in order to clarify the propagation characteristics of PD-induced electromagnetic wave in the long-distance GIL, PD current pulse waveforms and corresponding electromagnetic waveforms were simultaneously measured in the full-scale 275 kV class GIL model. The electromagnetic wave signal emitted by a PD with a charge magnitude of about 1 pC could be detected even at 169.5 m apart from PD source using an internal UHF sensor. Then, the electromagnetic wave velocity in GIL was calculated as 97% to 100% of the velocity of light. The attenuation rate was calculated about 7.5 dB/100 m based on its magnitude, and that for 50 MHz and 300 MHz components were calculated as 2.5 dB/100 m and 8.7 dB/100 m, respectively, by means of the time frequency analysis (wavelet analysis). Moreover, the wavelet analysis was pointed out to be most effective method for the propagated electromagnetic wave to unravel the transient phenomena such as the signal reflection.

The results are important to localize PD source in GIL accurately with appropriately distributed UHF sensors with least number. These results have been applied to the on-site, after-laying test in actual 275 kV GIL constructed and operated by Chubu Electric Power Co., Inc.

6.5 Future Problems

This dissertation proposed the PD measurement techniques based on PD mechanisms in SF_6 gas and applying them to the actual SF_6 gas insulated electric power apparatus such as GIS and GIL. In order to develop the results obtained in this dissertation into the electrical insulation diagnosis and the breakdown prediction of the power apparatus, the following investigations will be needed in the future.

(1) Sequential generation characteristics and mechanisms of leader-type PD in pressurized SF_6 gas

In the actual electric power apparatus under higher gas pressure condition, breakdown could be induced not only by the streamer-type PD which was the main scope of this dissertation, but also by the leader-type PD. The generation mechanism of the leader-type PD may also be influenced by the space charges, which comes from the evidence that the breakdown voltage at higher gas pressure region under ac voltage condition with higher power frequency was slightly higher than that with lower power frequency. Therefore, the influence of the space charge behavior on the leader-type PD generation should be clarified through the measurement of the sequential PD generation characteristics and with consideration of the transition mechanism from the streamer-type PD to the leader-type PD.

(2) Application of sequential PD measurement techniques to the diagnosis of actual power apparatus

This dissertation pointed out that the sequential PD characteristics were directly linked to the space charge behavior and PD mechanism. Since the insulation condition is closely related to the PD mechanism, the sequential PD measuring techniques are expected to be developed into the insulation diagnosis and preventative maintenance. In the actual SF_6 gas insulated electric power apparatus, the PD measurements are being carried out, however, they only detect the magnitude of PD signal. Therefore, the sequential PD measurement techniques should be applied to the PD diagnosis in the actual power apparatus with developing long-term and high time-resolution technique into more conventional one.

(3) PD mechanisms for other defects

In the actual SF_6 gas insulated electric power apparatus, there could exist not only the metallic particles on the high voltage conductor and the enclosure, which were dealt in this dissertation, but also different kinds of insulation defects such as voids and delaminations in the spacer and particles on the spacer. The particles on the spacer are considered as one of the most dangerous defects to induce the breakdown. The delamination in the spacer could induce PD,

which may degrade the insulation property of the spacer and develop into breakdown. Therefore, the investigations on PD mechanisms for the other defects are needed to establish the general preventive maintenance techniques for actual SF_6 gas insulated power apparatus.

Acknowledgment

The author is indebted to his research advisor, Professor Dr. Hitoshi Okubo, Faculty of Engineering, Nagoya University, for his insightful guidance, helpful discussions and unqualified encouragement through this work. Working with him has been the most rewarding experience of the author's life, and the author will cherish it for ever.

The author would like to express his sincere gratitude to vice-advisor, Professor Dr. Teruyoshi Mizutani, Faculty of Engineering, Nagoya University, for his considerate suggestions in preparing this dissertation.

The author would like to give great thanks to vice-advisor, Associate Professor Dr. Naoki Hayakawa, Faculty of Engineering, Nagoya University, for his continuous and intelligent advice through this work and unqualified comments in preparing this dissertation.

The author would like to express his appreciation to Assistant Professor Dr. Katsumi Kato, Faculty of Engineering, Nagoya University, for his helpful and uninterrupted advice through this work.

The author would like to express his great appreciation to Professor Dr. Masayuki Hikita, Faculty of Engineering, Kyushu Institute of Technology, for his helpful discussions.

The success of the present work is linked undeniably to the collaboration of various individuals and organizations:

In Chapters 2 and 3, special thanks go to Lightning and Insulation group, Power Engineering R&D Center, The Tokyo Electric Power Co., Inc., for their kind discussions.

In Chapter 4, the author would like to express his great appreciation to Institut de Recherche d'Hydro-Québec (IREQ), represented by Dr. Michel F. Fréchette, for the utilization of their facilities, permission to use the work performed at IREQ, intensive discussions and financial supports. Special thanks also go to Toshiba Corporation, for giving a chance of joining the joint work achieved under a specific agreement between Hydro-Québec and Toshiba Corporation to the author.

In Chapter 5, the author would like to give sincere thanks to Chubu Electric Power Co. Inc., Mitsubishi Electric Co., Ltd., Sumitomo Electric Industries, Ltd., The Furukawa Electric Co., Ltd., for their intensive cooperation in the experiments and discussions.

The author would like to thank all the members of Professor Okubo's Laboratory, who have contributed to this work. Special thanks go to Dr. Tatsuro Kato (presently Hitachi, Ltd.), Messrs. Atsushi Suzuki and Masanobu Yoshida (both of them presently Chubu Electric Power Co., Inc.), and Dr. Toshihiro Hoshino (presently Toshiba Corporation) for their kind and intelligent advice through his work. The author would like to thank Mr. Shigeyuki Seto (presently Hokuriku Electric Power Co., Inc.), Mr. Takao Iwai (presently NEC Corporation), Messrs. Tatsuji Yamada, Hitoshi Saito, Takeshi Ishida, Daiyo Shibutani, Akihisa Matsushita and Keiji Hatta for their cooperation in this work.

Finally, the author would especially like to thank his parents for giving him the great chance to make this work, and unqualified encouragement and support.

List of Publications Concerned with This Dissertation

Chapter	Title	Journal & Date	Coauthor
2	Power Frequency Dependence of Space Charge Behavior and Partial Discharge Characteristics in SF_6 Gas	IEEE Transactions on Dielectrics and Electrical Insulation, Vol. 7, No. 1, pp. 152-160, 2000.	T.Yamada N.Hayakawa H.Okubo
	Partial Discharge Mechanism in SF_6 Gas with Consideration of Space Charge Behavior	IEEE Transactions on Dielectrics and Electrical Insulation (submitted)	N.Hayakawa S.Yuasa S.Okabe H.Okubo
	Dependence of Partial Discharge and Breakdown Characteristics on Applied Power Frequency in SF_6 Gas	8th International Symposium on Gaseous Dielectrics, pp. 295-300, Virginia Beach, U.S.A., 1998.	T.Yamada M.Hikita H.Okubo
	Partial Discharge Mechanism in SF_6 Gas with Consideration of Space Charge Behavior under ac and dc Voltage Conditions	13th International Symposium on Gas Discharges and their Applications, Glasgow, U.K., 2000.	N.Hayakawa S.Yuasa S.Okabe H.Okubo
3	Space Charge Behavior in SF_6 Gas Viewed from Sequential Generation of Partial Discharge Pulses	IEEE Transactions on Dielectrics and Electrical Insulation, Vol. 7, No. 1, pp. 141-145, 2000.	T.Yamada N.Hayakawa H.Okubo
	Space Charge Behavior and Corona Stabilization Effect in SF_6 Gas Viewed from Sequential Generation of DC Partial Discharge	Journal of Physics D: Applied Physics (submitted)	N.Hayakawa S.Yuasa S.Okabe H.Okubo

Chapter	Title	Journal & Date	Coauthor
3	Space Charge Behavior in SF_6 Gas Viewed from Sequential Generation of Partial Discharge Pulses	International Workshop on High Voltage Engineering (IWHV'99), HV-99-10/SP-99-10, Okinawa, JAPAN, 1999.	T.Yamada, N.Hayakawa H.Okubo
	Corona Stabilization Effect in SF_6 Gas Viewed from Sequential Generation of Partial Discharge	11th International Symposium on High voltage Engineering, Vol. 3, pp. 88-91, London, U.K., 1999.	T.Yamada N.Hayakawa S.Yuasa S.Okabe H.Okubo
4	Long-term Sequential Characteristics of Negative Partial Discharge in Pressurized SF_6 Gas	9th International Symposium on Gaseous Dielectrics, Ellicott City, U.S.A, 2001. (submitted)	M.F.Fréchette R.Y.Larocque C.Hudon T.Umemura S.Matsumoto H.Okubo
5	Simultaneous Measurement of Partial Discharge Current Pulse and Its Electromagnetic wave in Full-scale 275kV Gas Insulated Transmission Line (in Japanese)	Transactions on IEE of Japan, Vol. 117-B, No. 8, pp. 1210-1215, 1997.	T.Hoshino M.Yoshida M.Hikita A.Miyazaki H.Okubo
	Partial Discharge Measurement in a Long Distance SF_6 Gas Insulated Transmission Line (GIL)	IEEE Transactions on Power Delivery, Vol.13, No.3, pp.683-690, 1998.	H.Okubo M.Yoshida T.Hoshino M.Hikita A.Miyazaki
	Partial Discharge Measurement in Long Distance SF_6 Gas Insulated Transmisson Line (GIL)	10th International Symposium on High voltage Engineering, Vol.4, pp.167-170, Montreal, CANADA, 1997.	H.Okubo M.Yoshida T.Hoshino M.Hikita A.Miyazaki